Microstructure and Mechanical Behavior of Ultrafine-grained Ni-Mo Alloys Processed by Top-Down and Bottom-Up Methods

Garima Kapoor

Ph.D. Dissertation

Submitted to

Doctoral School of Physics, Eötvös Loránd University
Materials Science and Solid-State Physics Program

Supervisor: **Prof. Jenő Gubicza**, DSc

Head of Doctoral School

Head of Doctoral Program: **Prof. István Groma**

Eötvös Loránd University, Department of Materials Physics

Budapest
2019

To the Graduate Council

This Ph.D. Dissertation is submitted for partial satisfaction of the requirements for the degree of Doctor of Philosophy in Materials Science from Department of Materials Physics in Eötvös Loránd University, Budapest. My Ph.D. research was conducted under the supervision of senior supervisor Prof. Dr. Jenő Gubicza at Department of Materials Physics at Eötvös Loránd University.

Garima Kapoor

Doctoral School of Physics, Eötvös Loránd University

Head of doctoral school: Prof. **Jenő Gubicza**

Materials science and solid-state physics program

Head of the doctoral program: Prof. **István Groma**

Table of Contents

List of Acronyms

UFG	Ultrafine-grained
RT	Room Temperature
SPD	Severe Plastic Deformation
LAGB	Low-angle Grain Boundaries
HAGB	High-angle Grain Boundaries
ECAP	Equal-channel Angular Pressing
HTP	High-pressure Torsion
ECAE	Equal-channel Angular Extrusion
SFE	Stacking Fault Energy
GB	Grain Boundary
DSC	Differential Scanning Calorimetry
XLPA	X-ray Line Profile Analysis
XRD	X-ray Diffraction
fcc	Face-centred Cubic
SEM	Scanning Electron Microscopy
TEM	Transmission Electron Microscopy
EDS	Energy-dispersive X-ray Spectroscopy
LNT	Liquid Nitrogen Temperature
hkl	Miller Indices
CMWP	Convolutional Multiple Whole Profile
EBSD	Electron Backscatter Diffraction
OIM	Orientation Imaging Microscopy
EDM	Electro-discharge machining
IPF	Inverse Pole Figure
KAM	Kernel Average Misorientation

Preface

Nanostructured materials (or simply nanomaterials) broadly refers to the class of materials which are composed of structural elements (such as the crystallites) with the size below 100 nm along at least one characteristic structural length. If the crystallite size is between 100 nm and 1 μm, the material is referred to as ultrafine-grained (UFG). The research on nanostructured and UFG materials have gained significant attention over the years owing to their unique physical, chemical and mechanical properties. In spite of several novel applications of nanomaterials, the influence of processing technique on the evolution of microstructure and lattice defects, such as dislocations or twin-faults and their effect on the mechanical behavior have not been deeply understood yet.

The objective of my PhD research was to study the microstructure, defect structures and mechanical properties of UFG and nanocrystalline Ni-Mo alloys. In the past two decades, numerous investigations were carried out to study the microstructure and the mechanical properties of various UFG alloys such as Al-Mg, Al-Zn-Mg, Cu-Zn, Cu-Al, Cu-Cr, Cu-Zr, etc. Although Ni-Mo alloys have important practical applications, no research has been conducted yet to examine the effect of Mo solute atoms on the microstructure of UFG Ni processed by top-down and bottom-up methods. Therefore, this thesis includes investigation of the influence of processing methods on microstructure, defect structure and mechanical behavior of Ni-Mo alloys. For this purpose, the specimens were produced by both bottom-up (electrodeposition) and top-down (severe plastic deformation) methods. Furthermore, the correlation between the mechanical properties and the defect structure was explored. Additionally, research was undertaken to assess the thermal stability of the microstructure and the defect structure in nanocrystalline and UFG Ni-Mo alloys during annealing. Moreover, the effect of the varying concentration of Mo in Ni on the defect structure and the mechanical properties was examined.

Layout of the Thesis

This thesis is divided into five chapters as follows:

In Chapter 1, I include a brief description about the properties and applications of Ni-Mo systems. Additionally, this chapter summarizes the processing of UFG and nanocrystalline (NC) materials by top down and bottom up methods. The effect of processing techniques and their conditions on the microstructure, defect structure, thermal stability and mechanical properties of the as-processed materials is also discussed.

In chapter 2, I present the details of the material processing and the experimental techniques used in this research. XRD technique was extensively used in this study, therefore the detailed description of XLPA method is included along with brief details of other characterization techniques such as SEM and TEM, DSC, microhardness and uniaxial tensile tests.

In chapter 3, I show the influence of Mo addition on the microstructure, thermal stability and hardness of Ni alloy processed by a combination of cryorolling and HPT. The evolution of microstructure, defect structure and mechanical properties of UFG Ni alloys processed by SPD with increasing SPD straining is presented. Additionally, the evolution of grain size and dislocation density were also investigated as a function of the annealing temperature and then correlated to the evolved DSC peaks.

In chapter 4, I present the evolution of the microstructure, defect structure as well as mechanical properties of thin films of Ni alloys with low and high Mo concentrations, which were processed by electrodeposition with and without saccharin addition. The calculation of the change of stored energy during annealing is also included.

In chapter 5, I discuss the influence of processing route on the microstructure, defect structure, thermal stability and stored energy. For this purpose, I compared the results obtained by the investigation of Ni-Mo bulk nanomaterials processed by HPT with that of Ni-Mo layers with very similar compositions but processed by electrodeposition

Chapter 1: Literature Overview

This chapter consists of a brief description of the properties and applications of Ni-Mo system. Further, the fundamentals of the processing of UFG and nanocrystalline materials by top-down and bottom-up methods are overviewed. It also covers the influence of processing methods and their conditions on the microstructure, defect structure, thermal stability and mechanical properties of processed materials.

1.1. Ni-Mo System

Ni-Mo alloys exhibit advantageous properties which make them useful for various practical applications. For instance, these alloys are used as catalysts in hydrogen production [1–3] and as substrate material for superconducting coatings [4]. It was shown that Ni-Mo alloys exhibit high activity and long-term stability as the hydrogen evolution reaction under alkaline conditions occurs either in the form of a catalyst coating [1] or as unsupported nanopowder [2,3]. Besides, they exhibit corrosion resistance to the dilute non-oxidizing acids, such as hydrogen chloride. Ni-Mo alloys can be used as electrocatalysts in the cathodic production of hydrogen. Nanocrystalline electrodeposited Ni-Mo thin films are potentially applicable as novel catalytic materials with ferromagnetism [5]. The Ni-Mo substrates for superconducting coatings are produced by severe cryorolling and subsequent annealing resulting in an extremely sharp cube texture which is required for epitaxial coatings. Moreover, Ni-Mo alloys have the potential to serve as ecological alternatives to chromium plating in the automotive and decorative plating industry since these alloys exhibit high hardness and wear resistance [6]. Along with these beneficial mechanical properties, the Ni-Mo alloys also possess good thermal and corrosion resistance, and therefore, they are readily useful as hard coating materials [7].

The equilibrium binary phase diagram for the Mo-Ni system is shown in Fig.1.1 [8]. This phase diagram shows that the solubility limit of Mo in Ni is less than 1 at.% at room temperature (RT), while a considerable amount of Mo can be dissolved in Ni at elevated temperature. There are three intermediate phases which are close to the stoichiometric Ni_4Mo, Ni_3Mo and NiMo compositions. The Ni_4Mo and Ni_3Mo phases are stable with a fixed composition only while the NiMo phase has a measurable range of existence and forms peritectically from the liquid [8–10]. Since I studied UFG and nanocrystalline Ni-Mo alloys, in the next sections, the processing methods of these materials are overviewed.

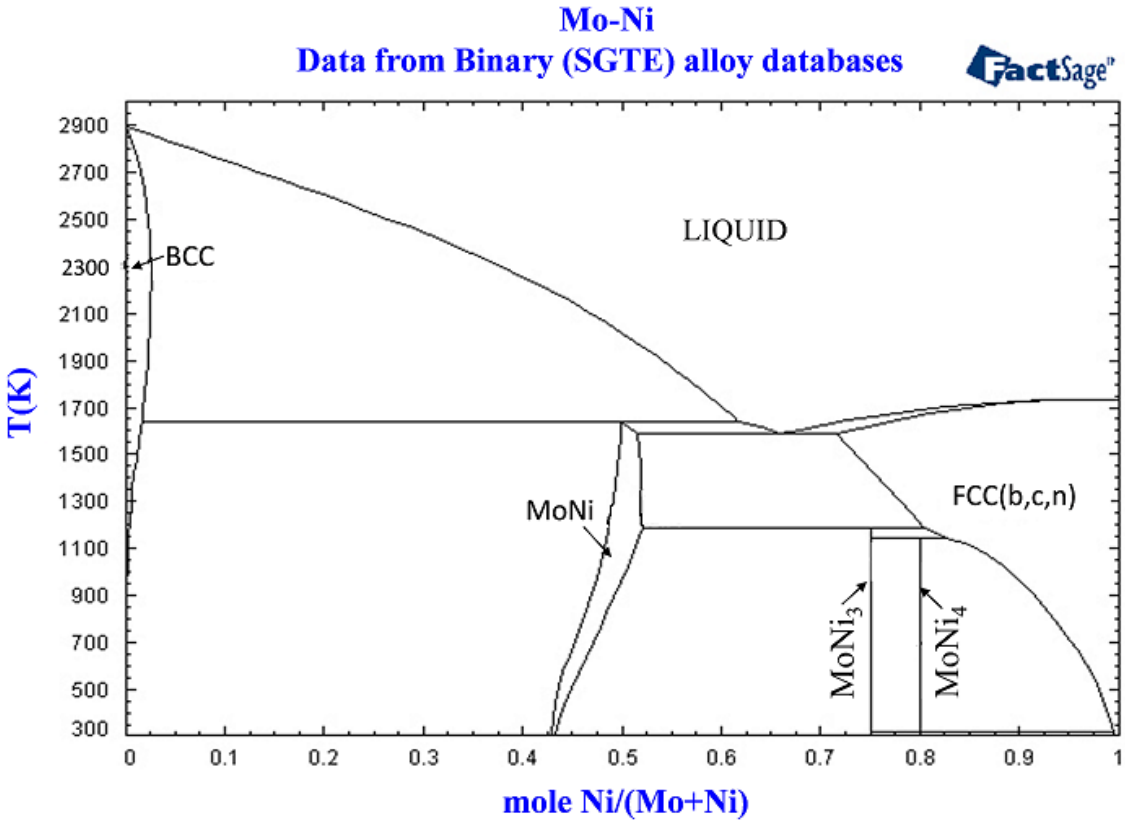

Fig. 1.1: Equilibrium phase diagram for Mo-Ni system.

1.2. Processing routes of nanomaterials

The processing techniques of bulk nanomaterials can be classified as bottom-up and top-down methods as shown in Fig. 1.2. In the case of top-down approach, the starting coarse-grained bulk material is transformed to UFG or nanocrystalline state using severe plastic deformation (SPD) techniques. On the other hand, in bottom-up procedures, the bulk nanostructured materials are built up through the assembly of individual atoms or nanoparticles.

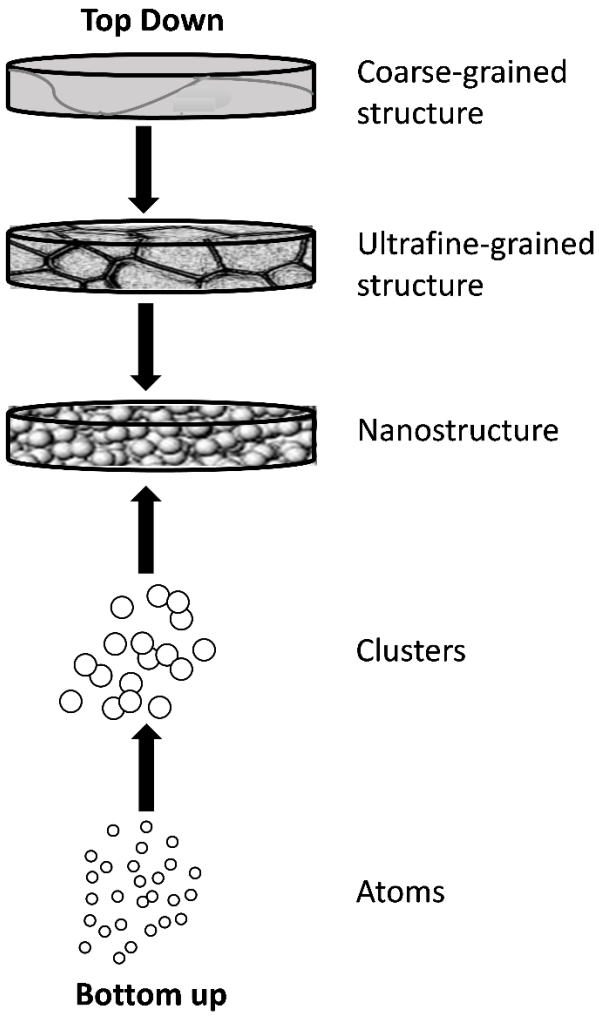

Fig. 1.2: Schematics illustrating the top down and bottom up processing methods for bulk nanomaterials.

Over the years, several different bottom-up techniques have been developed and employed for the fabrication of nanomaterials such as chemical vapor deposition, physical vapor deposition, inert gas condensation, and electrodeposition [11–15]. This approach has demonstrated a great potential to produce materials with exceptionally small grain sizes; however, it also comes with challenges such as contamination and porosity introduced during the fabrication.

Contrary to this method, the top-down approach involves the larger macroscopic initial structures which undergo grain refinement and leads to the formation of nanosized microstructural units (grains or crystallites). This refinement of the coarse-grained workpiece to UFG or nanomaterials is usually carried out by the process of SPD. The processing by SPD comprises of those metal forming procedures which involves subjecting a bulk material to a very high strain without any significant modification in its overall dimensions. Such procedures can be applied to the bulk materials as well as powder samples. The major advantages of fabrication of UFG and nanomaterials by SPD techniques over bottom-up processing techniques are contamination-free and porosity-free final microstructures.

1.2.1 Severe Plastic Deformation

SPD is one of the most efficient techniques to produce metals and alloys with nanocrystalline (below 100 nm) or UFG (100 nm to 1000 nm) microstructure. Grain size is a crucial parameter which influences nearly all aspects of the physical, mechanical and chemical properties of polycrystalline metals [16]. Thus, the modification of grain size offers strong control over the valuable properties of the materials [17]. The grain refinement in SPD-processed specimens is usually associated with the formation of a high density of lattice defects, such as dislocations, stacking and twin faults. The dislocations which are formed during processing, tend to arrange themselves into low energy configurations (e.g., low-angle grain boundaries, LAGBs). Further,

with increasing the strain, the LAGBs transform into high-angle grain boundaries (HAGBs), thereby resulting in grain refinement [18]. The microstructural development induced by SPD is reflected in the changes in the properties of materials, such as strength, ductility and corrosion resistance [19].

Over the years, several investigations were conducted to study the microstructural changes and their effect on the properties of SPD-processed specimens [20–23]. Since single-step processing cannot impose huge strains on the material, multi-step processing techniques are often used. However, besides the imposed strain, the grain size is also controlled by other factors such as temperature, strain rate and route of SPD processing. The most commonly used SPD processes are equal channel angular pressing (ECAP) [24] and high-pressure torsion (HPT) [25].

The ECAP technique also referred to as equal-channel angular extrusion (ECAE), is an effective SPD tool for producing UFG materials [26]. In ECAP, SPD is caused by pressing the sample (billet) with a piston through a die containing two lubricated intersecting channels. The cross-section of the billet matches with that of channels, thereby causing deformation only at the intersection of the two channels. After the removal of the billet from the exit channel, elastic relaxation causes a slight increase in the diameter of the specimen. Thus, if the cross-sections of the entry and the exit channels are same, then a surface layer of the sample should be removed between the consecutive passes. This is not necessary if the entry channel diameter is slightly higher than that for the exit channel. Since the cross-sectional dimensions of the billet remain practically unchanged, the repeated pressing can help to achieve very high strains [18]. The repetitive pressing accumulates the shear strain in the billet and thereby increases the microstrain while simultaneously reducing the size of crystallites to nanocrystalline range. The microstructural characteristics of the billets processed by ECAP are dependent on several parameters such as the angle between the two channels and the outer arc of curvature. Besides grain refinement, the ECAP processing not only can increase the HAGB fraction but also high

texturing effects could be introduced. The high fraction of HAGB in ECAP-processed specimens yields improved fatigue behavior as well as better corrosion resistance.

HPT is one of the most powerful SPD methods for grain refinement and strength increment [27–30]. HPT refers to a processing technique in which a disc or ring-shaped specimen is subjected to torsional strain under high hydrostatic pressure. This method was first introduced eight decades ago at Harvard University by Bridgman to investigate the phase transformations and mechanical behavior of the materials under high pressure and concurrent torsional straining [31]. In 1988, Valiev et al. reported a further development of this method in achieving significant grain refinement to the submicrometer levels and eventually to nanometer levels [26]. Over the last two decades, this technique has been recognized as an efficient SPD method in the study of the microstructure and the mechanical properties of UFG and nanomaterials [32]. In the scope of this thesis, as HPT technique is primarily applied for plastically deforming the specimens, therefore a detailed description of this technique is presented in next few sub-sections.

1.2.1.1 Fundamentals of HPT

The principle of HPT set-up is illustrated schematically in Fig.1.3. In the HPT device, the sample is placed within a coin-shaped cavity, which is located between two massive anvils. During the processing, high compressive pressure of several GPa is applied between the upper and lower anvils. Furthermore, the specimen is simultaneously subjected to a torsional strain imposed by the rotation of one anvil (usually the lower one) with respect to the other such that the surface frictional forces deform the disk by shear [28].

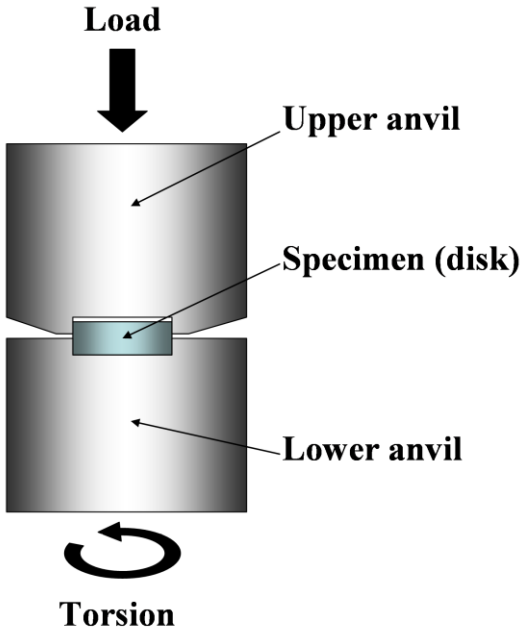

Fig. 1.3: Processing of disks by High pressure torsion technique.

The sample shape used for the HPT processing is conventionally in the form of a disk, however, occasionally HPT technique was also applied to specimens in the form of hollow cone [33], cylinders [34], rings [35], and U-shape samples [36]. Conventionally HPT-processing is performed at RT; however it is possible to conduct at elevated temperatures up to 1000 K [28,37,38].

There are three distinct categories of HPT technique, namely, unconstrained, quasi-constrained and constrained HPT, as illustrated schematically in Fig.1.4.

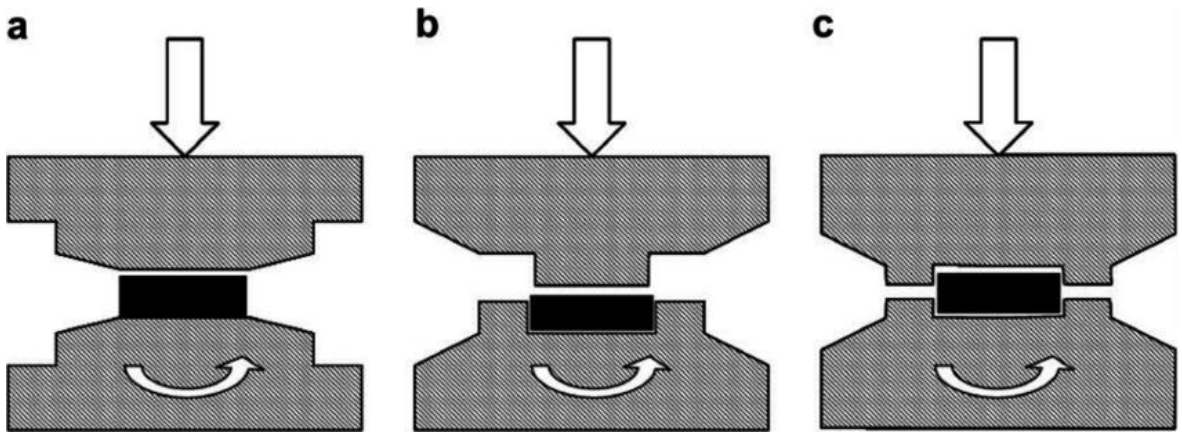

Fig. 1.4: Schematic illustration of HPT for a) unconstrained b) quasi-constrained c) constrained conditions.

In unconstrained HPT, the sample is placed between two flat anvils and the lateral flow of the material is not restricted under the applied load [39]. Under these conditions, the application of pressure can result in a free flow of the material outwards, and only minor backpressure is exerted on the sample due to the frictional forces acting between the specimen and the anvil. In the case of constrained HPT, a sample is prepared so that it fits well into the cavity in the lower anvil. Though the specimen is subjected to high applied pressure and torsion straining, but, the sample material cannot flow outward due to almost negligible gap between the two anvils [18]. In practice, the true constrained HPT has to be performed in the presence of an effective backpressure. However, the ideal constrained condition is not easy to achieve. Therefore, the experiments involving the third type of HPT processing, i.e., the quasi-constrained HPT has gained popularity over the other two categories [40]. In the quasi-constrained HPT, the sample is contained within the shallow depressions in the lower and upper anvils in such a way that the initial sample thickness is much greater than the sum of the depths of both anvil cavities. Therefore, such quasi-constrained condition permits at least some limited outward flow of material between the upper and lower anvils [41].

1.2.1.2 Strain Imposed by HPT

The total strain imposed on the HPT processed disk can be estimated by using two approaches. The first (Hencky/Eichinger) approach can determine the imposed strain by the following logarithmic relation:

$$\varepsilon_{Hencky} = ln\left(\frac{2\pi N r h_0}{h^2}\right), \tag{1.1}$$

where N is the number of rotation, r is the radius of the disk, h_0 and h are its initial and final thicknesses, respectively. This formula takes into account the reduction in thickness of the disk caused by the applied pressure, and therefore it can be used if there is some outward flow of material between the two anvils, causing reduction in h_0 [42-44].

According to the von Mises approach, the dependence of equivalent strain (ε_{vM}) on the distance from the center (r) can be expressed by a linear relation [43,44]:

$$\varepsilon_{vM} = \frac{\gamma}{\sqrt{3}} = \frac{r\theta}{\sqrt{3}h} = \frac{2\pi N r}{\sqrt{3}h}. \tag{1.2}$$

The above equation is based on the assumption that the thickness of the disk does not change during HPT. This formulation signifies that the torsional straining imposed on the sample depends on the distance from the center of the disk. There is zero torsional straining at $r = 0$, which increases linearly along the disk radius and reaches a maximum value at the peripheral region. Thus, strong inhomogeneity in the torsional shear strain exists along the radius of the HPT processed disk [45]. In this thesis, eq. (1.2) is used for the calculation of equivalent strain.

1.2.1.3 Advantages and disadvantages of HPT

One of the advantages of the HPT technique is that extremely large shear strain value can be achieved through this technique in a very simple way [28]. HPT processing not only can

generate a high equivalent strain but also a defined continuous variation of strain compared to most other SPD techniques, where strain is applied cycle by cycle to the sample. It also allows easy estimation of flow stress by measuring the total torque with respect to angle of rotation [42]. Higher hydrostatic pressure in HPT improves the workability of the specimens and thereby, this technique can be even applied for severe deformation of relatively hard and brittle materials, which are difficult to process by other SPD methods. When such hard to deform materials are subjected to much higher pressure, a higher maximum degree of deformation occurs. This induces a considerable reduction in grain size and further improvement in the mechanical properties. However, it is to be noted that the maximum achievable stress that can be applied is constrained by the fracture strength of the anvil material [29].

The major disadvantage of HPT is that it cannot be used to process very large samples, thus its applications are mainly restricted to laboratories and could not be employed for industrial purposes. Additionally, the inhomogeneous microstructure along the disk radius can cause inhomogeneity in the mechanical properties, which can be another challenge for its industrial and large-scale applications [46]. However, several research findings conclude that in many materials adequate homogeneity can be achieved through gradual evolution of the microstructure. For instance, according to previous reports on high purity Ni [47], Cu [48], and commercial purity Al [49], the variation in microhardness across the sample present in the early deformation stages, later evolved to a homogeneous value on applying sufficiently high total strain under a high applied pressure [26].

1.2.2 Electrodeposition

1.2.2.1 Fundamentals of electrodeposition

The process of electrodeposition of alloys involves electrochemical reduction of two or more metallic components from their salt(s) onto a substrate under controlled conditions [50]. The deposition conditions can be optimized and regulated as per the required specifications of the as-deposited layer. Some macroscopic parameters, such as composition [51] and pH [52] of the baths, have an indirect impact on the resulting alloy. These parameters influence the dissolving regime (*e.g.*, aquo ion, complexes, and clusters) of the metal ions in the bulk electrolyte and in the vicinity of the substrate [53]. Further, this regime contributes to the formation of deposition intermediate which regulates the properties of the final film.

The thin film is deposited on the surface of a conductive substrate using electricity. The simplest electrodeposition apparatus is an electrochemical cell consisting of an anode (positive electrode), cathode (negative electrode), electrolytic bath, current source and ampere/volt meter [54]. Electrolytes are usually aqueous solutions containing positive and negative ions, prepared by dissolving metal salts. The cathode is the conducting substrate onto which the layer of desired material has to be deposited. The anode can be the metal to be deposited (in this case, the anode is sacrificial), or it can be inert (when the anode reaction is the decomposition of the solvent). Both anode and cathode are immersed in the same electrochemical bath and then either a voltage or a fixed current can be applied between the electrodes. When direct current (DC) is passed through the electrolyte the ions migrate towards the electrodes with the opposite charge i.e., positively charged ions to the cathode and negatively charged ions to the anode. This charge transfer completes the electrical circuit, thereby resulting in the reduction of cations of the desired material from the solution and deposition of that material as thin layer on the surface of

substrate. Hence, the overall reactions taking place during electrolysis involves the reduction reaction at the cathode due to metal ions as well as the oxidation reaction at the anode due to electrons. These reactions can be represented as:

$$M^{Z+} + ne^- \rightarrow M, \qquad (1.3)$$

$$M \rightarrow M^{Z+} + ne^-, \qquad (1.4)$$

$$H_2O \rightarrow 2H^+ + \frac{1}{2}O_2 + 2e^- \text{ for pH}\leq 7, \qquad (1.5)$$

$$4OH^-_{(aq.)} \rightarrow H_2O + \frac{1}{2}O_2 + 4e^- \text{ for pH}\geq 7. \qquad (1.6)$$

where the reaction corresponding to Eq. (1.3) occur at the cathode, Eq. (1.4) at a soluble anode, both Eq. (1.5) and Eq. (1.6) occur at an insoluble anode with pH lower and higher than 7, respectively [55]. The above anodic reaction depends on the pH and electrolyte composition. Stable pH can be maintained during the electrodeposition process by addition of citrate in the bath [56].

Faraday's laws can be regarded as the backbone of the electrodeposition theory. According to Faraday's first law, the quantity of substance produced by electrolysis in a given time is proportional to the quantity of electricity passing through the electrolyte [57]. The second law states that the masses of different substances liberated as a result of the passage of the same quantity of electricity through the electrolyte are proportional to the chemical equivalent weights of the substances. The electrochemical equivalent of a substance is the weight of that substance liberated in unit time by unit current. Mathematically, the weight of metal deposited (W) at the surface of cathode/substrate can be calculated as follows [54]:

$$W = \int I(t)dtM_w/nF \qquad (1.7)$$

where $I(t)$ is the applied current as a function of time t, F is the Faraday constant, n is the number of electrons and M_w is the molar mass of the metal that undergoes electroreduction. The electrodeposition reactions that occur at the cathode/electrolyte interface are heterogeneous in nature, involving the mass transfer and charge transfer steps. Depending on the relative hindrance of the consecutive processes, the deposition can be activation controlled or mass

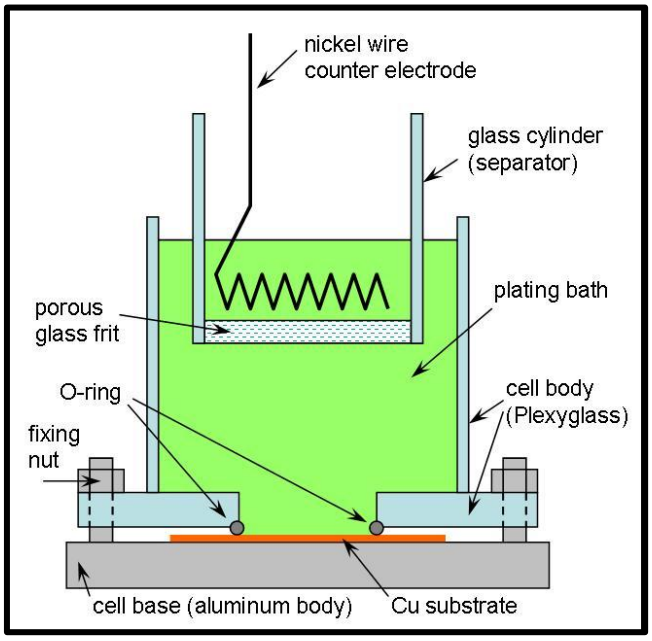

Fig. 1.5: Design of setup for processing nickel layers by electrodeposition.

transport controlled in extreme cases, or may be of mixed control in intermediate conditions. The other factors which affect the electrodeposition of metals are electrolyte concentration, temperature, addition agents, nature of the electrolyte and nature of the metal on which the deposit is to be made.

The formation of each grain consists of two stages: nucleation and growth. Both the nucleation and growth processes compete with each other and their kinetics determines the morphology and final size distribution of the deposited layer [58,59]. The nucleation process is affected by various parameters such as the crystal structure of the substrate (or that of the already deposited metal), adhesion energy, specific free surface energy, lattice orientation of the electrode surface and lattice mismatch at the nucleus–substrate interface boundary. The nucleation can be divided

into two types: instantaneous and progressive. In the case of instantaneous nucleation, the formation of nuclei on the substrate is instantaneous and is followed by subsequent growth with the time of electrodeposition without forming new nuclei. Thus, the nuclei have larger radii, and the deposited layer has rougher surface morphology. Contrarily, the progressive nucleation process involves continuous formation of new nuclei as a direct function of time of electrodeposition with gradual growth and can provide flatter surface morphology [54,60].

1.2.2.2 Induced codeposition mechanism

Concerning the dependence of the composition of the alloys deposited on the ratio of the metal ions in the solution, various codeposition modes are distinguished in the electrodeposition literature. For four basic codeposition modes (equilibrium, regular, irregular and anomalous) [61] the entire composition range can be swept because both components of the alloy can be deposited alone, too. This latter feature is, however, not true for the so-called induced codeposition in which one of the components cannot be obtained in pure form.

The electrodeposition of the elements such as P, Ge, W and Mo is not possible from aqueous media; however, these metals can be co-deposited by forming alloys with iron group hyper-transition metals [61–66]. The process of codeposition of elements such as P, Ge, W and Mo beside Ni, Co, Fe is classified as induced codeposition. For instance, pure Mo cannot be deposited alone (induced metal), while Ni (inducing metal) can be deposited with high current efficiency and also it facilitates the deposition of Mo as alloying element [61,67,68].

The phenomenon of induced co-deposition was first described by Brenner in 1963 [61]. Over the years, several mechanisms have been proposed to explain the induced codeposition of Mo with Ni [63,69–71] Zeng et al. investigated co-deposition mechanism of Ni with Mo from citrate solutions and suggested a mechanism involving electrochemical reduction of molybdate anion (MoO_4^{-2}) to MoO_4 which is subsequently reduced to a metallic form by hydrogen accumulated

on the surface of inducing metal nickel to form molybdenum in alloys [72]. However, later some studies undermine the role of the hydrogen in the co-deposition process. They suggested another mechanism which involves the presence of complex Ni-Mo species in the electrolyte, and these dissolved Ni-Mo complexes were reduced during co-deposition of molybdenum [56]. This mechanism has been subjected to criticism as the presence of complex Ni-Mo species in the electrolyte could not be experimentally detected. Podlaha and Landolt developed a mathematical model to quantitatively predict the mechanism of induced codeposition assuming the codeposition of Mo with Ni through an adsorbed nickel-molybdenum intermediate species [68]. Although several mechanisms have been proposed to explain the induced codeposition behavior of Mo, but no general agreement has been established [73]. The intensive investigations on induced co-deposition of Ni-Mo have entitled the mass transport as a crucial factor for the deposition behavior of Ni-Mo alloys, especially when the concentration of nickel in the electrolyte is higher than that of molybdate [69,71,74–76].

During the process of electrodeposition, the factors such as bath temperature, electrode rotation rate, pH of the solution and applied current density have considerable influence on the properties of the processed layers which are discussed in detail in the next section. In the solution of lower molybdate concentration with a larger amount of nickel, the Mo content in the alloy can be increased by increasing electrode rotation rate and decreased by increasing the current density. Thus, in the electrolytes containing high nickel content along with low concentration of molybdate, Ni is deposited under kinetic control, and molybdate is co-deposited under diffusion limiting conditions. The general trend in such case is that the increase in Mo content of the deposit leads to a decrease in current efficiency, particularly in alkaline solutions and when the citrate:nickel ratio is larger than one [72,77]. However, if concentration of molybdate is higher than that of nickel, then the composition of the deposited alloy is

independent of the rotation rate, as in this case, the deposition rate of both Ni and Mo is controlled by the flux of the nickel ion toward the cathode.

Thus, depending on relative concentrations, mass transport of either molybdate or nickel species may limit the rate of deposition of molybdenum [67]. Since electrodeposited Ni-Mo alloys of higher than 25 at.% molybdenum content and obtained from a stagnant solution always contain a significant amount of oxygen, an enhanced convection was suggested to achieve purely metallic deposits [76]. The Mo-content enhancement as a result of the application of both a vigorous convection [76] and pulse plating [78,79] confirm that the diffusion-limited transport of the molybdate ions, as well as the pH relaxation at the electrode surface, are important during the alloy formation. The application of appropriate additives proved to be also successful in increasing the Mo content of the deposits [80]. Ni-Mo alloy coatings deposited even from additive-free baths appear to be inherently nanocrystalline [5,7,77,81], especially when pulsed current is used for their deposition [82]. If coherent sample series are scrutinized in which only one technical parameter is modified during their deposition, the crystallite size decreases with the increase of the Mo content of the alloys. The electrodeposition of Ni-Mo alloys shows much commonality with any pair from the (Ni,Co,Fe)–(Mo,W,Re) group. The similarity ranges from the induced nature of the codeposition process through the drastic decrease in crystallite size with the increase in the refractory metal content to the structural relaxation upon heat treatment.

1.3. Properties of nanomaterials

1.3.3 Microstructural and mechanical properties of HPT-processed materials

The microstructure of specimens obtained by the application of HPT technique is highly dependent on the processing conditions such as applied pressure, processing temperature, strain rate and the number of revolutions [29]. The higher values of applied pressure, strain rate and

number of revolutions can cause greater grain refinement, however, such refinement become less pronounced on increasing the processing temperature [38]. In addition to the grain refinement, the homogeneity in HPT processed disks can also be controlled by the imposed pressure and the number of turns. The inhomogeneous distribution in strain further causes variation in microstructure across HPT disk. However, at sufficiently high strains and pressure, it is possible to remove this inhomogeneity and obtain a homogeneous microstructure along the radius of the HPT processed disk. The most widely used models to explain the grain refinement mechanism during SPD are based on dislocations. The dislocation cell structures formed during the early stages of plastic deformation, gradually transforms the bulk structure into a fine-grained structure. The dislocations formed due to the high strain introduced by SPD processing rearrange themselves into LAGBs. These LAGBs then gradually transform to HAGBs, thus causing the grain refinement. The minimum grain sizes obtained by HPT depends on the characteristics of the deformed material, such as its crystal lattice, melting temperature, and stacking fault energy (SFE) [83].

According to a report by Meyers et al., when the diameter-to-thickness ratio of the HPT disk is low, the pressure at the center of the disc can be unusually large [84]. Additionally, when the sample thickness increased, an axial inhomogeneity can also occur in addition to inhomogeneity along the radius [85]. Thus, the lower value of thickness to diameter ratio of the disk can be used to achieve a better sample homogeneity. Moreover, not only the dimension of the HPT-processed sample but also its shape can affect the microstructural homogeneity. For instance, a study which compares the microstructural evolution of ring and conventional disk-shaped samples, concluded that ring-shaped samples are effective in order to reach high strain in a single revolution leading to a more homogeneous microstructure compared to the disk specimen [86]. The chemical composition and purity of the material also significantly influence the final microstructure achieved by HPT processing. Furthermore, the applied pressure during HPT

processing causes a plastic flow of the sample material into the surface roughness of the anvils, which helps to obtain large friction between the sample and the anvil for the subsequent torsional straining. There is a lower limit to the applied pressure, which is necessary to have an adequate frictional force, in order to avoid any relative slippage between the anvil and the sample surfaces during rotational straining. This minimum amount of applied pressure is at least three times the yield stress of the initial undeformed sample material [29].

The temperature may increase during HPT processing due to the severity of plastic deformation. The heat generated within the HPT disk during HPT processing can have a drastic effect on the microstructural evolution and deformation mechanisms [87]. The temperature rise becomes more significant at higher imposed pressures, rotation speed, processing time, and at larger distances from the disk center. Among the abovementioned factors, the rotation speed is the most crucial parameter to control the temperature rise. Previous research claims that the rise in temperature depends on the processed materials and their hardness. According to a research which employs finite element simulations and experimental measurements for HPT processing of model metals with N = 10 at ω = 1.0 rpm and P = 6 GPa, the total generated heat is higher for harder materials: 16 kJ for Al, 41 kJ for Cu, 73 kJ for Fe and 155 kJ for Mo. This study also confirms that in spite of enormous plastic deformation during processing by HPT, the temperature rise is not significant (below 90 °C) in comparison to the melting temperatures of the selected model metals [88].

Though no fixed relationship exists between the grain refinement and dislocation density in SPD processed materials, the larger dislocation density value is accompanied by lower grain/crystallite sizes [18,89]. This can be explained by the arrangement of dislocations into the grain and sub-grain boundaries, which leads to refinement of grains in materials subjected to SPD procedures. The saturation dislocation density is determined by the dynamic equilibrium established between the dislocation multiplication and annihilation. The greater the hindrance

to annihilation of dislocations during SPD-processing, the higher the maximum achievable dislocation density. The annihilation of dislocations become difficult by the solid solution alloying, presence of secondary phase particles, the low homologous temperature during SPD processing and the high degree of dislocation dissociation due to the low SFE. The ways to maintain low homologous temperature during SPD processing are (i) processing at low temperatures (e.g., cryogenic rolling at liquid nitrogen temperature) and (ii) processing materials with high melting points [18]. The maximum dislocation density in an SPD-processed material has a strong dependence on the SFE [90][91] and the melting temperature. The thermally activated (cross-slip and climb) processes of dislocation annihilation can explain the dependence of saturation dislocation density on the melting point of the processed materials. The maximum dislocation density at high imposed strains is controlled by the diffusion-controlled climb process. When SPD is performed at RT on materials with higher melting point, the activation energy is greater and therefore, the relatively slower climb process contributes to a higher saturation dislocation density [92].

The addition of alloying elements to metallic materials can further enhance the grain refinement and the increase in the dislocation density during SPD processing [93]. The pinning effect of solute atoms and precipitates on dislocations and grain boundaries in alloys impedes the dislocation annihilation and grain coarsening, thereby leading to improved mechanical strength in the SPD-processed materials. For instance, in Cu-rich alloys processed by HPT at RT, on increasing the nickel content, substantial grain refinement and enhanced microhardness were observed [94]. Moreover, the solute atoms can improve the strength not only directly by increasing the critical resolved shear stress of dislocation glide but through an indirect way by increasing the dislocation density [92]. Hence, the addition of alloying elements influences the development of the UFG microstructures during SPD as well as their thermal stability.

The stability of SPD-processed UFG materials is a prerequisite of their reliable operation in practical applications. When grain growth occurs, the improved strength of UFG materials deteriorates, and therefore a study of the microstructural stability is necessary for the commercialization of these materials. The recovery and recrystallization behaviors of UFG materials are usually investigated by differential scanning calorimetry (DSC) combined with direct or indirect observations of the microstructure [95–98]. Former studies revealed that for SPD-processed pure metals and dilute alloys the recovery of the dislocation structure and the recrystallization could not be separated in the thermograms since they occur in a single exothermic DSC peak [99–104]. The temperature of the peak maximum depends on the method of SPD processing, the imposed strain and the heating rate. However, its value is usually between ~0.3–0.4 × T_m, where T_m is the melting point in Kelvin degrees [18]. It was also shown that the activation energy of recovery/recrystallization is usually about 0.5 ± 0.1 × Q_{self} where Q_{self} is the activation energy of self-diffusion, irrespective of the type of material and the processing method [105–108]. The observed values of the activation energies suggest that recovery and recrystallization are mainly controlled by diffusion along grain boundaries and dislocations. It is noted that for 4N and 4N8 purity Ni samples processed by HPT, an additional small DSC peak was observed at the homologous temperature of ~0.24 which corresponds to the annihilation of single and double vacancies [109]. However, the majority of reported DSC experiments do not show this vacancy peak. At the same time, for solid solutions with high solute content and precipitate hardened alloys, two exothermic peaks were often observed [110,111]. The first peak is related to recovery while the second peak corresponds to recrystallization and grain growth. This separation of recovery and recrystallization is attributed to the segregation of alloying elements and/or the formation of precipitates at grain boundaries. Then, these act as obstacles against grain boundary migration, thereby hindering

recrystallization and grain growth. The activation energy for the first "recovery" peak is usually smaller than that determined for the second "recrystallization" peak.

Despite the numerous reports on DSC studies of SPD-processed metallic materials, systematic studies on the influence of strong alloying on the thermal stability of the defect structure and the grain size have not been performed to date.

The experiments show that instead of single step HPT processing, a combination of HPT with other SPD and non-SPD processing routes (such as rolling) gives the potential for achieving a greater grain refinement in bulk metallic materials [112–114]. Among non-SPD techniques, cryorolling is very effective in achieving a small grain size because the extremely low temperature (usually liquid nitrogen temperature is applied) suppresses any dynamic recovery of the dislocation structure and the occurrence of grain growth during deformation [115]. Therefore, a combination of cryorolling and subsequent HPT at RT appears to be a promising SPD method for the production of metals and alloys with UFG or nanocrystalline microstructures.

1.3.4 Factors influencing the properties of electrodeposited films

The electrodeposition parameters such as applied current density**,** pH and bath temperature play a critical role in controlling the final microstructure and grain refinement of deposited layers [52,116–118]. As the rate of nucleation and growth can be controlled by the current density, the low current density causes a small overvoltage only and hence, the growth rate of nuclei is dominant over the rate of formation of new nuclei. Thus, the layer deposited at low current density tends to possess coarse-grained microstructure. On increasing the current density, the structure generally becomes finer due to the increased rate of formation of nuclei. This trend holds true for numerous investigations on nickel coatings [119,120], though some exceptions

could be found in the literature where contrary behavior was also observed [116,117,121]. When the current density increases beyond the limiting value of the electrolyte, porous and spongy deposit can form due to the release of hydrogen [122].

The pH of the solution is one of the important factors to obtain electrodeposited films with the desired structural and functional properties. The variation of electrolyte pH can have a strong effect on the crystallite size, chemical composition, preferred orientation, and crystallite shape [123].

Additionally, the temperature of bath during electrodeposition can affect the nucleation-growth and the microstructure of the deposited film. Therefore, by optimizing bath temperature, some important characteristics of the final coating such as grain size, brightness, internal stress, surface roughness, texture, chemical composition and current efficiency, can be controlled. The previous report on electrodeposited nanocrystalline Ni coatings concluded that both the electrodeposition rate and the microhardness of thin films is affected by the bath temperature [118]**.**

Beside the deposition conditions, the chemical composition of the material also influences the microstructure and the mechanical properties of electroplated layers as it has been shown for Ni-Co alloys [124–126]. For instance, the grain refinement and the defect density can be further enhanced through the addition of alloying elements to electrodeposited metals [93]. The previous studies have shown that the addition of organic additives such as saccharin and formic acid to the electrolyte bath yielded a smaller grain size and a larger defect density in nanocrystalline Ni layers processed by electrodeposition [127,128]. Saccharin is also known for its stress-relieving and hardening properties, thus used as one of the most common organic additives in industrial nickel baths.

Internal stresses can build up within the deposited layer due to electro-crystallization process and/or the codeposition of impurities such as sulfur, hydrogen, and other elements. The nature

of the internal stresses can either be tensile or compressive. Under the influence of tensile stress, the average distance between nickel atoms in the lattice is larger than the equilibrium value, creating a force that attempts to bring the atoms closer together. Thus, the deposit contracts after its removal from the substrate and can even crack under extreme conditions. Contrarily, the opposite effect is observed in presence of compressive stress, where the force tends to drive them further apart causing the deposit to expand.

Due to the difference in initial and final stress, the removal of the substrate causes the deposited layer could curl towards or away from the anode, depending upon whether the internal stress in the deposit is of tensile or compressive nature, respectively**.** The addition of organic additives can help in reducing or even entirely getting rid of the curvature in free-standing thin films [129]. According to a report on the effect of saccharin on nickel electrodeposition from sulfate electrolyte, the saccharin addition can reduce the tensile stresses of Ni deposits and eventually result in the compressive stress. It also concluded that the degree of reduction of tensile stress can be controlled by the concentration of saccharin in nickel deposits, till saccharin has reached saturated adsorption beyond which its effect on internal stresses become significantly low [130]. In the scope of this thesis, the original goal of the addition of saccharin was only to reduce the internal stresses causing curvature in free-standing thin films [129]. The decrease of these stresses is necessary for increasing the shock tolerance (thermal or mechanical) in the practical application of these materials. At the same time, saccharin not only reduces the internal stresses in electrodeposited films but also acts as a grain refiner [55,131]. Several studies have reported a rapid decrease in grain size by addition of the saccharin. Moreover, saccharin addition yields smaller grain size and greater defect density than some other additives such as formic acid [132]. However, this grain refinement is only limited to a certain concentration, above which grain size is not further reduced on increasing the saccharin content and saturation is observed. Thus,

both alloying and addition of organic additives have a significant impact on the microstructure and the mechanical properties of nanomaterials processed by electrodeposition [127,133].

As mentioned in the previous section, the annealing of nanostructures at high temperatures usually causes a reduction of defect density and grain coarsening; therefore, nanomaterials may lose their exceptional properties. Numerous investigations on nanocrystalline nickel have been conducted to show the dependence of thermal stability on several parameters such as the type and concentration of impurities, lattice defects, initial grain size, grain shape and its distribution, grain boundary (GB) structure and crystalline texture [134–139]. Former studies have shown that GB segregation of impurities or alloying elements helps to achieve a higher thermal stability [140]. In addition, the pinning effect of alloying elements on lattice defects, such as dislocations, can hinder their annihilation. Thus, the alloying elements kinetically retard the recovery and recrystallization of nanostructures [141–143]. At the same time, alloying in nanomaterials increases the lattice defect density including GBs, thereby enhances the thermodynamic driving force of recovery and recrystallization. A similar effect is expected when organic additives such as saccharin (contains sulfur atoms) are added to the electroplated materials [137,144–147]. In alloys containing organic additives, it is an open question whether the thermodynamic or the kinetic effect is the stronger, i.e. the addition of alloying elements and organic additives together increases or decreases the thermal stability of nanomaterials. Surely, the answer depends on the type and concentration of alloying elements and organic additives [130,148].

The energy stored in lattice defects such as stacking faults, GBs, dislocations and vacancies [18] formed during the production of nanomaterials has a great impact on the thermal stability of the nanomaterials [109,149]. The high stored energy in UFG and nanomaterials can make them thermodynamically unstable which limits their applications at high temperatures. Even if the nanomaterials processed by bottom-up routes do not undergo any deformation, a high defect

density has been detected in these materials too [15,150–152]. Therefore, the determination of the energy stored in lattice defects has a significance in nanomaterials produced either by SPD or bottom-up methods. A direct method for measuring the stored energy is DSC. Alternatively, the stored energy can be determined indirectly by calculating the contributions of different lattice defects (GBs, dislocations etc.) whose density can be obtained from quantitative structural characterization. The comparison of the results obtained by the two methods enables an indirect determination of important structural quantities such as GB energy per area [109,149,153]

Several investigations have been performed on the mechanical properties of nanocrystalline Ni films prepared by electrodeposition technique, suggesting improved hardness [154–156] and tensile strength [52,156–160]. Whether the reduction of grain size is accompanied by a continuous increase or decrease in hardness beyond a critical grain size is highly dependent upon the processing method [154]. The strengthening effect in nanocrystalline Ni films has been observed on decreasing the grain size when nanomaterials follow regular Hall-Petch behavior [118,155,156]. When the grain size falls into the regime of the inverse Hall–Petch relationship, a softening behavior is observed, and grain size reduction is no longer beneficial [161]. Former studies have shown that short time annealing at moderate temperatures may improve the ductility considerably while the strength decreases only slightly [97,162–165]. Interestingly, an opposite effect of heat-treatment was also observed in UFG and nanocrystalline solid solutions, namely a hardening caused by annealing [166–171]. In UFG materials processed by SPD techniques, this effect was explained by the annihilation of mobile dislocations during annealing [168]. Then, the reduced mobile dislocation density makes plastic deformation more difficult, leading to hardening. A different mechanism of annealing-induced hardening was observed in nanocrystalline alloys. A recently published study [171] demonstrated that for electrodeposited nanocrystalline Ni-Mo alloys with the grain sizes of ~3-25 nm an annealing at 600-800 K

resulted in hardening. This effect was explained by the segregation of Mo atoms at the grain boundaries which may lead to a more difficult occurrence of grain boundary mediated deformation mechanisms, such as grain boundary sliding. Therefore, for higher Mo concentrations the annealing-induced increase in hardness was found to be larger. In SPD-processed UFG Ni-Mo alloys, the annealing-induced changes in the mechanical performance may differ significantly from the results observed for their electrodeposited nanocrystalline counterparts due to the much larger grain size in the UFG alloys.

1.4. Motivation

The production of ultrafine-grained (UFG) or nanostructured materials either by top-down or bottom-up route is usually accompanied by lattice defect formation, such as stacking faults, grain boundaries (GBs), dislocations and vacancies. The type and density of lattice defects can have a significant impact on the properties of nanomaterials. Therefore, it is important to deepen our understanding of the relationship between lattice defects and properties of nanomaterials. Over the years, there is an increasing interest in employing severe plastic deformation (SPD) techniques for production of UFG materials. High-pressure torsion (HPT) is considered as the most effective SPD method in grain refinement and improvement of the strength of metallic materials. Moreover, the experiments showed that a combination of HPT with other SPD and non-SPD processing routes (such as rolling) gives the potential for achieving a greater grain refinement in bulk metallic materials. In the case of bottom-up techniques, the processing by electrodeposition is a conventional yet one of the most effective and low-cost methods. Further improvement in the properties of UFG and nanomaterials can be achieved by the addition of alloying elements which influence the microstructure as well as its thermal stability. A similar effect is expected when organic additives are added to the electrodeposited materials.

Ni-Mo alloys exhibit high hardness, wear, thermal and corrosion resistance, and have several important practical applications. However, the effect of Mo atoms on the microstructure and defect structure of UFG Ni prepared by different processing techniques has never been investigated yet. For this purpose, Ni-Mo alloy specimens were processed by both bottom-up (electrodeposition) and top-down (severe plastic deformation) routes with similar chemical compositions. My PhD research incorporated the influence of processing route on the microstructure, defect structure and mechanical properties of UFG and nanocrystalline Ni-Mo alloys. It also takes into account the influence of Mo alloying and saccharin addition on the characteristics of Ni alloy thin films processed by electrodeposition. In addition to the study of the thermal stability of the microstructure and defect structure during annealing, the correlation between the lattice defects and the mechanical properties was also investigated.

In my PhD research work, I performed the X-ray experiments for the characterization of all the samples investigated within the scope of this thesis to determine various microstructural parameters. For this purpose, after measuring the X-ray diffraction (XRD) patterns, I conducted the evaluation using the X-ray line profile analysis (XLPA) method. I carried out the sample surface preparation for X-ray and scanning electron microscopy (SEM) investigations. I evaluated the electron backscatter diffraction (EBSD) images to obtain grain size and grain boundary fractions using OIM software. Additionally, I calculated the grain sizes using transmission electron microscopy (TEM) images for those thin-film samples which were beyond the detection limit of EBSD. I evaluated the differential scanning calorimetry (DSC) thermograms and calculated the stored energies for SPD processed and electrodeposited samples. I also performed the microhardness tests to determine the mechanical properties of the samples and then correlated the mechanical properties to the microstructure and defect structure.

Chapter 2: Materials and Experimental Methods

In this chapter, the details of the material processing and the experimental techniques used in this research are overviewed. Firstly, the top-down and bottom-up processing techniques used for the fabrication of bulk and thin films, respectively, are described. These as-processed specimens along with the samples annealed using DSC method were then characterized using various experimental methods. X-ray diffraction technique was extensively used in this study, therefore the detailed description of X-ray line profile analysis (XLPA) method is included. This section also briefly presents the specifications of other microstructural characterization techniques such as scanning electron microscopy (SEM) and transmission electron microscopy (TEM). Furthermore, the details of microhardness and uniaxial tensile tests applied for the investigation of mechanical properties are discussed.

2.1. Processing of Ni-Mo Alloys

Ni alloys with low (~0.3 at%) and high (~5 at%) Mo contents were prepared by induction melting and casting into a Cu-mould. The as-cast ingots, having diameters of ~32 mm, were hot-rolled at 1100 °C to a thickness of ~13 mm. The hot-rolled samples were subjected to a two-step combined SPD process. In the first step, small strips were cut from the hot-rolled materials and cryorolled at liquid nitrogen temperature (LNT). During cryorolling, the thickness decreased from ~13 mm to ~3 mm in multiple passes with a thickness reduction of ~5% per pass. After each cryorolling pass, the strips were cooled again to LNT. From the plates obtained after cryorolling, discs were prepared with diameters of 10 mm and thicknesses of 1 mm. These samples were then processed by HPT technique under quasi-constrained conditions [30] with an applied pressure of 6.0 GPa and rotating speed of 1 rpm at RT for ½, 5 and 20 turns. The

chemical compositions of the HPT-processed Ni alloys were determined by energy dispersive X-ray spectroscopy (EDS) in SEM. The detailed results of EDS will be shown later in Chapter 3, however, it is worth to mention that the Mo concentrations in the alloys with low and high Mo contents were about 0.28 and 5.04 at.%, respectively. Hereafter, the materials with low and high Mo concentrations are designated as LMo and HMo respectively. The samples processed by the combination of cryorolling and subsequent HPT are labeled as LMo-HPT and HMo-HPT for low and high Mo contents, respectively.

It is noted that, in addition to Mo, other elements such as Al, Fe and Si were also detected in the samples. Nevertheless, the most significant difference between the chemical compositions of the two samples was the much higher Mo content in the material labeled HMo.

Electrodeposited Ni-Mo samples were prepared at RT with a galvanostatic electrolysis by using a solution containing 0.52 mol/l $NiSO_4$, 0.26 mol/l sodium citrate, 0.1 g/l sodium dodecylsulfate as a wetting agent, and Na_2MoO_4 in varying concentration up to 6 mmol/l. It was particularly important to use a high-purity nickel sulfate salt with c(Co) < 50 ppm (produced by Jenapharm) in order to minimize the impurity content of the deposit. The bath was operated at pH =6.1 ± 0.08 where the deposition efficiency of pure Ni was the maximum (about 98%) in a wide current density interval, in agreement with the finding of Ref. [72]. The current density was −5.6 mA/cm^{-2} where the desired concentration range of Mo in the deposit could be achieved by varying only the Mo content of the solution. The Faradaic efficiency as calculated from the true composition (the measurement of which is described later) and from the sample weight was nearly constant, exhibiting a similar value as observed for the deposition of pure Ni from the Mo-free bath. This high current efficiency of 96–98% is unprecedented for Ni-Mo alloys, and is due to both the pH optimization and the small current density used (which was about an order of magnitude smaller than the customary current density range used in general for Ni-Mo plating). The substrate was a Cu sheet that was degreased prior to the deposition experiment

and then placed horizontally at the bottom of the cell, allowing only the upward-facing side to contact the bath. A nickel wire spiral served as the counter electrode and was immersed into a frit-separated chamber of the cell in order to avoid the contamination of the deposit with the disintegrated grains of the sacrificial anode. The desired thickness of about 20 μm was regulated by the deposition time. When the electroplated specimens had to remove from their substrate, they were connected as anode in a cell containing 0.3 M CuSO4 solution buffered with acetic acid – sodium acetate solution to pH=5. In this solution, the Cu substrate could be dissolved from the Ni alloy with an excellent selectivity at +0.35 V electrode potential with respect to a saturated calomel electrode [58]. The end-point of the complete substrate removal was indicated by a drop of the current below the level of 60 μAcm^{-2}.

The chemical compositions of the electrodeposited layers were determined by EDS in an FEI Quanta 3D SEM. The Mo contents in the layers with low and high Mo contents, designated as LMo-ED and HMo-ED, were ~0.4 and ~5.3 at.%, respectively. These values were intentionally selected as the present electrodeposited films will be compared with bulk fine-grained Ni-Mo alloys having similar compositions but processed by HPT [172]. In addition to the effect of Mo concentration, the influence of the saccharin on the microstructure and its thermal stability was also investigated. Therefore, additional samples were processed by adding 1 g/l saccharin to the bath as the majority of grain refinement occur at 1 g/l saccharin in case of electrodeposited Ni [132]. These samples are denoted as LMo-sac-ED and HMo-sac-ED. In these specimens, EDS revealed the same Mo contents as for the saccharin free layers, but in addition sulfur was also detected with the concentration of ~0.2 at.%. Please note that in this research any change in the microstructure caused by the sulfur impurity can be regarded as a part of the effect of the processing method as saccharin was added intentionally to the bath in order to refine the grain structure, avoid texture formation and reduce internal stresses.

2.2. Experimental methods

2.2.1 X-ray Diffraction Analysis of the Lattice constant

X-ray diffraction (XRD) is one of the most important non-destructive tools for the characterization of crystalline materials. The periodic arrays of atoms, ions or molecules in crystalline solids act as a diffraction grating for incoming X-rays. The interaction of X-rays with atoms in the crystal lattice results in elastic scattering of X-ray photons, therefore causing constructive interference of a monochromatic X-rays scattered at specific angles from each set of lattice planes in a specimen, which produces X-ray diffraction peaks. The angle at which constructive interference occurs can be determined by the Bragg's equation, which describes the relationship between the X-ray wavelength (λ), the interplanar spacing (d_{hkl}) for planes (*hkl*) and the scattering angle (θ) as:

$$2d_{hkl}sin\theta = \lambda. \tag{2.1}$$

The lattice spacing $d$hkl for a given *hkl* Miller-indices can be used to determine the lattice parameter (a). For the simplest case of cubic symmetry, this relationship can be given as:

$$a = d_{hkl}\sqrt{h^2 + k^2 + l^2}. \tag{2.2}$$

The first step to obtain the lattice parameter is to calculate the values of interplanar spacing d_{hkl} for the different indices using the Bragg's law. The d_{hkl} and *hkl* values for cubic crystals are then substituted into eq. (2.2). This thesis covers the investigation of the samples with cubic structures only, therefore, the equations for other types of crystals are not described here.

2.2.2 X-ray Line Profile Analysis

XLPA is a powerful and well-established method besides electron microscopy to analyze the microstructure of nanomaterials. The X-ray diffraction pattern of a crystalline material is considered as a fingerprint of its periodic atomic arrangement. The diffraction peaks of an infinitely large and perfect defect-free crystal can be described by a Dirac-delta function. However, any perturbation in perfect infinite order of atoms in ideal crystalline material, originating either from lattice distortions or finite size of scattering crystallites is reflected in the diffraction line profiles. Thus, X-ray peak profile analysis exhibits high potential to reliably characterize important microstructural parameters, such as average crystallite size, size distribution as well as density and type of crystal defects. Additional contributions to broadening include instrumental broadening, compositional broadening due to heterogeneities in chemical composition and broadening caused by surface relaxation. However, in many cases, especially for nanocrystalline materials produced by SPD, the contributions from these effects are negligible compared to broadening effects of crystallite size and lattice defects, and hence, can be neglected. Apart from standard applications of X-ray diffraction, such as phase analysis and determination of lattice parameters, the XLPA technique has proven to be a very powerful method for determining the microstructural and defect structural parameters of nanomaterials. This technique exhibits high competence in reliable determination of dislocation density, as the probed volume is 10^3-10^5 times larger than that of TEM, thereby providing better statistics to obtain the microstructural parameters. Furthermore, it is a non-destructive method and doesn't require complicated sample preparation techniques. It only requires the sample to be mechanically polished followed by chemical etching or electropolishing to remove the topmost surface layer, usually damaged at the time of cutting and/or mechanical polishing.

The broadening of X-ray line profiles is usually described by the kinematical theory of diffraction. This theory is based on three underlying assumptions. Firstly, the multiple scattering is considered as negligible, which means that each X-ray photon is scattered only once inside the crystal. The second criterion assumes that the X-ray photon scattering is elastic, i.e., the wavelength of photon remains constant during a scattering event. The third assumption is that the diffraction is coherent, i.e., the phase change of the X-ray wave during scattering is the same for all scattering events. Following the above assumptions, the diffracted intensity distribution is majorly determined by the arrangement of atoms in the crystal. Thus, the intensity and position of the diffraction peaks can be used for the determination of the crystal structure. The experimental intensity profile consists of different intensity contributions which originate from small crystallite size, lattice defects and planar faults. Therefore, the measured line profile can be described as the convolution of the profile functions corresponding to the physical (caused by the microstructure) and the instrumental broadening contributions. The Fourier-transform of the measured intensity profile $A_M(L)$ can be calculated as a simple product of the Fourier-transforms of the size $A_S(L)$, strain (distortion) $A_D(L)$, planar fault $A_F(L)$ and instrumental $A_I(L)$ Fourier-transforms:

$$A_M(L) = A_S(L)\ A_D(L)\ A_F(L)\ A_I(L) \tag{2.3}$$

where L is the Fourier variable with length dimension, given by

$$L = \frac{n\lambda}{2(sin\theta_2 - sin\theta_1)}, \tag{2.4}$$

where n is an integer, λ is the wavelength of X-rays, and θ_1 and θ_2 are the start and end points of the angular range of the measured diffraction profile.

2.2.2.1 Crystallite Size Broadening of X-Ray Diffraction Peaks

A specimen, either single crystal or polycrystalline, can be imagined consisting of small fragments with distinct crystallographic orientations, referred to as domains (or crystallites). These small coherently scattering domains with the size less than the extinction length (about 1 μm), contributes towards broadening of the diffraction peaks. In contrast, to the Dirac-delta shaped peaks for infinite size single crystals without any lattice defect, the peak profiles of reflections in polycrystalline materials have finite breadth [173]. Moreover, this broadening tends to increase with the decrease in the diameter of the crystallite perpendicular to the reflecting planes. XLPA has significantly evolved since the relationship between the crystallite size and the breadth of X-ray diffraction peak profiles was first established in the last century by the Scherrer formula (1918). In 1950, Bertaut proposed a method to determine the line profile of a size broadened peak for reflection *hkl* by considering the division of reflecting crystallites perpendicular to the planes (*hkl*) into parallel and independent scattering columns and then adding up the intensities diffracted by each of these columns [174].

The Fourier-transform for the scattered X-ray intensity distribution caused by the crystallite size can be calculated from the column-length distribution density function *p(t)* as [175]:

$$A^S(L) = \frac{1}{< t >_{area}} \int_L^\infty (t - L) p(t) dt \,. \tag{2.5}$$

where *p(t)dt* represents the relative fraction of columns for which the length parallel to the *hkl* diffraction vector lies between *t* and *t*+*dt* while <*t*> is an average column length obtained as the ratio of the total volume of the reflecting crystallites and their cross-section normal to the *hkl* diffraction vector. The function *p*(*t*) can be expressed in terms of the crystallite size distribution density function, *f*(*x*), as:

$$p(t) = N \int_0^\infty h(t,x) f(x) dx \,, \tag{2.6}$$

where *N* is a normalization factor and *h(t, x)dt* is the relative fraction of columns with lengths between *t* and *t+dt* in the crystallite with diameter *x*. The crystallite size distribution function, *f(x)dx*, represents the relative number of crystallites having diameters lying within *x* and *x+dx* range.

Considering the simplest case, with the assumption of spherical crystalline domains having log-normal size distribution, the size broadening effect becomes isotropic, i.e., independent of the diffraction order (i.e., of the indices *hkl*), then *h(t, x)* and *f(x)* can be expressed as :

$$h(t,x) = \begin{cases} \frac{2t}{x^2}, & t \leq x \\ 0, & t > x \end{cases} \tag{2.7}$$

$$f(x) = \frac{1}{\sqrt{2\pi}\, x\sigma} exp\, (-\frac{[\ln(x/m]]^2}{2\sigma^2}) \,, \tag{2.8}$$

where *m* and *σ* are the median and the square-root of the log-normal variance of the crystallite size distribution, respectively. The expression obtained after inserting the formulae of *h(x, t)* and *f(x)* from equation (2.7) and (2.8) in *p(t)* from equation (2.6) can be further substituted in equation (2.5) to determine the Fourier transform, $A^S(L)$ of the line profile caused by the crystallite size as:

$$A^S(L) = \frac{1}{2} erfc\left[\frac{ln\left(|L|/m\right)}{\sqrt{2}\sigma} - 1.5\sqrt{2}\sigma\right] - \frac{3}{4mexp(8.125\sigma^2)} L\ erfc\left[\frac{ln(L/m)}{\sqrt{2}\sigma} - \sqrt{2}\sigma\right] + \frac{3}{4m^3exp(10.125\sigma^2)} L^3\ erfc\left[\frac{ln(L/m)}{\sqrt{2}\sigma}\right], \quad (2.9)$$

where *erfc* is the complementary error function define as:

$$erfc(x) = \frac{2}{\sqrt{\pi}} \int_x^\infty \exp(-t^2)\, dt. \quad (2.10)$$

Equation (2.9) signifies the dependence of Fourier coefficients on two independent parameters of the log-normal size distribution function, m and σ, of spherical crystallites which can be used to determine the different mean size values of the crystallites.

The area-weighted mean crystallite size, $<x>_{area}$, defined as the mean size of crystallites weighted by their surface area, is used for the characterization of the crystallite size in this thesis and can be calculated as:

$$< x >_{area} = \frac{\int_0^\infty \pi x^3 f(x) dx}{\int_0^\infty \pi x^2 f(x) dx} = m \cdot exp(2.5\sigma^2). \quad (2.11)$$

2.2.2.2 Strain Broadening of Diffraction Line Profiles

The displacement of atomic positions in a real crystal from a perfect order due to the external and/or internal stresses causes broadening of X-ray diffraction lines. The source of these lattice distortions is usually the strain fields of lattice defects, such as dislocations, but can also originate from surface relaxation in nanoparticles. These distortions yield both shift and

broadening of the diffraction peaks, caused by the change of the average spacing between atoms due to stresses and the variance of the interatomic spacing, respectively.

The Fourier-transform of the X-ray peak profile caused by the lattice distortion (strain) can be determined by the following equation [176]:

$$A^D(g,L) = exp(-2\pi^2 g^2 L^2 < \varepsilon_{g,L}^2 >)\,, \tag{2.12}$$

where g is the magnitude of the diffraction vector *hkl* and $\langle \varepsilon^2_{g,\,L} \rangle$ is the mean-square strain normal to (*hkl*) lattice planes, which is a function of g and L.

In general, the greater the lattice distortion, the broader the diffraction peak. However, the broadening of X-ray peaks associated with point defects is not detectable due to the short-range character of their strain field, i.e., on increasing the distance from the defect, *r*, the strain field decays quickly with r^{-3}. On the other hand, the strain field of an individual dislocation has a long-range character as it decays with r^{-1}. Thus, dislocations have significant contribution to line profiles broadening, especially in plastically deformed metallic materials, where the lattice distortion is primarily caused by the presence of dislocations. The mean-square strain in cases where the dislocations are the cause of distortion can be given as:

$$< \varepsilon_{g,L}^2 \geq \frac{b^2}{4\pi} \rho C_{hkl} f^* \left(\frac{L}{R_e}\right), \tag{2.13}$$

where b and ρ are the magnitude of Burgers vector and dislocation density, respectively. C_{hkl} is the dislocation contrast (or orientation) factor and f^* is the so-called Wilkens function. Here, R_{e} is the effective outer cut-off radius of dislocations, which reflects how far from the core of dislocation the strain field becomes negligible. Strong screening of the dislocation strain fields occurs by the arrangement of dislocations into low-angle grain boundaries or dipoles which

lowers the total distortion in the lattice and thereby yields a smaller value of R_e. This indicates that the strain field of dislocation is not only dependent on the dislocation density but also the arrangement of dislocations. Thus, instead of R_e, it is more appropriate to characterize the screening of the strain field of dislocations using a dimensionless dislocation arrangement parameter, *M*, which can be obtained as:

$$M = R_e \rho^{1/2}. \tag{2.14}$$

The lower value of *M* corresponds to a stronger screening of the strain fields of dislocations [173]. Moreover, the greater the screening of the strain fields of dislocations, the longer the tails observed in the diffraction profiles.

Substituting equation (2.13) into (2.12), the Fourier-transform of the line profile caused by the strain field of dislocations can be expressed as:

$$A^D(L) = exp\left(-\frac{\pi b^2}{2} g^2 L^2 \rho C_{hkl} f^*\left(\frac{L}{R_e}\right)\right). \tag{2.15}$$

According to the above equation, the line broadening has a strong dependence on the diffraction vector, the Burgers and line vectors of dislocations, and the elastic anisotropy of the crystal. Additionally, the strain fields of dislocations have anisotropic nature, which results in a specific dependence of line broadening on indices of reflections *hkl* for randomly oriented polycrystalline materials. Consequently, even the same dislocation structure causes different peak broadening for the different *hkl* reflections. This effect referred to as strain anisotropy is included in the contrast factor C_{hkl} in equation (2.16).

For a non-textured cubic polycrystalline sample, or if all possible slip systems are equally populated by dislocations in the case of textured or single crystalline cubic material, the $\bar{C}_{hkl}$ can be obtained by averaging of the individual contrast factors, C_{hkl}, over *hkl* indices of the reflections which appear at the same Bragg angle [177]. By this method, the average contrast factor for cubic materials can be written as:

$$\bar{C}_{hkl} = \bar{C}_{h00}(1 - qH^2)\,, \tag{2.16}$$

where

$$H^2 = \frac{h^2k^2 + h^2l^2 + k^2l^2}{(h^2 + k^2 + l^2)^2} \tag{2.17}$$

and q describes the edge/screw character of dislocations. $\bar{C}_{h00}$ is the average contrast factor for reflection *h00*.

As this thesis focuses on cubic materials, only the contrast factors for cubic crystal system are determined. The value of $\bar{C}_{h00}$ and q for a given dislocation slip system can be calculated on the basis of the dislocation crystallography and the anisotropic elastic constants of the material. The contrast factors can be determined by the software ANIZC (that can be found on the website *http://metal.elte.hu/anizc*) [178]. The theoretical values of parameter q for pure edge and screw dislocations were calculated using the elastic constants and the dislocation slip systems activated in the crystal. The experimental value of parameter q obtained by X-ray line profile analysis can be used to describe the edge/screw character of the dislocation. For dislocations character determination, the theoretical values for pure edge and screw dislocations are compared with the experimentally determined q_{exp} obtained from XLPA. For Ni q equals 1.38 and 2.21 for edge and screw dislocations, respectively. If the experimental q value is close to the theoretical values for either edge or screw dislocations (q_{edge} or q_{screw}, respectively), then the

dislocations have either pure edge or pure screw character, respectively. On the other hand, if q_{exp} doesn't match with either the theoretical q_{edge} or q_{screw}, and rather lies between them, then the dislocation structure has a mixed character. The degree of edge character of dislocations can be estimated by the quantity

$$\frac{q_{exp} - q_{screw}}{q_{edge} - q_{screw}}$$

which is zero and one for pure screw and edge dislocations, respectively.

2.2.2.3 Broadening by Planar Faults

Planar faults are two-dimensional lattice defects in crystalline materials, such as twin boundaries, stacking faults etc., produced either during plastic deformation or recrystallization of severely strained microstructures [18]. The physical and mechanical properties of nanomaterials can be significantly altered by the presence of these faults and thus, it is necessary to determine their type and density. X-ray line profile analysis is an effective tool to investigate the stacking faults as well as twin boundaries in nanomaterials and UFG materials due to the large information volume. The characteristics of a profile observed in the presence of planar faults differ considerably from those caused by either the small crystallite size or dislocations. These faults not only yield anisotropic (i.e., *hkl* dependent) broadening of X-ray line profiles but also may cause displacement of the peak center and asymmetry of peaks. Moreover, the broadening and shift due to planar faults depend on the type of these faults, the *hkl* indices of reflection and the probability of twinning. In the case of fcc crystals, the X-ray line profile is influenced by the planar faults present on {111} planes only if its *hkl* indices satisfy the condition $h+k+l \neq 3m$ where m is an arbitrary integer. Under this condition, the peak center is displaced from the exact Bragg-position and line broadening occur, which is proportional to $|h+k+l|$ and the probability of the planar fault. Hence, in fcc materials, both twin boundaries

and stacking faults yield broadening of the diffraction profiles. However, the former defects have symmetrical diffraction peaks with marginal peak shift which can be distinguished from the asymmetric profile shape of stacking faults. The analysis of asymmetry of peak profile helps to correctly interpret the type of stacking faults as the asymmetry for a given reflection is opposite for intrinsic and extrinsic stacking faults.

The effect of planar faults on X-ray diffraction profile can be calculated numerically as a function of the density of planar defects using the DIFFaX (Diffraction of Faulted Crystals) software. DIFFaX obtains the diffraction pattern by the summation of the amplitudes scattered from crystal planes parallel to the planar faults.

The theoretical intensity profile function of planar faults can be described as:

$$I^F(g) = w_\delta I^\delta_{hkl}(g) + \sum_{j=1}^{N} w_L^j I^j_{L,hkl}(g), \tag{2.18}$$

where I^δ_{hkl} is the Dirac delta-function component of the profile at the exact Bragg position and $I^j_{L,hkl}$ are the Lorentzian profile functions of the broadened and shifted sub-reflections, and $w_\delta$and w_L^j are the fractions of the different sub-reflection components [178]. The fractions are given by the relative multiplicities of sub-reflections within a hkl reflection.

2.2.2.4 X-ray Diffraction Experimental Setup and Evaluation

The XRD measurements were conducted by a high-resolution rotating anode diffractometer (manufacturer: Rigaku) with $CuK_{\alpha 1}$ radiation (wavelength: λ=0.15406 nm). The Debye–

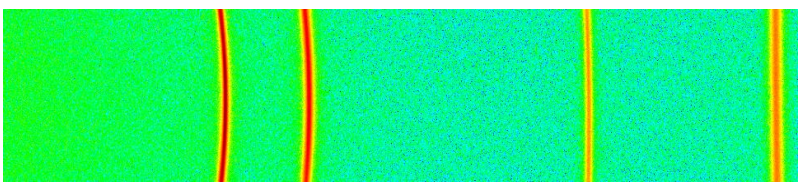

Fig. 2.1: Parts of Debye–Scherrer diffraction rings detected on an imaging plate.

Scherrer diffraction rings were detected by two-dimensional imaging plates, and the line profiles were determined as the intensity distributions perpendicular to the rings obtained by integrating the two-dimensional intensity distributions along the rings.

The evaluation of the patterns was carried out by the Convolutional Multiple Whole Profile (CMWP) fitting method [179]. In this procedure, the experimental diffraction pattern is fitted by the sum of a background spline and the convolution of the instrumental pattern and the theoretical line profiles related to crystallite size, dislocations and planar faults. The instrumental broadening was negligible, compared to the physical peak broadening due to the UFG microstructure of the samples, and therefore an instrumental correction was not necessary. The theoretical line profile functions used in this fitting procedure were based on a model of the microstructure where the crystallites have spherical shape and a log-normal size distribution. The microstructures of the SPD-processed and the electrodeposited Ni-Mo alloys were studied by XLPA. For the HPT-processed samples, the XLPA investigations were carried out at the center, half-radius and periphery of the disks. The following parameters of the microstructure were determined by the CMWP fitting procedure: the area-weighted mean crystallite size ($\langle x \rangle_{area}$), the twin fault probability (β), the average dislocation density (ρ) and the dislocation arrangement parameter M. The twin fault probability in fcc materials is defined as the relative fraction of twin boundaries among the {111} lattice planes. The value of parameter M reflects the arrangement of the dislocations. Thus, a smaller value of M relates to a more shielded strain field of the dislocations and the arrangement of dislocations into low energy configurations, such as LAGBs or dipoles, yields a consequent decrease in M.

2.2.3 Scanning Electron Microscopy

SEM is one of the most versatile instruments for the characterization of the microstructural morphology and the chemical composition. The microstructures of the initial and the HPT-

processed Ni-Mo disks, as well as thin films, were investigated using a FEI Quanta 3D scanning electron microscope. Before EBSD investigations, the surfaces of the initial and HPT-processed disks were first mechanically polished with 600, 1200, 2500 and 4000 grit SiC abrasive papers and then the surface treatment was continued by polishing with a colloidal silica suspension (OP-S) having a particle size of 1 μm. Finally, electropolishing of the surfaces was conducted at 28 V and 1 A using an electrolyte with a composition of 70% ethanol, 20% glycerine and 10% perchloric acid (in vol%).

2.2.3.1 Electron Backscatter Diffraction

EBSD enables the specimen microstructure to be analyzed, visualized and quantified. It can be used for the characterization of the grain boundary misorientations, global/local texture and phase identification. The EBSD images were evaluated using the Orientation Imaging Microscopy (OIM) software.

The microstructures of the initial and the HPT-processed disks were investigated by EBSD with a step size of ~30 nm. The average grain sizes and the fractions of the LAGBs and HAGBs were determined from the EBSD images by investigating the misorientations in the SPD-processed microstructures. The grains were considered as the regions in the EBSD images bounded by HAGBs having misorientations higher than 15°. The number-averaged grain size values were determined by the OIM software.

The grain size of the as-deposited layer samples could not be determined by EBSD due to the very small grain size values (20-30 nm). However, after DSC annealing, the grain size was large enough (400-800 nm) for the characterization by EBSD. The step size in EBSD study for the DSC-annealed layers was 50 nm.

2.2.3.2 Energy Dispersive X-ray Spectroscopy

The chemical compositions of the layers and the HPT-processed Ni alloys were determined by EDS. This technique uses the X-ray spectrum emitted by the bombardment of solid samples with a focused beam of electrons and provides localized chemical analysis. It is noted that the same device was used for the EBSD analysis. In principle, it can be used to detect all the elements from atomic number 4 (Be) to 92 (U).

2.2.4 Transmission Electron Microscopy

Transmission electron microscopy (TEM) technique was applied to determine the grain size of the as-deposited Ni-Mo thin films as other microscopic techniques could not be effectively used for grain size less than 30 nm. For this purpose, the TEM samples were thinned by ion milling with continuous cooling using liquid nitrogen to avoid any unwanted annealing of the nanocrystalline samples. The TEM examinations were performed in a Philips CM20 electron microscope operating at 200 keV. The images and the diffraction patterns were recorded on imaging plates, and the ProcessDiffraction program was used for indexing the diffraction patterns.

2.2.5 Differential Scanning Calorimetry

Differential scanning calorimetry (DSC) was used to investigate the thermal stability of the phase composition and the microstructure of specimens prepared by bottom-up and top-down approaches. For HPT-processed materials, small samples were cut from the region between the half radius and the periphery of the disks processed by 20 turns. This region was intentionally selected as the microstructure corresponding to the HPT-processed specimens with both low

and high Mo contents achieved a saturation state between the half-radius and the periphery of the disks processed for 20 turns of HPT. The DSC experiments were performed using a Perkin Elmer (DSC2) calorimeter at a heating rate of 40 K/min under an Ar atmosphere. The upper limit of temperature for this calorimeter was 1000 K. The same conditions of DSC annealing were applied on small parts of the electrodeposited layers after removing the Cu substrate. Furthermore, this technique was also employed for the calculation of stored energy on both electrodeposited and SPD-processed samples.

2.2.6 Characterization of Mechanical Properties

2.2.6.1 Microhardness Testing

The microhardness of the SPD-processed samples was determined using a Zwick Roell ZHμ hardness tester with a Vickers indenter, an applied load of 500 g and a dwell time of 10 s. Due to the anticipated gradient in the microstructure along the radius of the HPT disks, the hardness was measured at the center, half-radius and periphery of the HPT-processed samples as well as annealed samples. The same method was applied to thin films, however a load of 25 g was applied due to the low thickness of these samples.

2.2.6.2 Tensile Testing

Tensile specimens were prepared from the samples processed by 20 turns of HPT and from the samples processed through 20 turns of HPT and then annealed at the characteristic temperatures determined by DSC.

Two miniature tensile specimens were cut from each HPT-processed disk by electro-discharge machining (EDM). These two miniature tensile specimens were cut symmetrically on either side of the center of the disk as shown in Fig. 2.2.

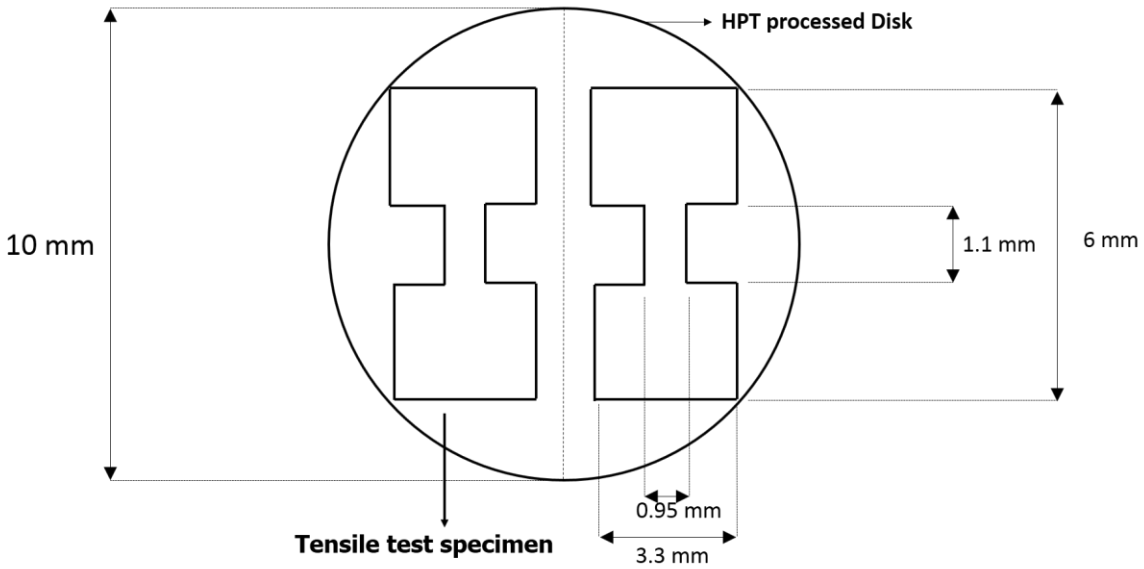

Fig. 2.2: The tensile test specimens cut from the HPT processed disks.

The thickness of the HPT-processed disk was ~0.80 mm. However, as a consequence of the elastic distortion of the anvils during HPT, the surface of the HPT processed disk became curved. So, the upper and lower surfaces of the HPT-processed disks were ground using abrasive papers to a thickness of ~0.60 mm before EDM cutting in order to obtain a uniform thickness and remove any surface irregularities. The gauge length and width of the tensile specimens were 1.1 and 0.95 mm, respectively. Tensile tests were performed on a Zwick Z030 testing machine. All miniature tensile specimens were pulled to failure at RT with an initial strain rate of 10^{-3} s^{-1}.

Chapter 3: Effect of Mo addition on the microstructure and thermal stability of SPD processed Ni alloys

In this chapter, the impact of varying Mo contents on the microstructure and hardness of a UFG Ni alloy processed by SPD is shown. The evolution of microstructure, including grain size and dislocation density, with increasing SPD straining, was characterized using different experimental methods. In addition, the hardness values were investigated both for the cryorolled samples and for HPT processed disks, as a function of the number of revolutions and the distance from the center of the disks. The yield strength was determined and correlated to the dislocation density. The influence of Mo alloying on the thermal stability of HPT-processed UFG Ni alloys is included in this chapter. The evolution of grain size and dislocation density were also investigated as a function of the annealing temperature and then correlated to the evolved DSC peaks. Furthermore, the variation of the strength and ductility during annealing of SPD-processed UFG Ni-Mo alloys was investigated by tension. The influence of Mo alloying on annealing-induced hardening in UFG Ni is also discussed.

3.1. Microstructure Evolution with Addition of Mo in SPD-Processed Ni Alloys

3.1.1 Lattice Parameter of the SPD-Processed Ni Alloys

The cryorolled and the HPT processed Ni alloys were investigated by XRD to determine the average lattice parameters. The values of the lattice parameter for both the cryorolled and the HPT-processed specimens were 0.3527 ± 0.0002 and 0.3549 ± 0.0002 nm for the LMo-HPT and HMo-HPT alloys, respectively. These values deviate from the lattice constant of pure Ni (0.3524 nm) because of the considerable alloying elements that are concentrated in these alloys. Indeed, the EDS results in Table 3.1 reveal that both materials contain Mo, Al, Si and Fe, but

the most significant difference between the compositions is the highest Mo content in sample HMo. It was reported that the addition of Mo, Al and Fe to Ni increases the lattice parameter while alloying with Si leads to a decrease of the lattice constant [180].

Table 3.1: Chemical composition of the alloys with low and high Mo contents as determined by EDS.

LMo alloy					
Element	Ni	Mo	Al	Si	Fe
At.%	98.29	0.28	0.84	0.34	0.25
HMo alloy					
Element	Ni	Mo	Al	Si	Fe
At.%	93.70	5.04	1.08	0.05	0.13

In the present alloys, the largest effects on the lattice parameter are caused by the additions of Mo and Al, whereas the effects of Fe and Si approximately compensate each other. Therefore, the lattice parameter of the present alloys may be estimated as:

$$a = 0.3524 + 0.0478 \cdot \mathrm{x}_{Mo} + 0.0179 \cdot \mathrm{x}_{Al}\,, \tag{3.1}$$

where x_{Mo} and x_{Al} are the mole fractions of Mo and Al, respectively. Using the concentration values in Table 3.1, eq. (3.1) gives estimates of 0.3527 and 0.3550 nm for the lattice parameters of the LMo and HMo alloys, respectively, and these values agree with the measured lattice constants within experimental error. This agreement between the measured and the calculated lattice parameters indicates that all of the alloying elements are in solid solution. Thus, as the equilibrium solubility limit of Mo in Ni is only about 0.6 at.%, the HMo alloy is a supersaturated solid solution.

3.1.2 Characterization of the Microstructure for Cryorolled and HPT-Processed Ni Alloys by EBSD

Fig. 3.1 shows EBSD images obtained from the cryorolled LMo (a and b) and HMo (c and d) alloys. The HAGBs are indicated by black lines in the images.

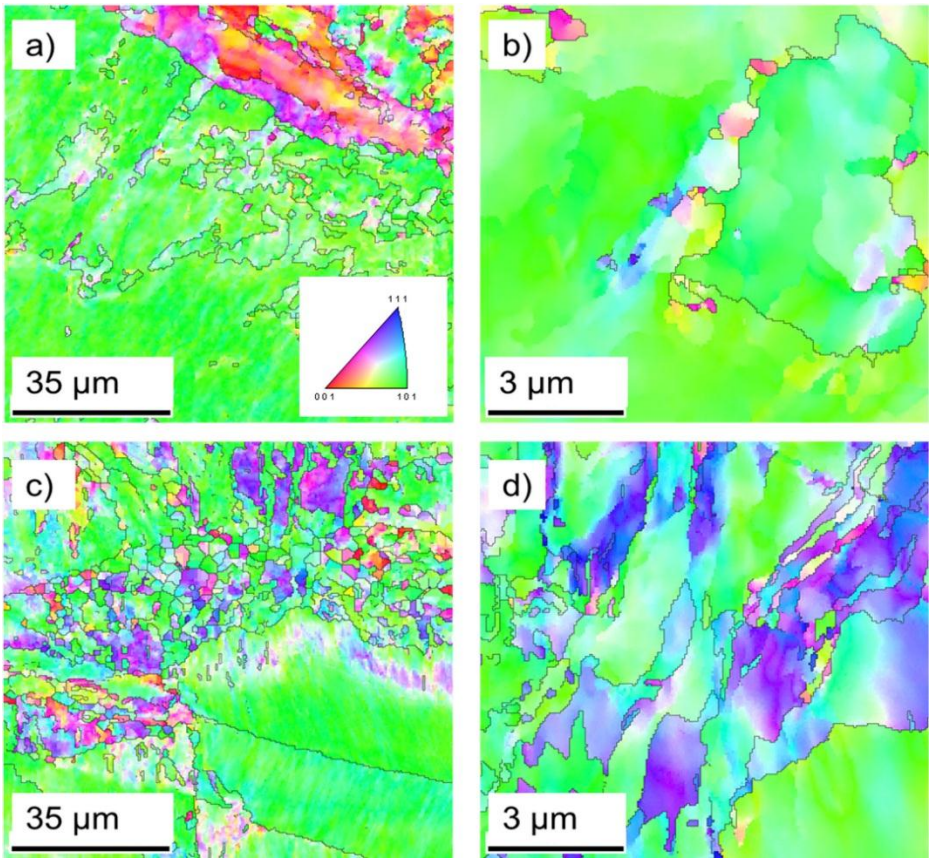

Fig. 3.1: EBSD images for the cryorolled LMo (a and b) and HMo (c and d) Ni alloys. The HAGBs are indicated by black lines.

For each alloy, two images are shown with low (Figs. 3.1 a and c) and high magnifications (Figs. 3.1 b and d) due to the complex nature of the microstructures. Indeed, the low magnification images in Figs. 3.1 a and c reveal that there are large grains with the dimensions of several tens of microns while in other regions the grain size is only a few microns. The high magnification images in Figs. 3.1 b and d show that there are grains which are even smaller than one micron in the LMo and HMo alloys, respectively. The average grain sizes for the cryorolled LMo and HMo samples were ~4.1 and ~3.8 µm, respectively.

The microstructure evolutions in the LMo-HPT and HMo-HPT alloys during HPT are illustrated by the EBSD images in Figs. 3.2 and 3.3 where these images correspond to the centers (on the left) and the peripheries (on the right) for the lowest and the highest numbers of HPT turns corresponding to (a,b) 1/2 and (c,d) 20 revolutions, respectively. For better visibility of the grains in the centers of the disks processed by ½ turn, the HAGBs are indicated by black lines.

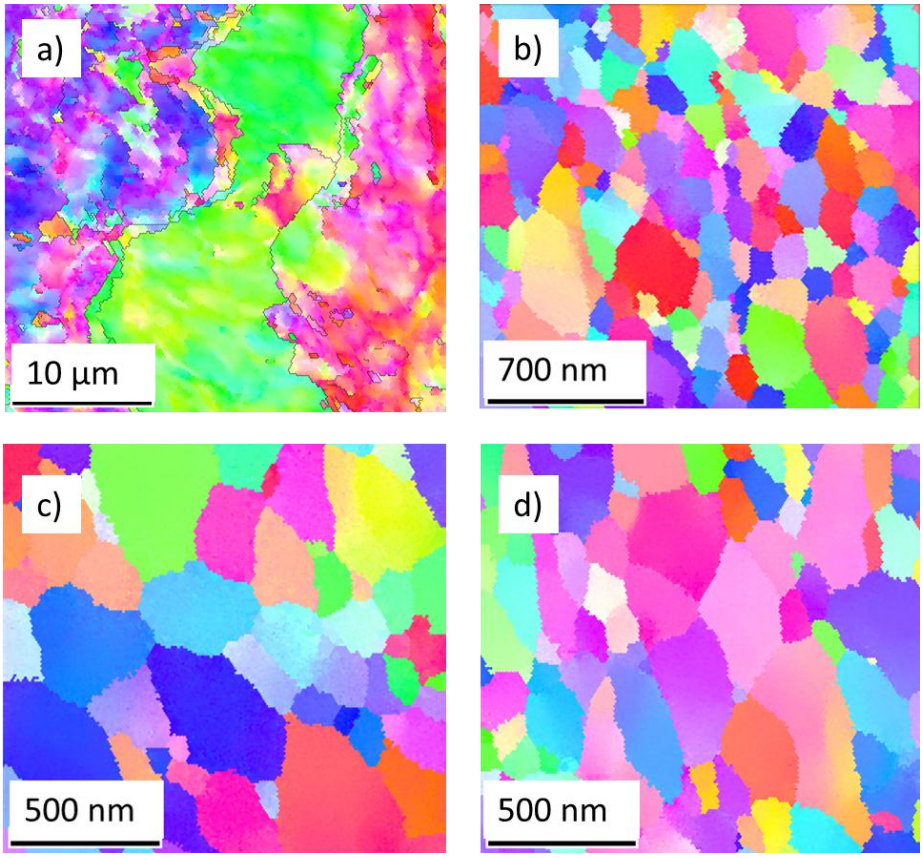

Fig. 3.2: EBSD images for the LMo-HPT alloy processed by HPT: center (a) and periphery (b) for 1/2 turn, and center (c) and periphery (d) for 20 revolutions.

The grain size values determined for these two alloys in the disk center, half-radius and periphery positions for 1/2, 5 and 20 HPT turns are plotted in Fig. 3.4 (a) and (b) for the LMo-HPT and HMo-HPT alloys, respectively.

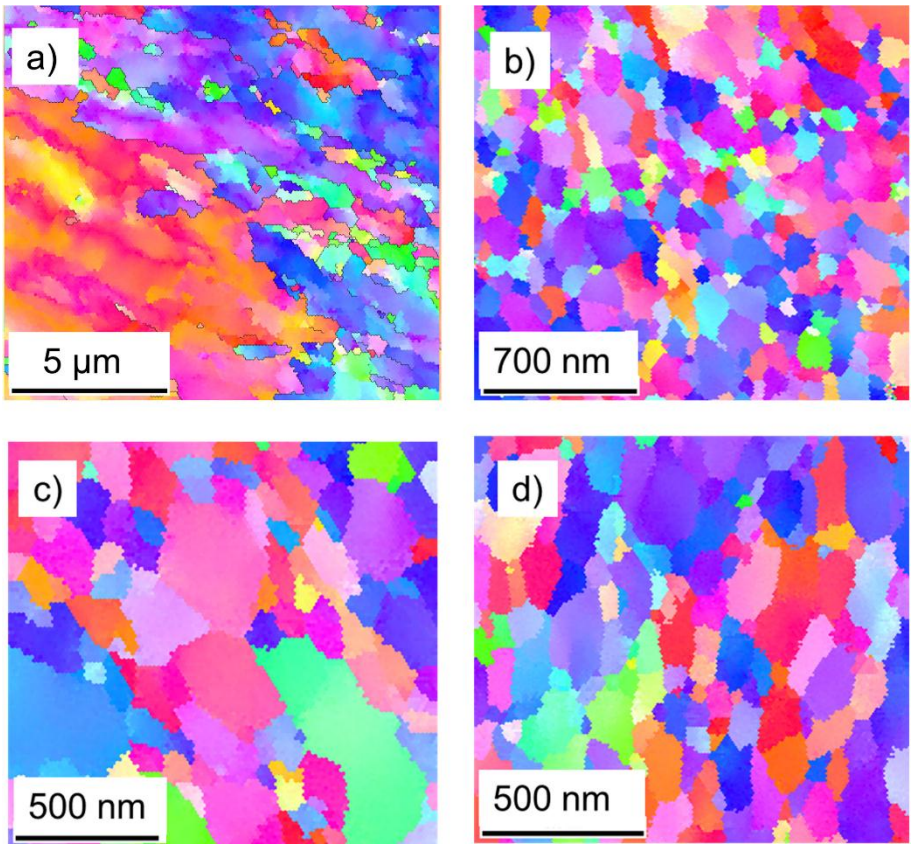

Fig. 3.4: EBSD images for the HMo-HPT alloy processed by HPT: center (a) and periphery (b) for 1/2 turn, and center (c) and periphery (d) for 20 revolutions.

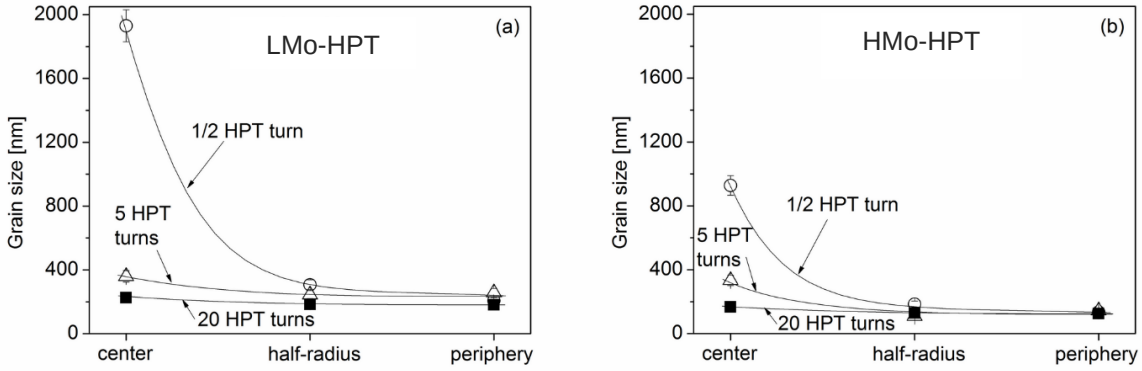

Fig. 3.3: The grain size in the center, half-radius and periphery for the LMo-HPT (a) and HMo-HPT (b) disks processed by different turns of HPT. The scales of the vertical axes in the two images are the same for an easier comparison of the different grain size values in the LMo-HPT and HMo-HPT alloys.

For the LMo-HPT alloy, a significant grain refinement was observed in the center of the disk processed by ½ turn since the grain size decreased to ~1.9 μm, and at the periphery, the grain

size was even smaller at ~205 nm due to the higher applied shear strain. For 20 turns, the microstructure became more homogeneous along the disk radius, and the grain sizes in the center and the periphery were ~225 and ~180 nm, respectively. For the HMo-HPT alloy, there were much smaller grain sizes in the center (~930 nm) and at the periphery (~135 nm) after ½ turn than for the LMo-HPT alloy because of the higher Mo content. With increasing numbers of turns to 20 for the HMo-HPT alloy, the grain sizes in the center and periphery were further refined to ~170 and ~125 nm, respectively. These values are considerably smaller than the grain sizes obtained for the LMo-HPT alloy, but for both compositions the grain size decreases with both increasing distance from the disk center and increasing numbers of turns. It is apparent from these measurements that the higher Mo content yielded ~30% smaller saturation grain size, and for this alloy the grain size at the periphery saturated after approximately ½ turn of HPT.

The fraction of HAGBs was also determined from the EBSD images for the cryorolled and HPT-processed LMo-HPT and HMo-HPT specimens. Fig. 3.5 shows the HAGB fraction for the center, half-radius and periphery of the disks processed for ½, 5 and 20 turns. After cryorolling, the fractions of HAGBs were only ~11 and ~16% for LMo and HMo, respectively. HPT processing produced a significant increase in the HAGB fraction for both compositions. With increasing distance from the disk center and the number of turns, the fraction of HAGBs was further increased. A maximum HAGB fraction of about ~70% was achieved at the periphery even after ½ turn. For 20 turns of HPT, saturations were achieved in both alloys at the half-radius positions. Finally, it is important to note there are no significant differences between the saturation values of the HAGB fractions in the LMo-HPT and HMo-HPT alloys.

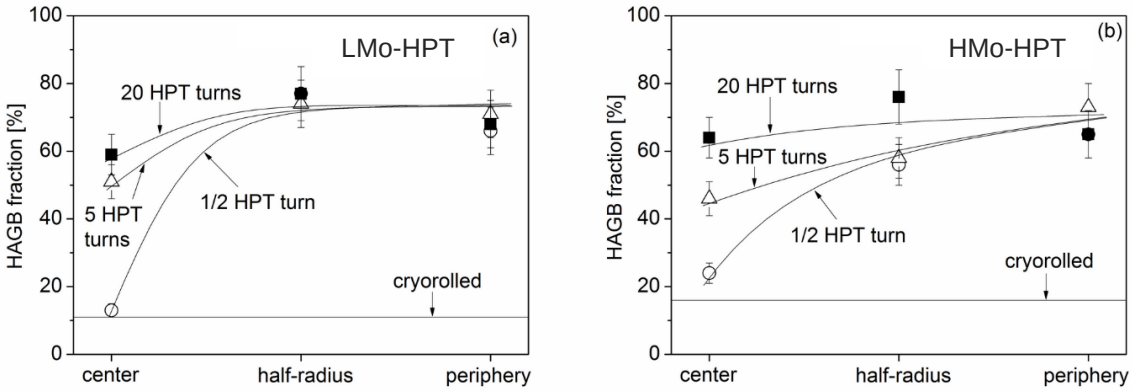

Fig. 3.5: HAGB fraction in the center, half-radius and periphery for the LMo-HPT (a) and HMo-HPT (b) disks processed by different turns of HPT. The HAGB fractions for the cryorolled alloys are also indicated by the horizontal lines.

3.1.3 Influence of Mo Content on Density and Arrangement of Dislocations

The dislocation densities and the dislocation arrangement parameters for the cryorolled and HPT-processed LMo-HPT and HMo-HPT alloys were determined by XLPA. Fig. 3.6 illustrates the CMWP fitting for the HMo-HPT alloy in the center of the disk processed by 20 HPT turns. The open circles and the solid line correspond to the measured and fitted intensity profiles, respectively. In the cryorolled LMo and HMo alloys, the dislocation density values were ~15 × 10^{14} m^{-2} and ~35 × 10^{14} m^{-2}, respectively. The higher dislocation density in the alloy containing the larger Mo content is due to the stronger effect of the larger Mo solute atoms in impeding dislocation annihilation during cryorolling.

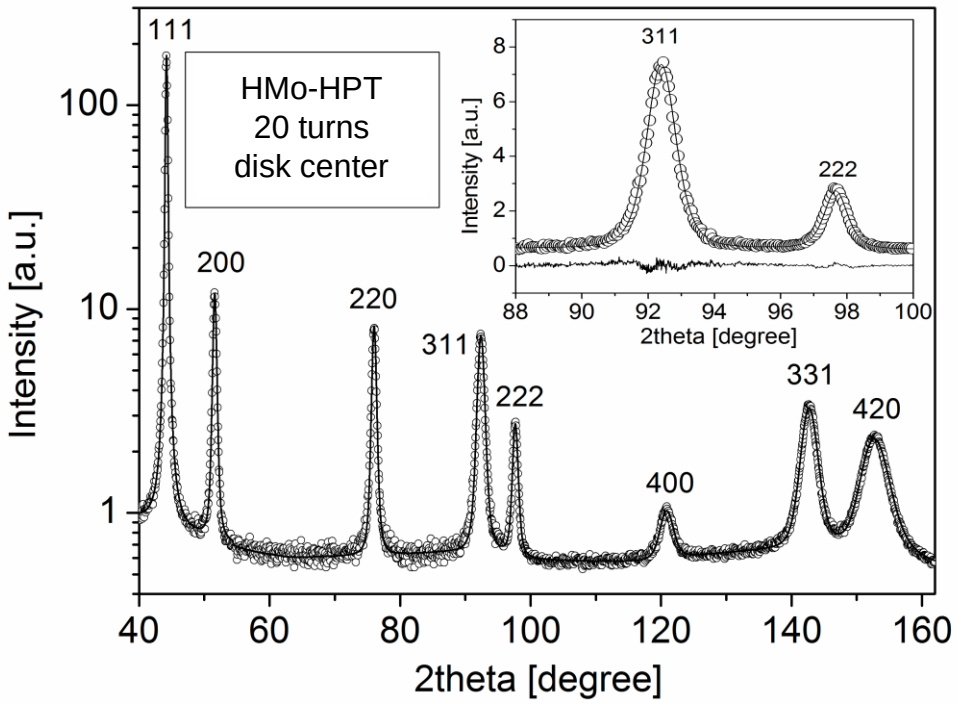

Fig. 3.6: CMWP fitting of the X-ray diffraction pattern taken in the center of the HMo-HPT alloy disk processed by 20 turns of HPT. The open circles and the solid line represent the measured data and the fitted curve, respectively. The intensity is in a logarithmic scale. The inset shows a magnified part of the diffractogram in a linear intensity scale where the difference between the measured and the fitted patterns is also given at the bottom of the image.

Fig. 3.7 shows that HPT processing led to a further enhancement in the dislocation density. For the LMo-HPT alloy, an early saturation of the dislocation density was observed, and its value changes only slightly either along the disk radius or as a function of the number of HPT turns. The maximum dislocation density in the LMo-HPT alloy achieved by the subsequent application of cryorolling and HPT was ~27×10^{14} m^{-2}. For the HMo-HPT alloy processed by ½ turn, the dislocation density was significantly enhanced with increasing distance from the center and reached a value of ~59×10^{14} m^{-2} at the disk periphery. This value can be regarded as the saturation value of the dislocation density for the HMo-HPT alloy since after 5 and 20 turns the dislocation density did not exceed this value, but it became more homogeneous along the disk radius. Thus, it is concluded that the higher Mo content yielded a larger dislocation density by a factor of two in the alloys processed by the subsequent application of cryorolling and HPT and this is attributed to the pinning effect of the solute Mo atoms on dislocations. The use of XLPA permits a determination of the dislocation arrangement parameter, *M*, and after cryorolling and HPT the values of *M* were in the ranges of ~2.3 ± 0.6 and ~5.0 ± 0.5 for the LMo-HPT and HMo-HPT alloys, respectively. The higher *M* value for HMo-HPT alloy is also explained by the pinning effect of the solute Mo atoms on the dislocations, which impedes their re-arrangement into low energy configurations.

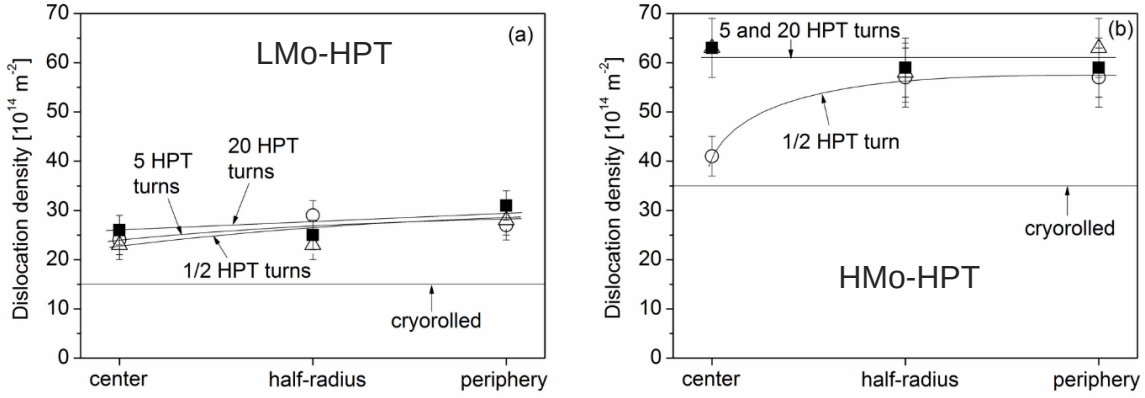

Fig. 3.7: The dislocation density in the center, half-radius and periphery for the LMo-HPT (a) and HMo-HPT (b) disks processed by different turns of HPT. The scales of the vertical axes in the two images are the same for an easier comparison of the very different dislocation density values in the LMo-HPT and HMo-HPT alloys. The dislocation densities for the cryorolled alloys are also indicated by the horizontal lines.

In addition to the density and the arrangement parameter of dislocations, the crystallite size was also determined from an analysis of the X-ray diffraction peak profiles. The average crystallite sizes were ~40 and ~30 nm for the LMo-HPT and HMo-HPT alloys processed by the consecutive application of cryorolling and HPT, respectively. There were no major changes in the crystallite size with increasing distance from the center or with the number of turns. Both the values of the crystallite sizes determined by XLPA and their evolutions with increasing strain were different from the grain sizes obtained by EBSD. This difference is due to the hierarchical microstructure in SPD-processed metals where the grains are subdivided into subgrains and/or dislocation cells, which scatter X-rays incoherently [173]. Therefore, XLPA measures the size of the subgrains and cells as the crystallite size, also defined as the coherently-scattered domain size, and this is smaller than the grain size in SPD-processed materials. The twin fault probability in both LMo-HPT and HMo-HPT alloys processed by SPD was under the detection limit of the present XLPA method (0.1%), indicating that twinning has no significant role in cryorolling and HPT processing of these alloys.

3.2. Annealing of Low-Mo and High-Mo Samples Processed by HPT

3.2.1 DSC Analysis of the HPT-Processed Low-Mo and High-Mo Samples

The thermal stability of the UFG microstructures was studied only for the materials between the half-radius and the periphery of the disks processed by 20 turns of HPT since in this region the grain size and the defect structure get saturated. Fig. 3.8 shows DSC thermograms taken at a heating rate of 40 K/min for the LMo-HPT and HMo-HPT alloys processed by HPT for 20 turns. The heat flow versus temperature curves were plotted after baseline subtraction. The baseline was determined from a second heating experiment. It is noted that for the LMo-HPT alloy the DSC trace displays an endothermic trend at about 627 K due to the Curie transition from a ferromagnetic to a paramagnetic state. This endothermic peak was also observed in the second DSC scan, therefore after the subtraction of the second heating scan from the first scan, the resultant data were free of the signal of the Curie transition. For the HMo-HPT alloy, the endothermic peak of the ferromagnetic to paramagnetic transition was not observed. This is in line with former studies (for example, Ref. [181]) which indicated that ~5 at.% Mo alloying led to a considerable reduction in the Curie temperature to 333 K, so that the paramagnetic

transition cannot be observed in the present experiments starting at 300 K due to the transient DSC signal at the beginning of the measurements.

Fig. 3.8 shows that for the LMo-HPT sample, there was a single exothermic DSC peak with a long tail part at the left side of the peak. Between ~400 and ~600 K only a weak exothermic signal was detected. The majority of the peak appeared between ~600 and ~830 K. The exothermic peak has a shoulder at the left side, and its maximum was observed at a temperature of ~743 K.

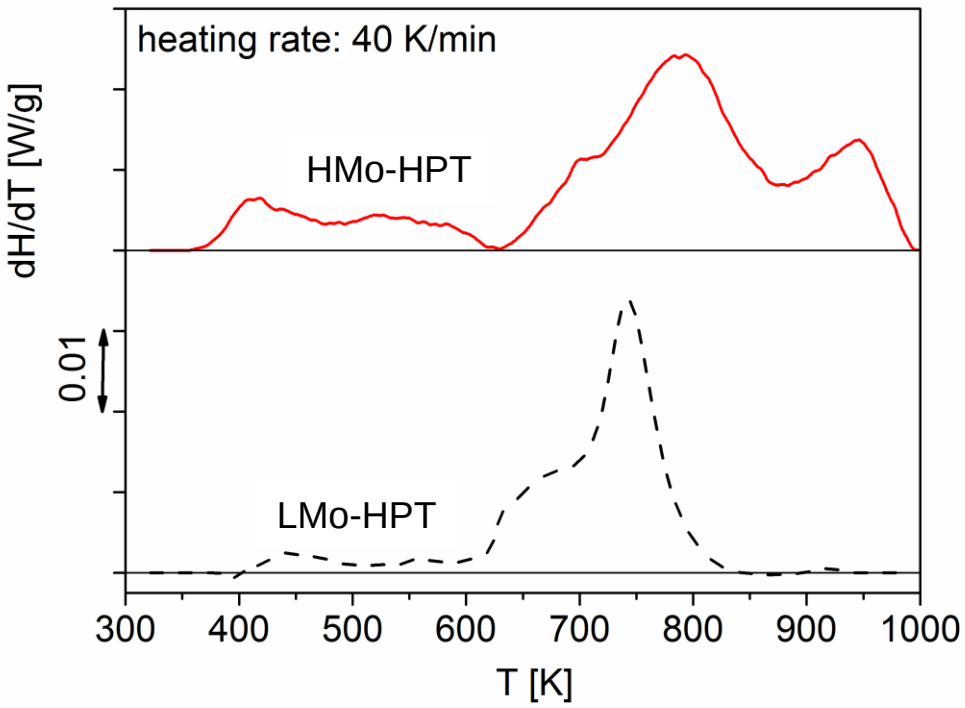

Fig. 3.8: DSC thermograms obtained at a heating rate of 40 K/min for the LMo-HPT and HMo-HPT alloys processed by 20 HPT turns.

For the HMo-HPT specimen, between ~360 and ~630 K the exothermic signal was weak while in the temperature range of 630–1000 K two main exothermic DSC peaks were detected. The first peak was observed between ~630 and ~875 K while the second peak evolved between ~875 K and ~1000 K. The peak maxima for these two peaks were found at ~786 K and ~946 K. Such exothermic peaks are usually related to the recovery and recrystallization of the SPD-processed

microstructures. Therefore, it may be concluded that the increase in Mo content resulted in a shift of the exothermic signal to higher temperatures, and thus the Mo alloying improved the stability of the UFG microstructures in Ni. In order to reveal the processes related to the exothermic peaks, the microstructure evolution was studied as a function of annealing temperature, and the results are presented in the next sections.

3.2.2 Microstructure Evolution During Annealing

The XRD patterns (an example is shown in Fig. 3.9) indicated that both HPT-processed alloys remained single phase fcc solid solutions during DSC annealing up to 1000 K.

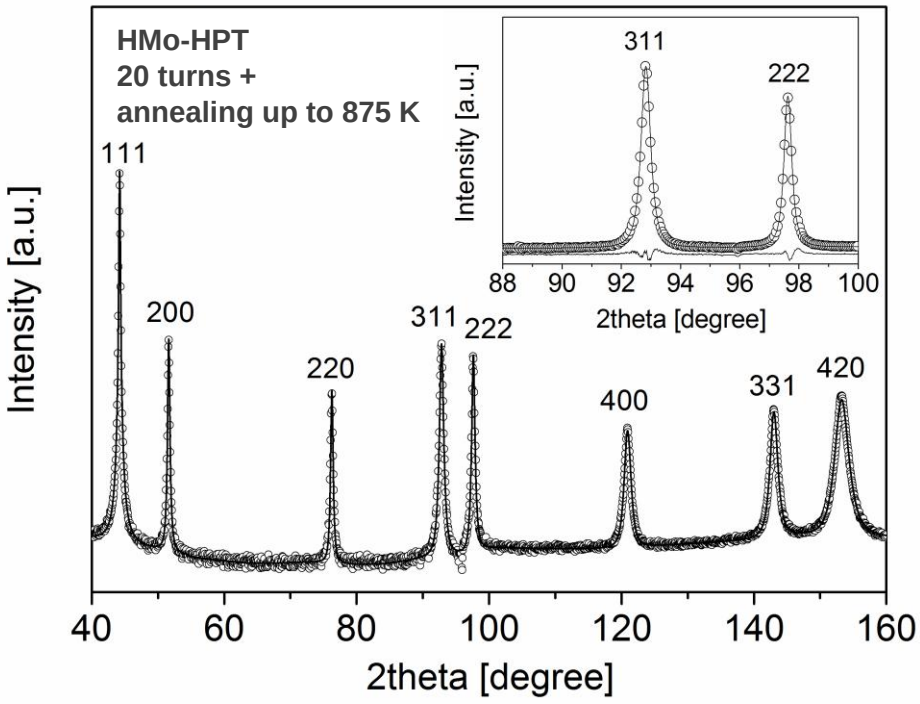

Fig. 3.9: CMWP fitting on the diffraction pattern taken on the HMo-HPT alloy processed by 20 turns of HPT and heated up to ~875 K. The open circles and the solid line represent the measured and the fitted patterns, respectively. The intensity is plotted in logarithmic scale. The inset shows reflections 311 and 222 with higher magnification and linear intensity scale. The difference between the measured and fitted diffractograms is shown at the bottom of the inset.

Fig. 3.10 shows the evolution of the dislocation density as a function of the annealing temperature together with the DSC curves for both alloys. Before annealing, the dislocation density values were ~27 × 10^{14} m^{-2} and ~59 × 10^{14} m^{-2} in the LMo-HPT and HMo-HPT alloys, respectively. The more than two times larger dislocation density in the HMo-HPT material is attributed to the hindering effect of Mo solute atoms on the annihilation of dislocations during HPT processing. The heat treatment of the samples led to a gradual reduction in the dislocation density with increasing annealing temperature. For both samples, the dislocation density decreased by about 30–40% up to the onset of the large exothermic DSC peaks at 600–630 K.

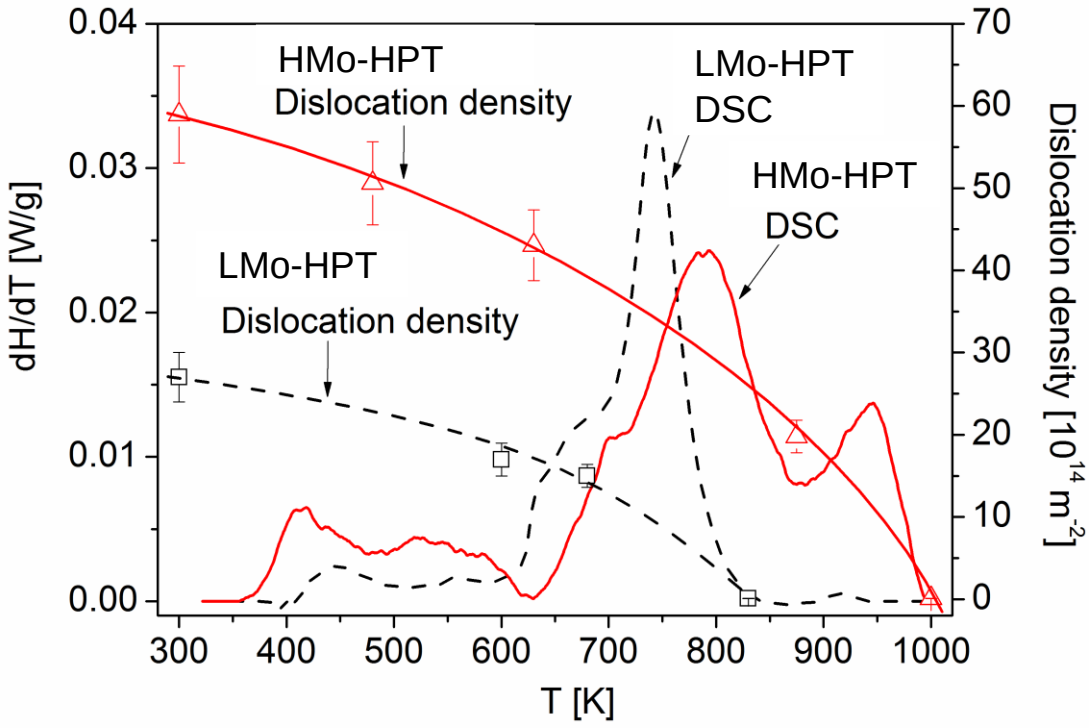

Fig. 3.10: The average dislocation density obtained by XLPA as function of annealing temperature for the LMo-HPT and HMo-HPT alloys processed by 20 HPT turns. The corresponding DSC thermograms are also shown in the figure.

For the LMo-HPT sample, at the end of the exothermic DSC peak at ~830 K, the dislocation density fell below the detection limit of the present XLPA method (~10^{13} m^{-2}), thereby suggesting the completion of recovery in the microstructure. For the HMo-HPT material, the dislocation density decreased to ~20 ×10^{14} m^{-2} after the first DSC peak at ~875 K, thereby

indicating a partial recovery of the microstructure. The value of the dislocation density reduced further with increasing annealing temperature and reached a value below ~10^{13} m^{-2} at the end of the second exothermic DSC peak at ~1000 K.

It is shown in Fig. 3.11 that, in addition to the reduction of the dislocation density, the dislocation arrangement parameter decreased continuously with increasing annealing temperature. The reduction of the value of *M* indicates a higher shielding of the strain field of dislocations, which suggests their arrangement into low energy configurations such as LAGBs and/or dipolar dislocation walls. Therefore, in both alloys during the recovery of the UFG microstructures there are simultaneous annihilations and clustering of dislocations.

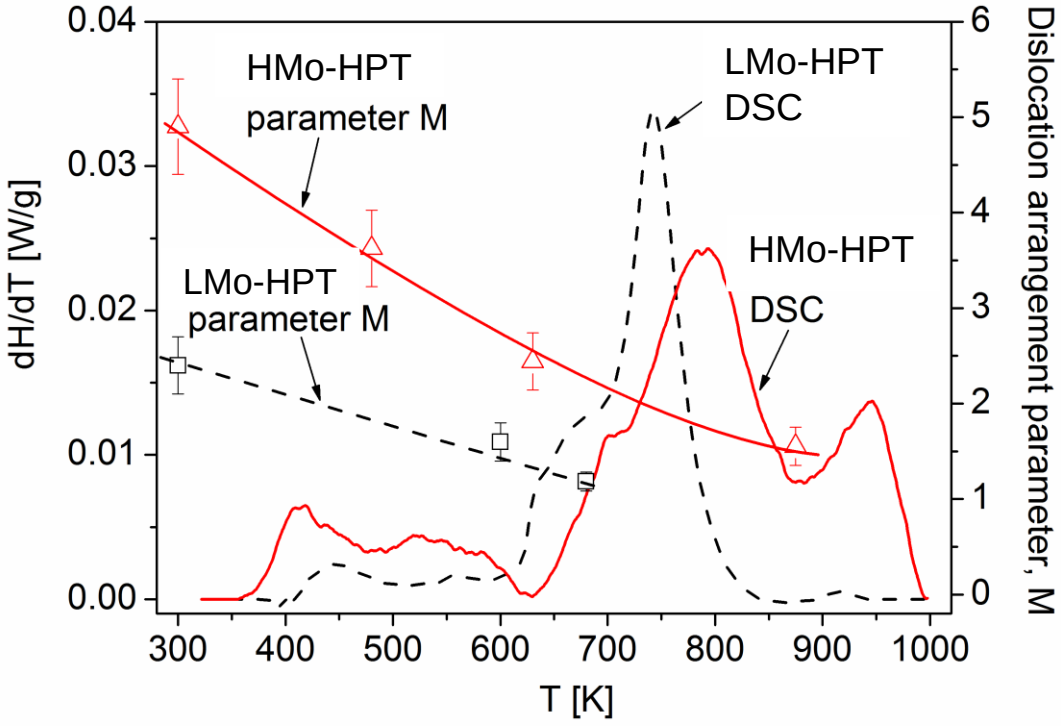

Fig. 3.11: The dislocation arrangement parameter obtained by XLPA as function of annealing temperature for the HPT-processed LMo-HPT and HMo-HPT alloys. The corresponding DSC thermograms are also shown in the figure.

Fig. 3.12 shows inverse pole figure (IPF) maps obtained on the HPT processed LMo-HPT sample and the specimens annealed at two characteristic temperatures of the DSC thermogram (~680 and 830 K).

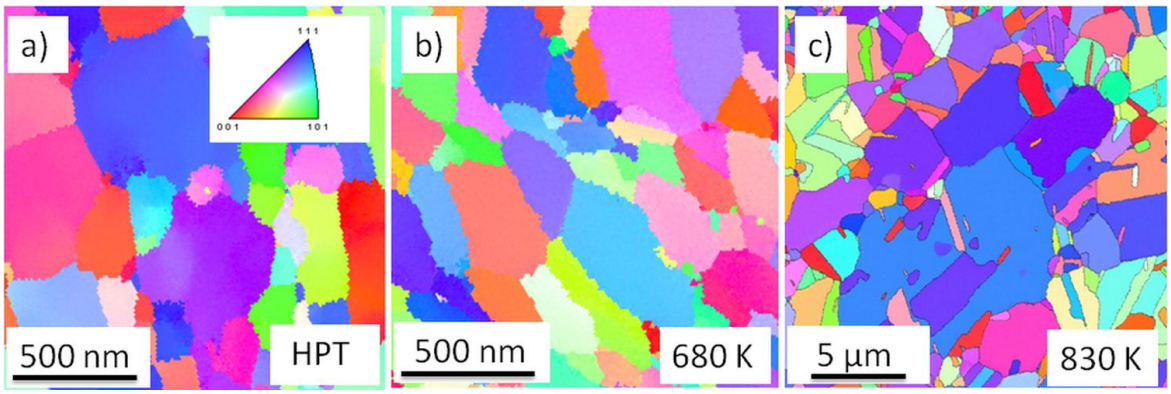

Fig. 3.12: IPF maps showing the grain structure for the LMo alloy after (a) HPT, (b) subsequent annealing at ~680 K and (c) ~830 K. The color code for the maps is shown in the inset in (a). The HAGBs are indicated by black lines.

The grain size values determined from the IPF maps are plotted for the LMo-HPT sample in Fig. 3.13 as a function of the annealing temperature. Immediately after HPT processing, the average size of the grains in the LMo-HPT specimen was ~180 nm. The grain size remained practically unchanged up to ~680 K where this corresponds to the beginning of the high exothermic signal in the DSC peak. Thereafter, the grain size quickly increased from ~180 to ~874 nm. In addition, Fig. 3.12c reveals that most of the grains have straight grain boundaries. These observations suggest that the high exothermic signal observed at the end of the DSC peak is related to the recrystallization of the UFG microstructure in the LMo-HPT alloy.

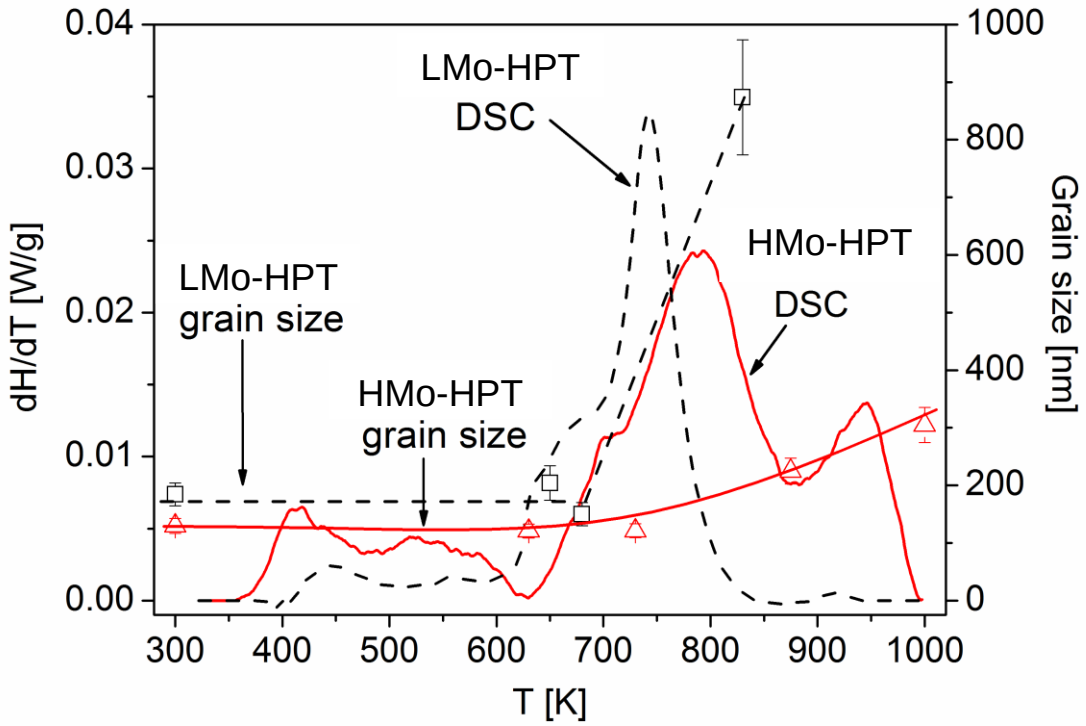

Fig. 3.13: The average grain size determined by EBSD as function of annealing temperature for the LMo-HPT and HMo-HPT alloys. The corresponding DSC thermograms are also shown in the figure.

The IPF maps in Fig. 3.14 show the HPT-processed microstructure in the HMo-HPT alloy and also after annealing up to the characteristic temperatures of the DSC thermogram (~630, 875 and 1000 K). The grain sizes determined from the IPF maps are shown in Fig. 3.13 together with the corresponding DSC curve. Immediately after HPT, the grain size was ~130 nm and remained unchanged within experimental error up to ~730 K. This temperature corresponds to the end of the shoulder at the left side of the first large DSC peak. When the temperature increased up to the end of the first large exothermic peak at ~875 K, the grain size increased moderately from ~130 to ~225 nm. During the second exothermic peak between ~875 and ~1000 K, there was a further increase in grain size to ~305 nm in the HMo-HPT alloy. After annealing up to ~1000 K many of the boundaries seem to be straight (for example, in Fig. 3.14d)

but nevertheless, a considerable fraction of boundaries is curved which suggests that complete recrystallization did not occur even at the end of the thermogram.

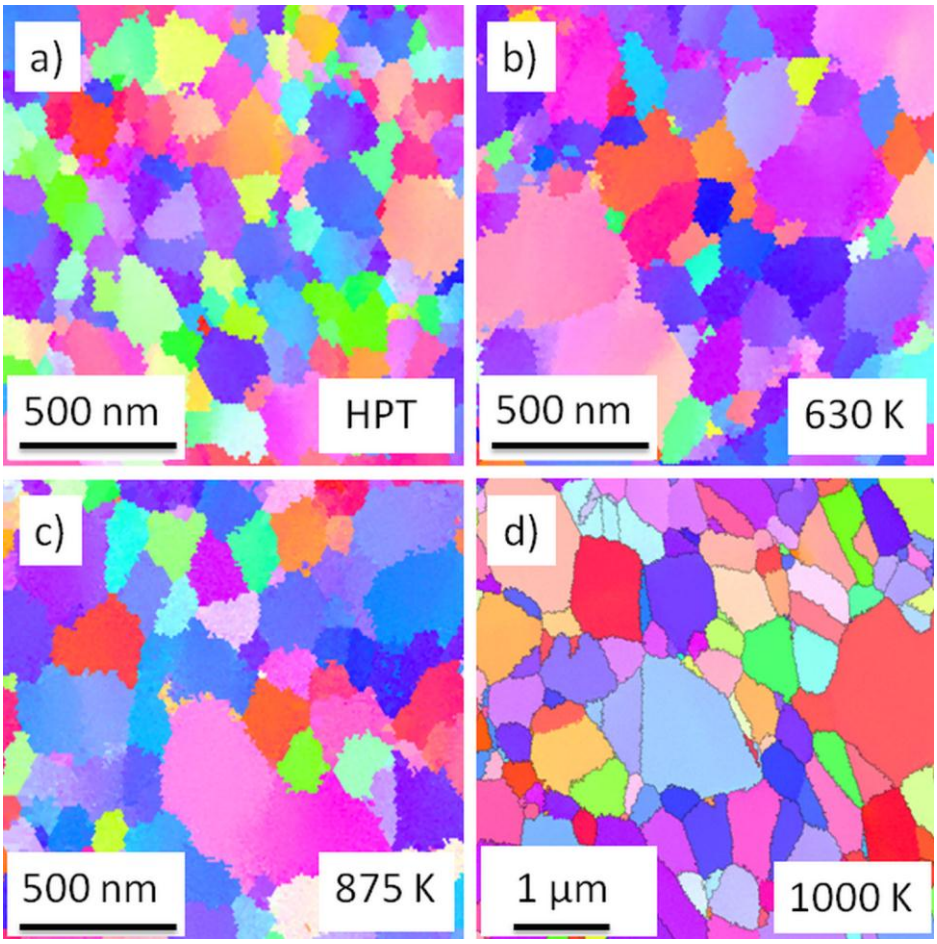

Fig. 3.14: IPF maps showing the grain structure for the HMo alloy after (a) HPT, (b) subsequent annealing at ~630 K, (c) ~875 K and (d) ~1000 K. The color code for the maps is shown in the inset in Fig. 3.12 a. The HAGBs are indicated by black lines.

The fraction of LAGBs was also determined from the EBSD data for the HPT-processed and the annealed LMo-HPT and HMo-HPT specimens and plotted as a function of temperature in Fig. 3.15. After HPT, the LAGB fraction was ~24% for both alloys. First, the LAGB fraction increased with increasing temperature to about 40%, which can be attributed to the arrangement of dislocations into LAGBs within the grains in the first stage of recovery of the HPT-processed microstructures. This trend was observed up to temperatures of ~650 and ~875 K for the LMo-HPT and HMo-HPT samples, respectively. Thereafter, the fraction of LAGBs decreased to

~10% for both samples since the dislocations arranged into LAGBs were annihilated during recrystallization.

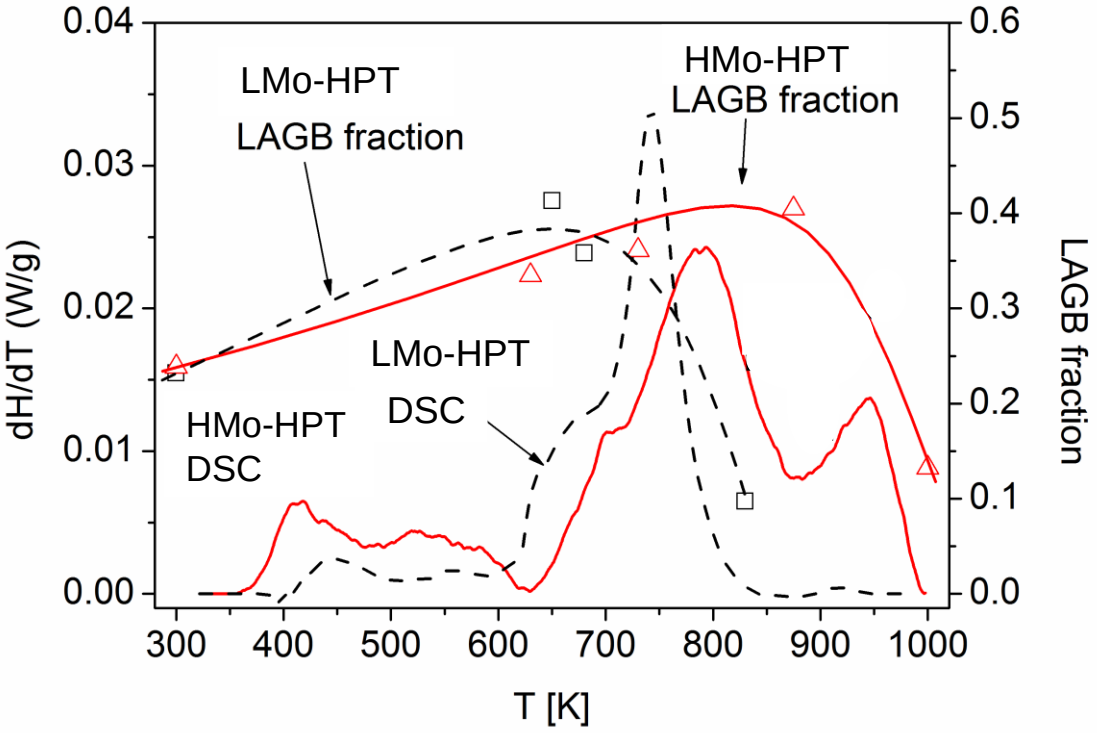

Fig. 3.15: The LAGB fraction determined by EBSD as function of annealing temperature for the LMo-HPT and HMo-HPT alloys. The corresponding DSC thermograms are also shown in the figure.

3.2.3 Thermal Stability

This study revealed that both LMo-HPT and HMo-HPT alloys remain a single phase fcc Ni-Mo solid solution during annealing up to 1000 K. For the LMo-HPT alloy, this observation is in accordance with the equilibrium phase diagram [182]. At the same time, for the HMo-HPT alloy, the phase diagram suggests that a two-phase microstructure with fcc Ni(Mo) solid solution and tetragonal Ni_8Mo intermetallic compound is stable between ~300 and ~500 K. In the temperature range of 500–700 K, the phase diagram predicts a microstructure with fcc Ni(Mo) solid solution and tetragonal Ni_4Mo intermetallic compound. Above ~700 K, the single-phase fcc Ni(Mo) solid solution is stable. The lack of transformation from fcc solid solution to

a two-phase system below ~700 K can be explained by the short term of the present DSC annealing process. In addition, a large amount of Mo may be segregated at the grain boundaries, and this may stabilize the microstructure against recrystallization or phase transformation as revealed by former studies [183–185]. The segregation of alloying elements at grain boundaries may lower the grain boundary energy thereby reducing the thermodynamic driving force for recrystallization.

In addition, the decrease of the grain boundary energy due to segregation hinders the nucleation of the intermetallic compound as the higher alloying element content in the precipitates must be supplied by the solute atoms at the grain boundaries. In accordance with the present study, a recent investigation also showed the absence of precipitation in nanocrystalline Ni-Mo alloys with different Mo contents up to 21.5 at. % annealed at various temperatures up to 1173 K for 1 h [171].

The higher Mo content in the Ni alloy yielded a smaller grain size and a higher dislocation density after HPT processing. This is explained by the retarding effect of solute Mo atoms on the dynamic annihilation of dislocations and the recrystallization during SPD straining. At the same time, the higher dislocation density in the HMo-HPT alloy led to a larger driving force for recovery and recrystallization. The former kinetic and the latter thermodynamic effects hinder and promote the annihilation of dislocations, respectively. It seems that the increase of the Mo content from 0.28% to 5.04% has a similar influence on these two effects at the beginning of DSC annealing as the recovery started at about 400 K for both alloys as revealed by the DSC thermograms in Fig. 3.8. In addition, between ~400 and ~600 K, the relative change of the dislocation density due to recovery was practically the same (about 30–40%) for both alloys. At the same time, the recrystallization occurred at a much higher temperature, and the exothermic DSC signal finished later for the HMo-HPT sample than for the LMo-HPT alloy (see Fig. 3.8). The grain growth during the DSC scan was also less pronounced in the HMo-

HPT material. Thus, it can be concluded that, although the recovery started at similar temperatures for both alloys, the recrystallization occurred at a higher temperature for the HMo-HPT alloy so that the higher Mo content yielded a considerable increase in the thermal stability of the UFG microstructure.

The grain-growth in both alloys was preceded by a reduction in the dislocation density to about one-half of the value measured after HPT and the arrangement of the remaining dislocations into LAGBs as revealed by the decrease of the dislocation arrangement parameter (*M*) and the increase of the LAGB fraction (see Figs. 3.11 and 3.15). When grain growth began, the fraction of LAGBs started to decrease with a concomitant reduction of the dislocation density to practically a zero value. These observations suggest that, in addition to recovery processes, recrystallization also occurred in the temperature ranges of 680–830 K and 875–1000 K for the LMo- and HMo-HPT alloys, respectively. The higher thermal stability of the HMo-HPT material against recrystallization can be explained by the segregation of Mo solute atoms in the grain boundaries which yields both kinetic and thermodynamic retardation of the grain growth, as discussed in the previous paragraphs. In the LMo-HPT alloy annealed up to the end of the exothermic peak at ~830 K, the majority of HAGBs are straight, which suggests complete recrystallization. At the same time, for the HMo-HPT alloy the grain size is much smaller, and many curved grain boundaries were detected in the EBSD images, suggesting that only partial recrystallization occurred in this material. Thus, at the heating rate of 40 K/min full recrystallization can be achieved only at temperatures higher than 1000 K which is above the upper temperature limit of the present DSC facility.

The changes in the microstructures of the HPT-processed LMo- and HMo-HPT alloys during annealing are also reflected in the KAM maps shown in Figs. 3.16 and 3.17, respectively.

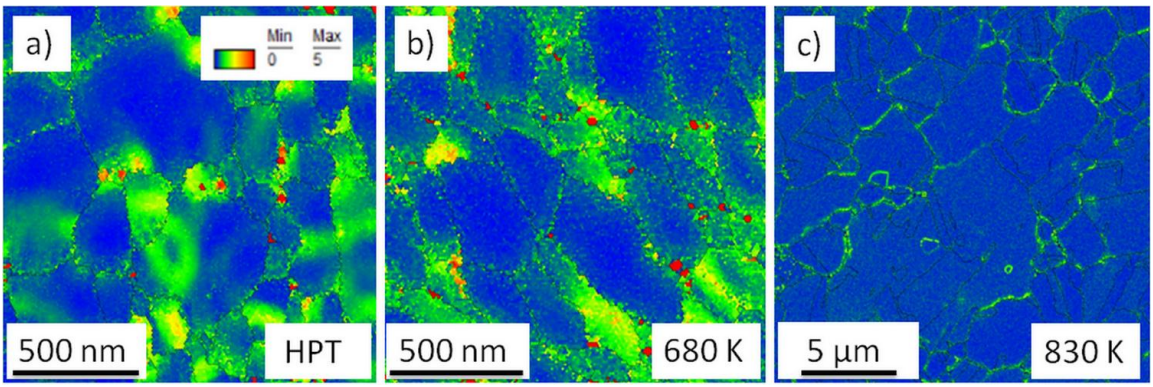

Fig. 3.16: KAM images showing the local misorientations between 0 and 5° for the LMo alloy after (a) HPT, (b) subsequent annealing at ~680 K and (c) ~830 K. The color code for the maps is shown in the inset in (a).The HAGBs are indicated by black lines.

These maps were made on the same areas as those shown in the IPF images of Figs. 3.12 and 3.14 with the HAGBs indicated by black lines. For all HPT-processed or annealed samples, more than 95% of the pixels inside the grains have local misorientations smaller than 5°. Therefore, the KAM maps were prepared for the misorientation angle range between 0 and 5°. The color codes for the different misorientation angles are shown in the inset of Fig. 3.16a. The pixels with local misorientations larger than 5° received the same red color as the pixels with the misorientation of 5°. The KAM maps are indicative of local strains in the studied microstructures. Fig. 3.16a reveals an inhomogeneous spatial distribution of distortion inside the grains for the LMo-HPT alloy processed by HPT. It is noted that, although in some regions low KAM values were observed as indicated by blue color, they may contain high dislocation densities as the statistically stored dislocations are not arranged into LAGBs, and therefore they do not cause local misorientations in the KAM maps. Indeed, XLPA indicated a high dislocation density (~27× 10^{14} m^{-2}) in the LMo-HPT alloy. Until the grain size remained practically unchanged (up to ~680 K), large local misorientation angle values were detected in the KAM maps (see Fig. 3.16b). At the same time, between ~680 K and ~830 K the large exothermic signal and the extensive grain growth were accompanied by a strong reduction of the KAM

values inside the grains. Considerable local misorientations may be observed only in the vicinity of some grain boundaries. These HAGBs are assumed to be incoherent or semi-coherent boundaries with significant lattice distortions. However, the majority of HAGBs are straight without considerable KAM values in the neighboring areas. These boundaries are assumed to be coherent HAGBs formed during recrystallization.

Fig. 3.17a reveals significant misorientations within the grains for the HPT-processed HMo-HPT alloy. High KAM values were also observed in the samples annealed up to the beginning (~630 K) and the end (~875 K) of the first large exothermic DSC peak, as shown in Figs. 3.17b and c, respectively.

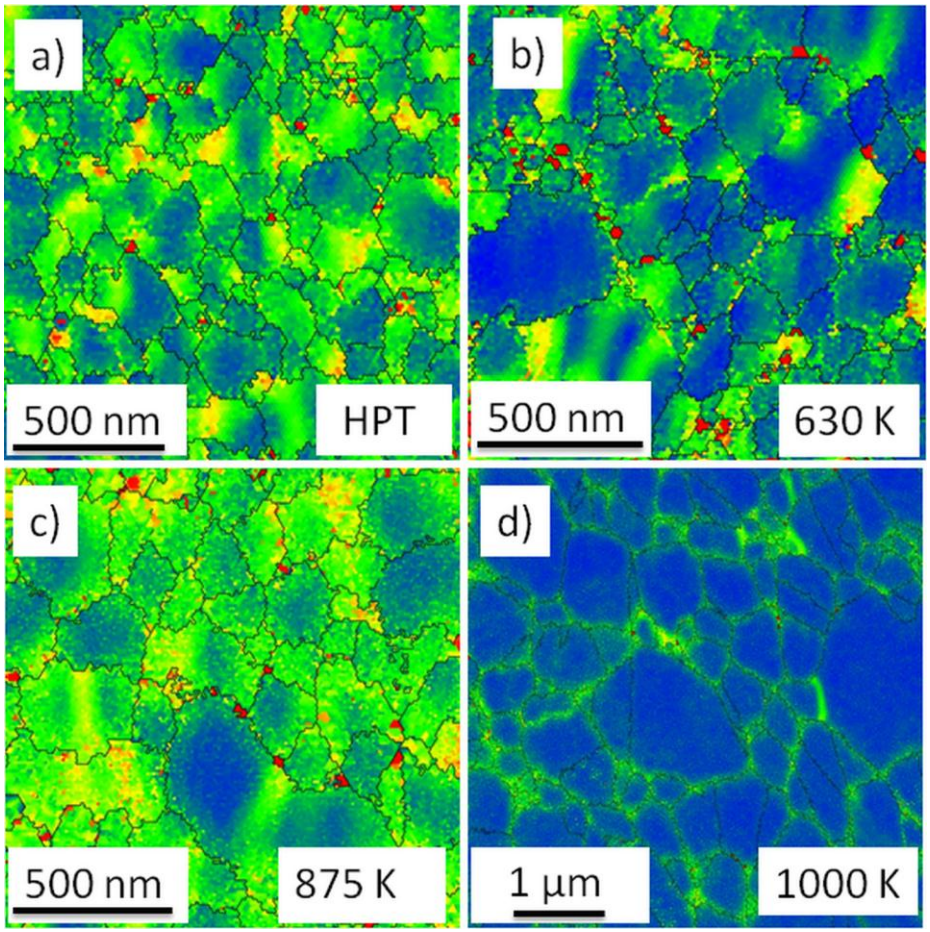

Fig. 3.17: KAM images showing the local misorientations between 0 and 5° for the HMo alloy after (a) HPT, (b) subsequent annealing at ~630 K, (c) ~875 K and (d) ~1000 K. The color code for the maps is shown in the inset in Fig. 3.16a. The HAGBs are indicated by black lines.

This observation suggests that considerable recrystallization does not occur in the HMo-HPT alloy between ~630 and ~875 K even if the average grain size increased from ~130 nm to ~225 nm. Therefore, the first large exothermic peak is related mainly to the recovery of the microstructure, which is accompanied by moderate grain growth. During the second large DSC peak the misorientations inside the grains were strongly reduced, and considerable KAM values are only observed in the vicinity of HAGBs. In addition, there are many grain boundaries which are straight and free of significant KAM values. It is assumed that these HAGBs are formed by recrystallization. The fraction of the distortion-free grain boundaries among HAGBs is lower for the HMo-HPT alloy than for the LMo-HPT sample (compare Figs. 3.16c and 3.17d) which suggests that recrystallization in the HMo-HPT material was not complete up to 1000 K. This observation is supported by the moderate grain growth to ~305 nm. Therefore, it is concluded that the increase of Mo content in Ni has a stronger retardation effect on the recrystallization than on the recovery. The latter process started at about 400 K for both alloys while the onset temperature of recrystallization was shifted from ~680 to ~875 K when the Mo concentration increased from ~0.28 to ~5.04 at.%. This difference is explained by the segregation of Mo atoms at HAGBs which hinders grain growth during recrystallization. The more pronounced separation of recovery and recrystallization for the HMo-HPT alloy led to two large DSC peaks between ~630 and ~1000 K (see Fig. 3.8). It should be noted that the separation of the recovery and recrystallization (or grain-growth) processes into two DSC peaks was also observed for severely deformed Al-based solid solutions either in powder or bulk form [110,111]. In addition, two exothermic peaks were detected for UFG Cu consolidated from a coarse-grained powder using the HPT technique [186]. In this case, contamination on the powder surface may be segregated at the grain boundaries in the sintered UFG sample which hinders grain boundary motion during recrystallization and grain growth.

3.3. Mechanical Properties

3.3.1 Effect of Mo Content on the Hardness of the SPD-Processed Ni Alloys

The measured hardness values of the cryorolled LMo and HMo alloys were ~2650 and ~3730 MPa, respectively. Fig. 3.18 shows the hardness for the center, half-radius and periphery positions of the HPT-processed disks with low and high Mo contents. It is apparent that the hardness increases with both distance from the disk center and the number of turns of HPT. After 5 turns the hardness saturated for both alloy compositions and became homogeneous along the disk radii. The saturation values of hardness for the LMo-HPT and HMo-HPT alloys were ~3200 and ~4300 MPa, respectively. This higher hardness for the larger Mo concentration is attributed to the higher dislocation density as discussed in more detail in the following section.

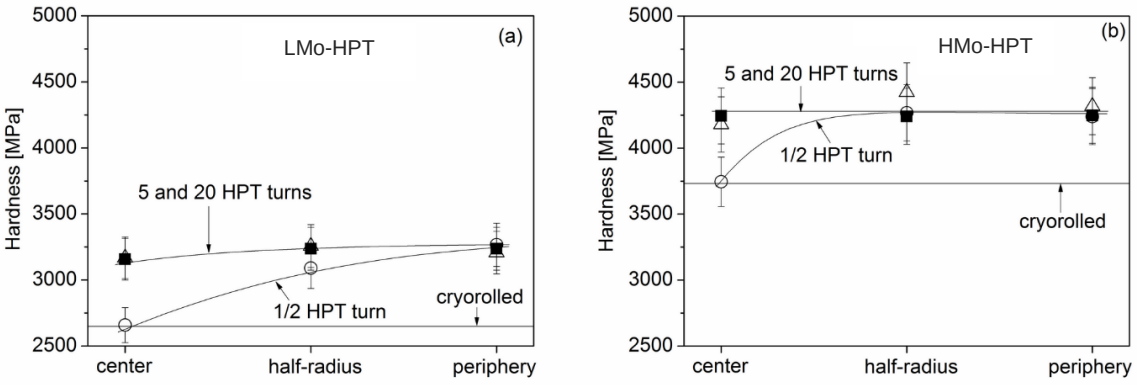

Fig. 3.18: The hardness in the center, half-radius and periphery for the LMo-HPT (a) and HMo-HPT (b) disks processed by different turns of HPT. The scales of the vertical axes in the two images are the same for an easier comparison of the very different hardness values in the LMo-HPT and HMo-HPT alloys. The hardness values for the cryorolled LMo and HMo alloys are also indicated by the horizontal lines.

3.3.2 Correlation Between the Yield Strength and the Dislocation Density

In the present study, cryorolling at LNT and HPT at RT were applied consecutively in order to refine the microstructure of two Ni alloys containing ~0.3 and ~5% Mo. The dislocation density after cryorolling was about one-half of the saturation value achieved by additional HPT, as

shown in Fig. 3.7. At the same time, the grain sizes of the cryorolled samples were at least one order of magnitude larger than the values determined after HPT. These observations demonstrate that for both compositions the increase of the dislocation density was faster than the refinement of the grain structure. Accordingly, the cryorolled samples had high dislocation density (15-35 × 10^{14} m^{-2}) while the grain size remained relatively large (~4 μm). Despite this large grain size, the cryorolled alloys exhibited high hardness (~2650 and ~3730 MPa for LMo and HMo samples, respectively) due to the high dislocation density.

The rate of microstructure evolution during HPT is similar for both the 0.3 and 5% Mo alloys. At the half-radius and the periphery of the disk, the grain size, the HAGB fraction and the dislocation density achieve saturation values even after only ½ turn. In addition, in the disk center, the grain size and the HAGB fraction saturate only after 20 turns due to the much lower shear strain per turn. The dislocation density in the disk center reached a maximum value earlier after only 5 turns.

The results show that the Mo concentration has a significant effect on the saturation values of the microstructural parameters. For 5% Mo, the grain size is about 30% smaller, and the dislocation density is two times larger than for the 0.3% Mo alloy. This is due to the pinning effect of Mo on dislocations and grain boundaries which in practice hinders the occurrence of dynamic microstructural recovery during SPD. In addition, this effect also hinders the arrangement of dislocations into low energy configurations, such as dipoles, within the refined grains. As a consequence of this effect, the dislocation arrangement parameter, *M*, is much higher for the alloy containing the larger amount of Mo. At the same time, there was no major difference between the saturation values of the HAGB fractions for the LMo-HPT and HMo-HPT samples, as their values were between 70 and 75%. This is similar to the HAGB fractions reported for Ni processed by HPT or a combination of ECAP and HPT [112]. Therefore, it appears that the higher Mo content has no significant effect on the saturation values of the

HAGB and LAGB fractions. It should be noted, however, that EBSD investigations take into account only those LAGBs which have misorientations between 2 and 15° and thus the LAGB fractions for misorientations lower than 2° may be different in these two alloys in accordance with the different values for the dislocation arrangement parameter *M*.

HPT processing of the cryorolled alloys led to significant hardening. The maximum hardness values achieved by a combination of cryorolling and HPT were ~3200 and ~4300 MPa for LMo-HPT and HMo-HPT alloys, respectively. In order to study the strengthening mechanisms in the HPT-processed Ni alloys, the yield strength, σ_Y, was estimated as one-third of the hardness and compared with the stress, σ_{Taylor}, calculated from the dislocation density, ρ, using the Taylor equation:

$$\sigma_{Taylor} = \sigma_0 + \alpha M^T G b \rho^{1/2} \quad (3.2)$$

where σ_o is threshold stress, α is a constant describing the dislocation strengthening, G is the shear modulus (~82 GPa for Ni), b is the magnitude of the Burgers vector (~0.25 nm for Ni) and M^T is the Taylor factor. The alloys used in this investigation did not exhibit a strong texture and therefore M^T was taken as 3.06. The values of σ_o for the LMo-HPT and HMo-HPT alloys were determined by uniaxial compression of samples annealed in a vacuum furnace at 800°C for 24 h and then quenched in oil to RT in order to retain the supersaturated solid solution state. The threshold stress values were obtained as ~40 and ~180 MPa for the LMo-HPT and HMo-HPT alloys, respectively.

In eq. (3.2), σ_o includes the solid solution strengthening caused by the alloying elements in the Ni alloys and therefore the value of σ_o is much higher for the HMo-HPT alloy than for the LMo-HPT material. In previous studies, eq. (3.2) was successfully applied for a calculation of the yield strength from the dislocation density for many SPD-processed metals and alloys without an additive Hall-Petch term [187]. In the present investigation, the dislocation density was

determined by XLPA, which measures both the statistically stored and the grain boundary dislocations. In SPD-processed microstructures, many dislocations are accumulated at the HAGBs through pile ups, and therefore gliding dislocations interact with these dislocations rather than directly with the grain boundaries. As a consequence, HAGB hardening is practically included in eq. (3.2) and α may be regarded as an effective dislocation strengthening parameter.

For the present Ni alloys, the values of the parameter α in eq. (3.2) are not known initially, since they are strongly influenced by the arrangements of the dislocations. Usually, the value of α varies between 0.1 and 0.4 [188], and a less clustered dislocation structure is associated with a lower value of α [189]. Therefore, the parameter α in plastically deformed metals may depend on the types and concentrations of alloying elements, the SFE and the applied strain. For example, it was shown that a lower SFE yields a smaller α since the clustering of highly dissociated dislocations is retarded by their difficult cross slip and climb [188]. For the present LMo-HPT and HMo-HPT alloys processed by cryorolling and HPT, the value of α was determined by minimizing the difference between the yield strength determined experimentally as one-third of the hardness (σ_Y) and the strength values (σ_{Taylor}) calculated from Eq. (3.2). The significant difference between the dislocation arrangement parameters for the two alloys, as discussed in section 3.1.3, suggests that the value of α may also differ for the LMo-HPT and HMo-HPT materials. Thus, when the difference between the calculated and measured strength values is minimized by a least squares method, the values of α for the LMo-HPT and HMo-HPT alloys were refined independently. This fitting procedure yielded 0.32 ± 0.03 and 0.26 ± 0.02 for parameter α for the LMo-HPT and HMo-HPT alloys, respectively, where these values are similar to α obtained previously for Ni processed by 6 passes of ECAP at RT (~0.26) [37]. The slightly lower value of α for the HMo-HPT alloy is attributed to the less clustered

dislocation structure after HPT in accordance with the higher dislocation arrangement parameter.

Fig. 3.19 plots the experimentally determined yield strength against the strength calculated from eq. (3.2) for the cryorolled and the HPT-processed Ni alloys using the refined values of α of 0.32 and 0.26 for the LMo-HPT and HMo-HPT alloys, respectively. Inspection of Fig. 3.19 shows that the measured and the calculated strength values agree within the experimental error.

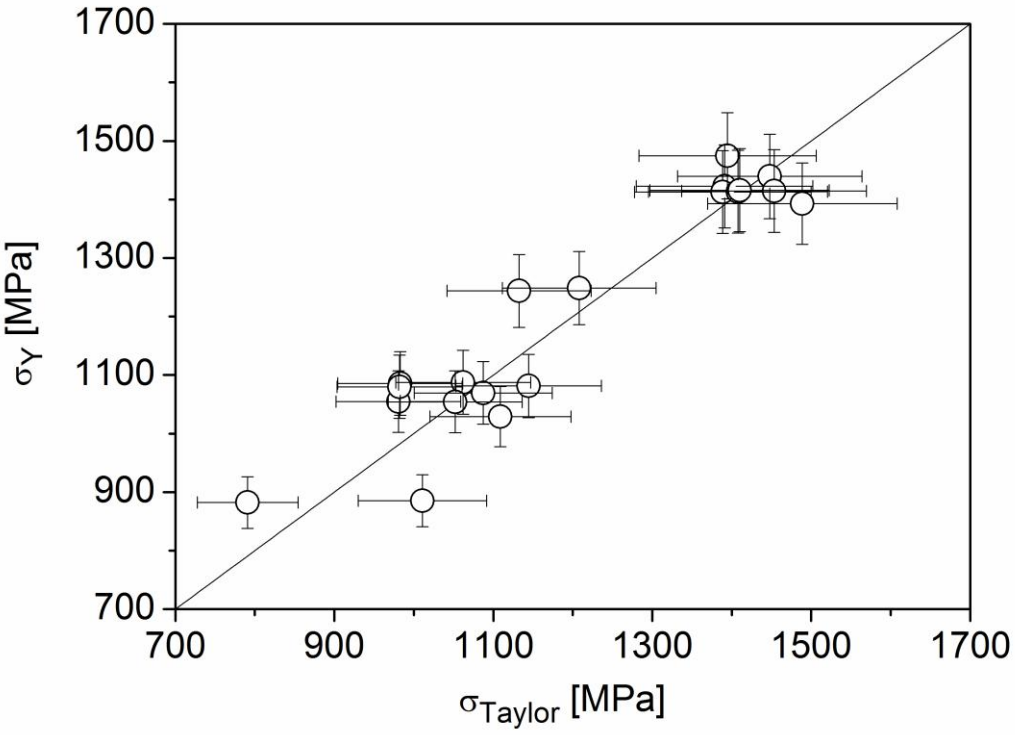

Fig. 3.19: The experimentally determined yield strength (σ_Y) versus the strength calculated from the Taylor equation (σ_{Taylor}) for the cryorolled Low-Mo and High-Mo alloys, and the HPT processed disks at the center, half-radius and periphery for ½, 5 and 20 turns. The Taylor strength was calculated using 0.32 and 0.26 as α for the Low-Mo and High-Mo alloys, respectively.

It is noted that the parameter α may vary both with increasing distance from the center of the HPT disk and with the number of turns. Therefore, the values of α were also calculated from eq. (3.2) for each position in the HPT disks using the condition $\sigma_Y = \sigma_{Taylor}$. No significant dependence was observed for α in terms of the distance from the disk center or the numbers of

turns. This demonstrates that the use of a single α value for every strength value obtained for the same Mo content is a good approximation in determining α.

3.3.3 Annealing-induced Hardening in Ultrafine-grained Ni-Mo Alloys

The tensile performance of the samples processed by 20 turns of HPT and the specimens processed through 20 turns of HPT and then annealed to the beginning and the end of the large exothermic DSC signal was studied on miniature samples. The preparation details of these specimens are given in section 2.2.6.2. The engineering stress-strain curves for the LMo-HPT and HMo-HPT alloys are shown in Fig. 3.20a and b, respectively.

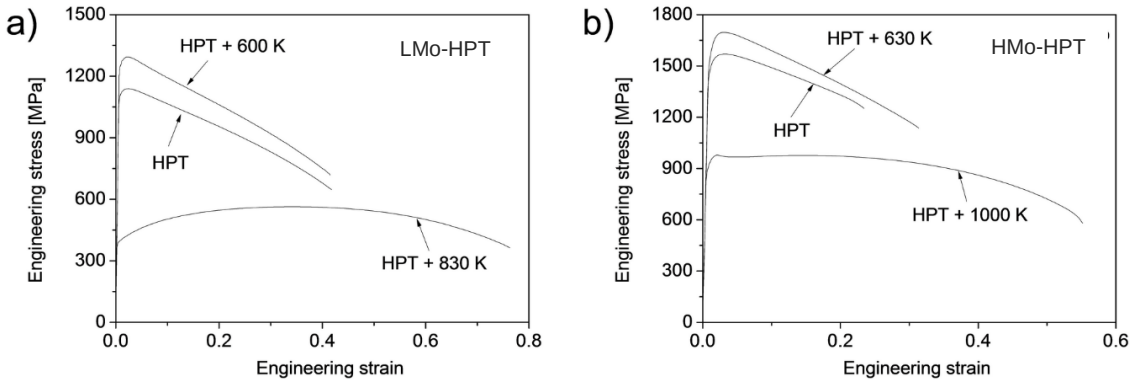

Fig. 3.20: Engineering stress-strain curves obtained by tension for the HPT-processed and annealed states of (a) the LMo-HPT and (b) HMo-HPT alloys.

The yield strength, the ultimate tensile strength, the uniform elongation, and the elongation to failure were determined from the tensile curves and plotted for the LMo-HPT and HMo-HPT alloys in Fig. 3.21a and b, respectively. These values were obtained as the average of the values measured for the two samples fabricated from one disk. The errors in the datum points were calculated as the difference between the average and the individual values obtained for the two tensile specimens. For some points, the error is smaller than the symbol size, therefore, in this case, the uncertainty of the value is represented by the dimension of the symbol. The yield and ultimate tensile strength values for the HPT-processed LMo-HPT sample were ~970 and ~1140

MPa, respectively (see Fig. 3.21a). The higher Mo concentration increased both the yield and ultimate tensile strength to ~1370 and ~1570 MPa, respectively, which can be explained by the higher solute content, the smaller grain size and the higher dislocation density (see Fig. 3.22).

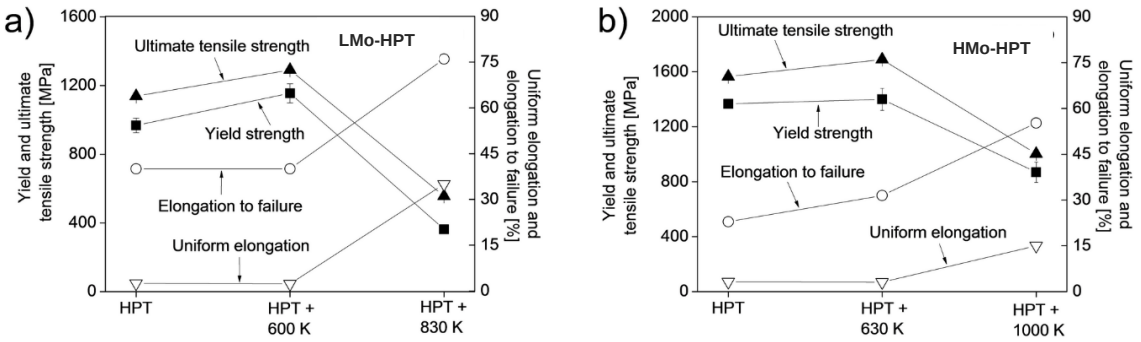

Fig. 3.21: The yield strength, the ultimate tensile strength, the uniform elongation and the elongation to failure determined for the HPT-processed and annealed states of (a) the LMo-HPT and (b) HMo-HPT alloys.

Annealing of the LMo-HPT alloy to ~600 K increased the yield strength and the ultimate tensile strength by 19 and 13%, respectively (see Fig. 3.21a). This heat-treatment yielded no change in the ductility as the uniform elongation, and the elongation to failure remained ~3 and ~40%, respectively. It should be noted that the present experiments were carried out on miniature tensile specimens for which both the ratio of gauge length to width and the sample thickness are smaller than for a standard tensile specimen. A former study showed that the measured elongation to failure usually increases with decreasing ratio of gauge length to width and increasing specimen thickness [83]. Therefore, the two effects nearly compensate each other by comparing the data obtained on these miniature specimens with a standard sample having dimensions of $5 \times 1 \times 1$ mm^3. In addition, the present study focuses on the increase of strength due to annealing and not on the change of ductility.

For an explanation of the annealing-induced hardening in the LMo-HPT sample, the microstructures in the HPT-processed and annealed specimens are compared (see Fig. 3.22a). During annealing to ~600 K, the dislocation density decreased from ~$27 \pm 3 \times 10^{14}$ m^{-2} to ~17

$\pm$ 2 × 10^{14} m^{-2} while the grain size remained unchanged (~180 nm) which suggests that only recovery occurred. During this recovery, the dislocation arrangement parameter decreased significantly, indicating a more clustered dislocation configuration after annealing. The more clustered dislocation arrangement within the grains has a higher strengthening effect (manifested in a higher value of α in the Taylor equation), resulting in a hardening, despite the decrease of the dislocation density [189]. The arrangement of dislocations into low energy configurations (e.g., into subgrain boundaries) is also confirmed by the increase of the LAGB fraction determined by EBSD (see Fig. 3.22a). The higher strengthening effect of this more clustered dislocation arrangement may cause the hardening observed after annealing to ~600 K, despite the significant reduction in the dislocation density. In addition to this effect, the annihilation of mobile dislocations may also contribute to the hardening observed after annealing since the reduced mobile dislocation density makes plastic deformation more difficult as discussed elsewhere [168]. Moreover, former molecular dynamic simulations showed that the relaxation of non-equilibrium grain boundaries during annealing can lead to a hindered emission of dislocations from grain boundaries, which also induces hardening [166].

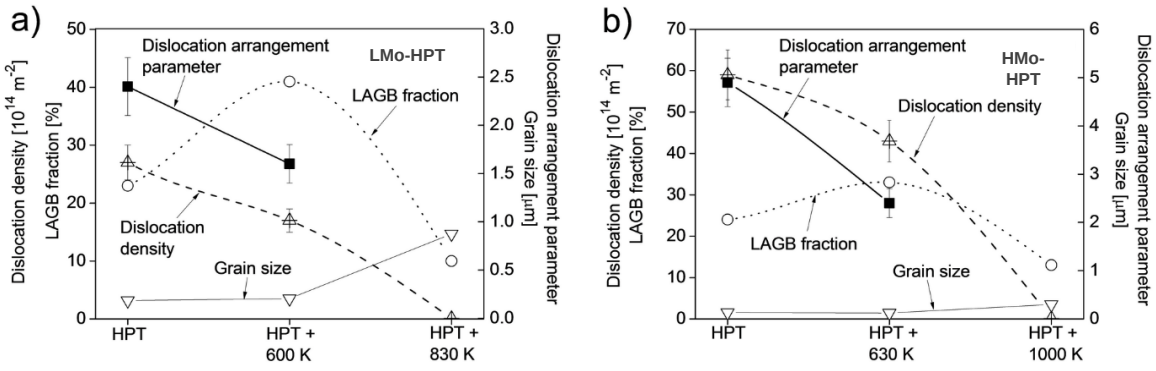

Fig. 3.20: The grain size, the dislocation density, the dislocation arrangement parameter and the LAGB fraction determined for the HPT-processed and annealed states of (a) the LMo-HPT and (b) HMo-HPT alloys.

For the HMo-HPT alloy, annealing to ~630 K resulted in a much lower hardening than for the LMo-HPT alloy (see Fig. 3.21). During this heat treatment, the dislocation density and the

dislocation arrangement parameter decreased while the grain size remained unchanged (~130 nm), similar to the behavior of the LMo-HPT alloy. In addition, the fraction of LAGBs in the HMo-HPT alloy also increased during annealing to ~630 K. The lower annealing-induced hardening in the HMo-HPT sample can be explained by the hindering effect of the higher Mo content on the annihilation of mobile dislocations and the clustering of the remaining dislocations. The change of ductility in this specimen was also marginal and similar to the LMo-HPT alloy.

An annealing-induced strengthening has already been observed for other UFG or nanocrystalline materials [166,167,169–171]. It was shown for electrodeposited nanocrystalline Ni films that the segregation of impurities and alloying elements to the grain boundaries during annealing may lead to a more difficult occurrence of grain boundary mediated deformation mechanisms, such as grain boundary sliding and grain rotation, resulting in hardening [167,169]. As a consequence, the larger alloying element concentration in Ni will yield a higher annealing-induced strengthening effect as was demonstrated for electrodeposited Ni-Mo alloys with grain sizes between ~3 and ~25 nm [171]. With increasing Mo content from 0.8 to 21.5 at.%, the grain size decreased from ~25 to ~3 nm, and the hardness increment induced by annealing increased from ~20 to ~125%. At the same time, for the present HPT-processed Ni-Mo alloys the annealing-induced strengthening decreased with increasing Mo content: the increase of the yield strength in the LMo-HPT and the HMo-HPT alloys are ~19% and ~2.4% during annealing to 600 and 630 K, respectively (see Fig. 3.21). The opposite trend can be explained by the much larger grain size for the HPT-processed Ni-Mo alloys (~130-180 nm), resulting in a less significant role of grain boundary sliding in plasticity. Rather, for the UFG Ni-Mo alloys the change of the dislocation strengthening during the heat-treatments plays a crucial role in the annealing-induced hardening effect. In the HMo-HPT alloy, the higher solute Mo content hinders the annihilation of mobile dislocations and the arrangement of the

remaining dislocations into low energy configurations during the heat-treatment to ~630 K. Therefore, the annealing-induced hardening is less pronounced for the HMo-HPT with smaller grain size than for the LMo-HPT alloy.

For the LMo-HPT sample, between 600 and 830 K, the strength values decreased due to the increase of the grain size to ~870 nm and the reduction of the dislocation density below ~10^{13} m^{-2}. In addition, the ductility was significantly improved. The strength reduction and the ductility increase for the HMo-HPT alloy annealed to the end of the exothermic signal (~1000 K) were lower than for the LMo-HPT sample, despite the larger temperature for the former alloy. This is due to the much better stability of the HMo-HPT alloy (the gran size increased only to ~300 nm at ~1000 K). It is noted that both alloys remained solid solutions during annealing as proven by X-ray diffraction experiments, therefore there was no influence from precipitation on the mechanical properties.

Chapter 4: The Nanostructure and its Thermal Stability in Electrodeposited Ni-Mo Alloys

This chapter deals with the thin films of Ni alloys with low and high Mo concentrations, which were processed by electrodeposition with and without saccharin addition. The evolution of microstructure, including grain size and dislocation density, with increasing Mo and saccharin contents is discussed. Moreover, to understand the annealing-induced changes in the microstructure, these layers were annealed to different temperatures up to 1000 K. The evolution of microstructure, defect structure, thermal stability, and hardness during annealing of electrodeposited Ni-Mo films is shown. The stored energy in nanocrystalline Ni-Mo thin films processed by electrodeposition was determined experimentally by DSC and compared with the values calculated from the parameters of the microstructure.

4.1. Microstructure and defect densities in the as-deposited layers

The Mo contents in the layers with low and high Mo contents were 0.4 and 5.3 at.%, respectively. These values were intentionally selected as the present electrodeposited films will be compared with bulk UFG Ni-Mo alloys having similar compositions but processed by HPT [190]. Hereafter, the materials with low and high Mo concentrations are designated as LMo-ED and HMo, respectively. In addition to the effect of Mo concentration, the influence of the saccharin on the microstructure, and its thermal stability of samples LMo-ED and HMo-ED was also investigated. Therefore, additional samples were processed by adding 1 g/l saccharin to the bath. These samples are denoted as LMo-sac-ED and HMo-sac-ED. In these specimens, EDS revealed the same Mo contents as for the saccharin-free layers, but in addition sulfur was also detected with the concentration of 0.2 at.%.

For all compositions, the deposits were free of cracks even at the relatively large deposit thickness needed for the study of high-temperature structural relaxation. As an example, the SEM images in Fig. 4.1 show the crack-free surfaces of samples LMo-sac-ED and HMo-sac-ED.

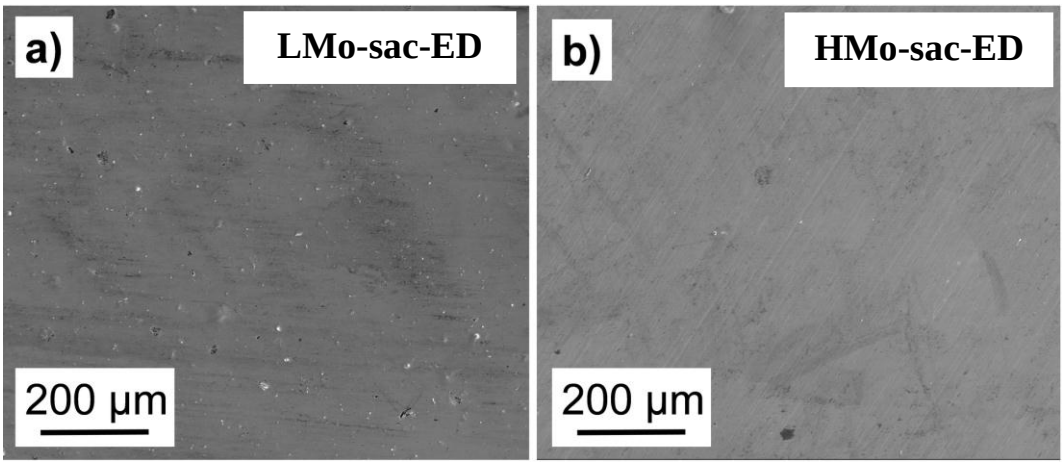

Fig. 4.1: SEM images showing the crack-free surfaces of samples (a) LMo-sac-ED and (b) HMo-sac-ED.

The microstructure of the initial layers is illustrated in Fig. 4.2, which shows dark-field TEM images for the as-processed LMo-ED, HMo-ED, LMo-sac-ED and HMo-sac-ED samples. The grain size values obtained from the TEM images are listed in Table 4.1.1. It can be seen that the increase of the Mo content from ~0.4 to ~5.3 at.% in the Ni layer is accompanied by one order of magnitude reduction in the grain size from ~240 nm to ~26 nm. Similar decrease in the grain size was observed when saccharin was added to sample LMo-ED. At the same time, addition of saccharin to HMo-ED did not yield a considerable change of the grain size determined by TEM.

Table 4.1: The diffraction domain size ($<x>_{area}$), the dislocation density (ρ) and the twin-fault probability (β) determined by XLPA as well as the grain size (d_{TEM}) obtained from TEM for the as-processed layers.

Sample	d_{TEM} [nm]	$<x>_{area}$ [nm]	ρ [10^{14} m^{-2}]	β [%]
LMo-ED	240	40 ± 4	23 ± 3	< 0.1
HMo-ED	26	47 ± 5	114 ± 12	3.9 ± 0.4
LMo-sac-ED	31	20 ± 5	105 ± 11	1.8 ± 0.2
HMo-sac-ED	21	30 ± 5	283 ± 30	5.8 ± 0.6

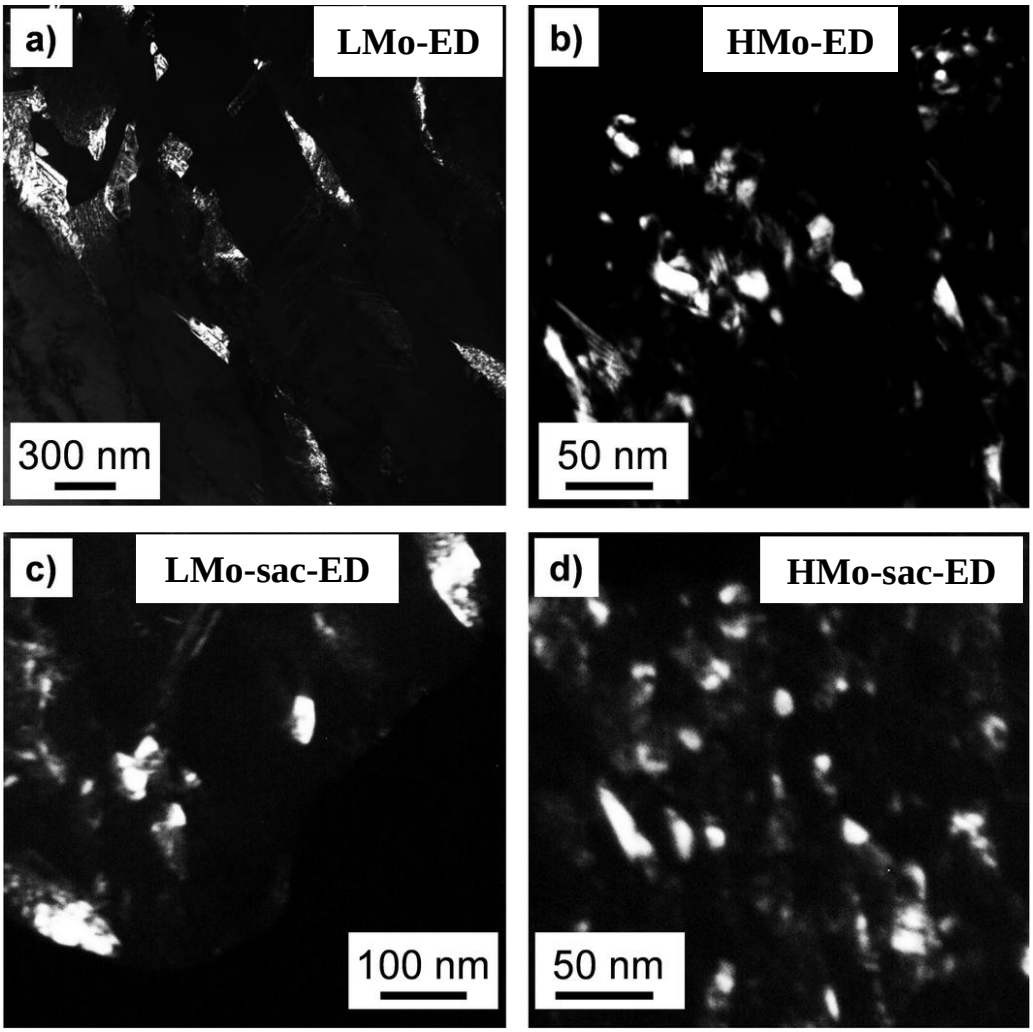

Fig. 4.2: Dark-field TEM images for (a) LMo-ED, (b) HMo-EDo, (c) LMo-sac-ED and (d) HMo-sac-ED samples.

The average diffraction domain size, the dislocation density, and the twin fault probability were determined by XLPA. As an example, Fig. 4.3 illustrates the CMWP fitting on the diffraction pattern measured for sample HMo-ED. The microstructural parameters obtained by XLPA for the as-processed LMo-ED, HMo-ED, LMo-sac-ED and HMo-sac-ED samples are listed in Table 4.1.1. The diffraction domain size for specimen LMo-ED is much smaller (~40 nm) than the grain size determined by TEM (~240 nm). This difference suggests a subgrain structure in the layer LMo-ED. In the determination of the grain size from TEM, we used dark-field images which guarantee that the volumes bounded by high-angle grain boundaries were considered as grains. At the same time, XLPA is very sensitive to small misorientations, therefore the diffraction domain size for materials with high defect (e.g., dislocations) densities corresponds to the subgrain or dislocation cell size [173]. For the other three samples, the grain and diffraction domain sizes differ from each other by a factor of less than two. Moreover, for specimens HMo-ED and HMo-sac-ED the diffraction domain size is larger than the grain size. These relatively small differences can be attributed to the different sampling statistics of XLPA and TEM methods. As the volume studied by XLPA was about seven orders of magnitude larger than that investigated by TEM, the statistics of XLPA results are much better, and the small deviations from the TEM results are not surprising.

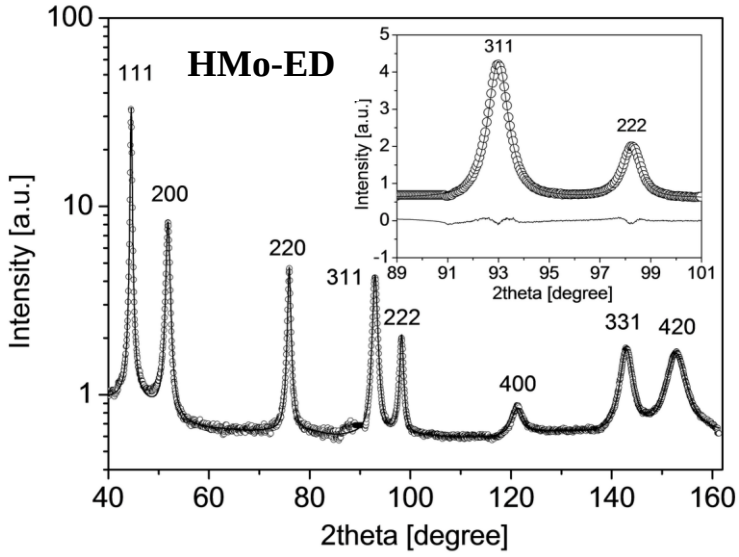

Fig. 4.3: CMWP fitting of the X-ray diffraction pattern taken for sample HMo-ED. The open circles and the solid line represent the measured data and the fitted curve, respectively. The intensity is in logarithmic scale. The inset shows a magnified part of the diffractogram in linear intensity scale where the difference between the measured and the fitted patterns is also given at the bottom of the figure.

The dislocation density in the sample LMo-ED was ~23 × 10^{14} m^{-2} as obtained by XLPA (see Table 4.1.1). The addition of both Mo and saccharin increased the dislocation density significantly to about 110 × 10^{14} m^{-2}. The high Mo content together with saccharin addition resulted in the highest dislocation density with the value of ~283 × 10^{14} m^{-2}. In sample LMo-ED, the twin fault probability was under the detection limit of XLPA. At the same time, the increase of the Mo concentration and the addition of saccharin yielded a significant twin fault probability in the Ni layer with the values between ~1.8 and ~3.9%. When both high Mo compound and saccharin were added to the bath during the Ni film deposition (sample HMo-sac-ED), the twin fault probability reached its highest value of 5.8%. The high twin fault density is confirmed by the TEM image in Fig. 4.4 where the twin boundaries are indicated by white arrows. Thus, it can be concluded that the defect density increased when either Mo or saccharin was added to the Ni layer, and the highest defect density was achieved by the combination of the two additives.

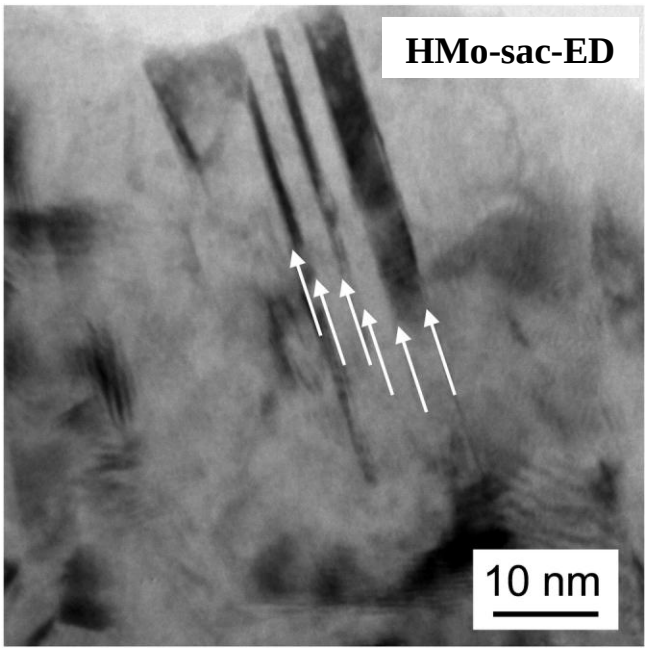

Fig. 4.4: Bright-field TEM image showing twin faults in sample HMo-sac-ED.

4.2. DSC annealing of the electrodeposited films

All the four studied samples were subjected to DSC scan up to the temperature of 1000 K. For specimens LMo-ED and HMo-ED, neither exothermic nor endothermic signal was detected between 300 and 1000 K. At the same time, an exothermic peak was observed for the samples with saccharin addition. Fig. 4.5 shows the DSC thermograms after baseline subtraction for samples LMo-sac-ED and HMo-sac-ED. For specimen LMo-sac-ED, the exothermic peak was developed between 650 and 720 K with the heat released of 5.6 J/g. For sample HMo-sac-ED, the exothermic peak was detected between 735 and 813 K and the released heat was 14.3 J/g. Thus, it can be concluded that the temperature range of the exothermic peak was shifted to higher values while the released heat increased with increasing Mo concentration in the sulfur-containing specimens. The exothermic DSC peaks for nanocrystalline materials are usually related to the recovery and recrystallization of the microstructure. The lack of detectable exothermic signal for samples LMo-ED and HMo-ED does not mean the absence of recovery

and recrystallization, but it may be due to the very broad temperature range of the heat released during these processes.

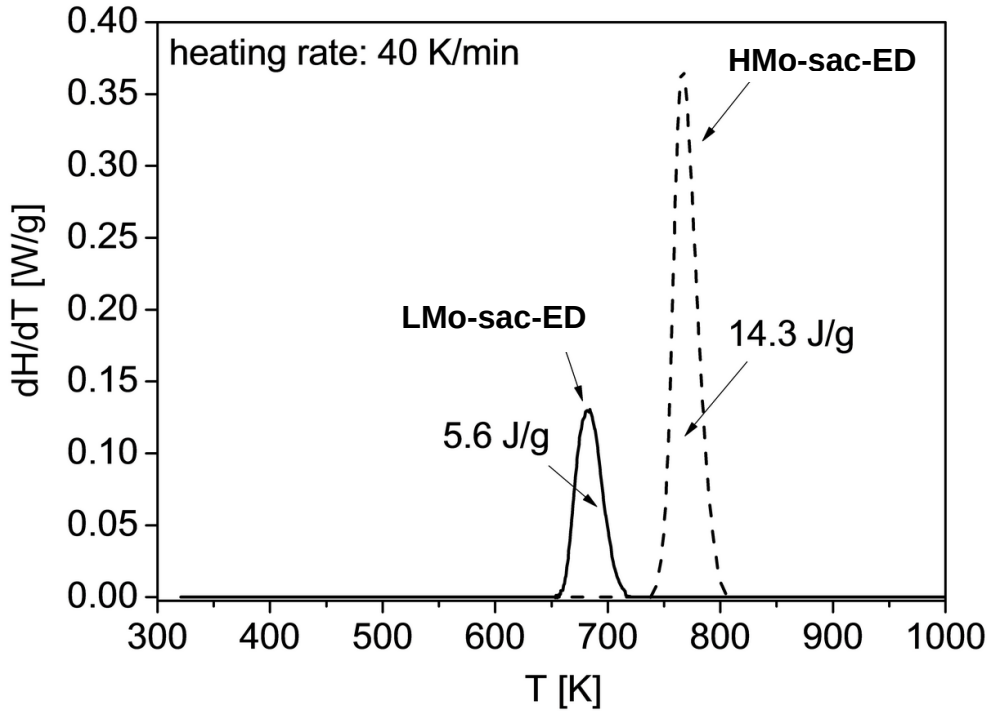

Fig. 4.5: DSC thermograms after baseline subtraction for samples LMo-sac-ED and HMo-sac-ED measured at a heating rate of 40 K/min.

4.2.1 Microstructure evolution during annealing

For the study of the effects of Mo and saccharin on the thermal stability of the electrodeposited Ni layers, samples were heated up to the characteristic temperatures of the DSC thermograms, i.e., to the beginning and the end of the exothermic peaks, and then quenched to RT. For specimens LMo-ED and HMo-ED, DSC peaks were not observed, therefore they were annealed to the same temperatures as for the counterparts containing sulfur. This means that samples LMo-ED and LMo-sac were heated up to 650 and 720 K while layers HMo-ED and HMo-sac-ED were annealed to 735 and 813 K. It will be shown that samples LMo-ED and HMo-ED exhibit a better stability than the layers processed with saccharin, therefore the saccharin-free

specimens were also heated up to the maximum temperature of the DSC thermograms (1000 K). The annealing temperatures for the four layers are summarized in Fig. 4.6.

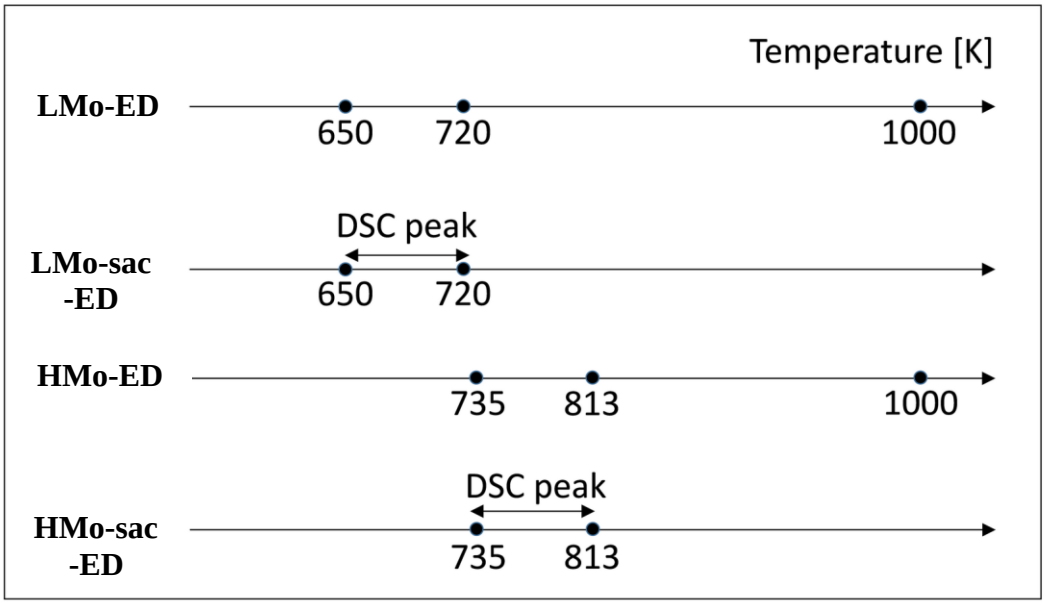

Fig. 4.6: A schematic showing the temperatures of annealing for samples LMo-ED, HMo-ED, LMo-sac-ED and HMo-sac-ED.

The evolution of the dislocation density, the twin fault probability and the diffraction domain size determined by XLPA as a function of the annealing temperature is shown in Fig. 4.7. For both samples LMo-sac-ED and HMo-sac-ED, the dislocation density and the twin fault probability decreased moderately up to the beginning of the exothermic peak, i.e., recovery occurred in these layers even if the exothermic signal was not observed. This apparent contradiction can be explained by the distribution of the released heat over a wide temperature range that makes the exothermic signal undetectable. The decrease of the dislocation density and twin fault probability in samples LMo-sac-ED and HMo-sac-ED was accelerated in the temperature ranges corresponding to the DSC peaks (see Fig. 4.7a and b).

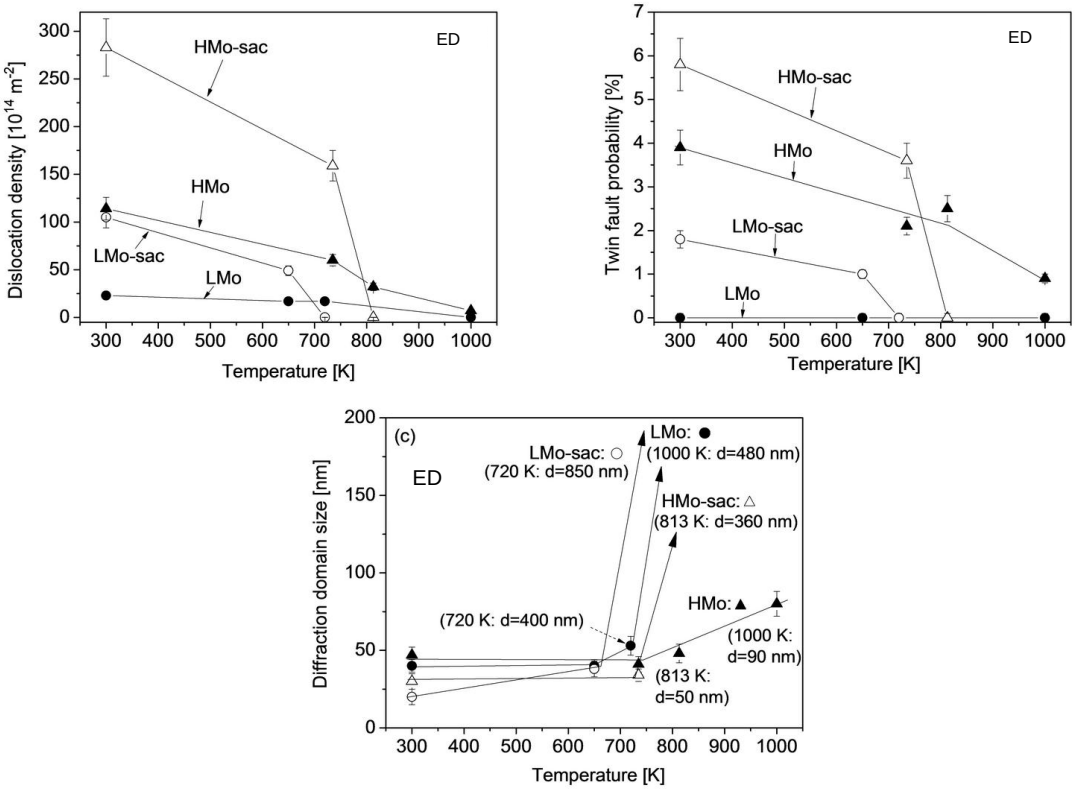

Fig. 4.7: Evolution of the (a) dislocation density, (b) twin fault probability and (c) diffraction domain size as a function of annealing temperature for electrodeposited samples LMo-ED, HMo-ED, LMo-sac-ED and HMo-sac-ED. The grain sizes (denoted by d) determined by EBSD are also given for some selected samples in (c). In this figure, the arrows indicate that the diffraction domain size increased above the detection limit of XLPA.

For these layers, at the end of the exothermic peaks, the Debye-Scherrer X-ray diffraction rings became spotty, and the breadth of these spots was practically the same as the instrumental broadening. This means that the volumes reflecting these intensity spots were recovered and/or recrystallized and the dislocation density and the twin fault probability in these grains were under the detection limits of XLPA (~10^{13} m^{-2} and ~0.1%, respectively). Similar evolution was observed for the diffraction domain size, i.e., its increment was accelerated in the temperature range corresponding to the exothermic signal, and at the end of the DSC peak its value in the volumes reflecting the high intensity spots in the Debye-Scherrer rings was above the detection limit of XLPA (~800 nm). It should be noted that the narrow spots were superimposed on a

broader continuous ring for each reflection, therefore the average domain size may be smaller than ~800 nm. Anyway, the large number of high intensity spots in the Debye-Scherrer rings suggests that the majority of the microstructures in samples LMo-sac-ED and HMo-sac-ED was recovered and/or recrystallized at the temperatures corresponding to the end of the DSC peaks. It should be noted that for layer LMo-sac-ED, the defect structure became very inhomogeneous due to recovery after annealing to the beginning of the exothermic peak (650 K). This was apparent from the shape of the XRD peaks. As an example, Fig. 4.8 shows reflection 200 for sample LMo-sac-ED annealed to 650 K. This special peak shape can be obtained by the sum of a narrower and a broader component. The former and the latter sub-reflections correspond to strongly and weakly recovered volumes in the studied material. Indeed, in the CMWP fitting the narrower diffraction peak components yielded the following microstructural parameters: $\langle x \rangle_{area} = 147 \pm 16$ nm, $\rho = (8 \pm 1) \times 10^{14}$ m^{-2} and $\beta = 0\%$. At the same time, the broader profile components gave $\langle x \rangle_{area} = 24 \pm 3$ nm, $\rho = (54 \pm 5) \times 10^{14}$ m^{-2} and $\beta = 1.0 \pm 0.1\%$. For all XRD reflections, the fractions of the narrow and broad peak components were 0.11 and 0.89, respectively, indicating that only a minor part of the sample LMo-sac-ED suffered strong recovery during heating up to the beginning of the exothermic DSC peak. The values of the

defect densities and diffraction domain size plotted in Fig. 4.7 were obtained as a weighted average of the parameters determined for the two microstructure components.

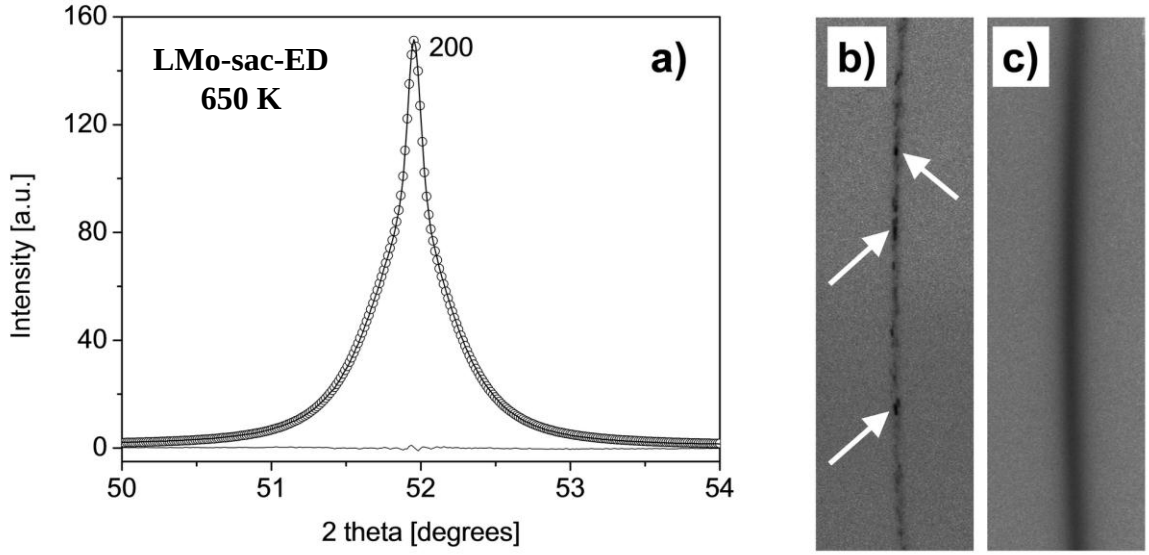

Fig. 4.8: (a) X-ray diffraction peak with the indices 200 for sample LMo-sac-ED heated up to 650 K. The open circles and the solid line represent the measured data and the fitted curve, respectively. The difference between the measured and the fitted peaks is also given at the bottom of the figure. (b) and (c) show Debye-Scherrer diffraction rings of reflection 222 for samples LMo-ED and HMo-ED, respectively, heated up to 1000 K. The white arrows indicate spots in the ring of sample LMo-ED.

Fig. 4.7 reveals that in the temperature range corresponding to the DSC peaks of the samples deposited from solutions with saccharin, the defect densities, and the crystallite size in the saccharin-free samples only slightly changed. Thus, it is apparent that the presence of sulfur as a result of the saccharin addition significantly reduced the thermal stability of the Ni layers for both low and high Mo contents. Comparing the LMo-ED and HMo-ED samples, the higher Mo content improved the stability as after heating up to 1000 K the layer LMo-ED was recrystallized while in the sample HMo-ED only recovery occurred. This difference can also be seen from the Debye-Scherrer rings. Fig. 4.8b and c compares the Debye-Scherrer diffraction rings of reflection 222 for samples LMo-ED and HMo-ED heated up to 1000 K. For specimen

LMo-ED, the ring is spotty, indicating recrystallization, while the ring of layer HMo-ED is broad and homogeneous, suggesting the lack of recrystallization. The evaluation of the pattern measured for specimen HMo-ED annealed to 1000 K showed that the dislocation density and the twin fault probability remained as high as ~7 × 10^{14} m^{-2} and ~0.9 %, respectively, and the diffraction domain size increased only to ~80 nm. These values prove the very good thermal stability of the layer processed with high Mo content but without saccharin.

As XLPA method could not give quantitative information about the saccharin containing samples annealed to the end of the DSC peaks, EBSD was applied for the characterization of the recovered/recrystallized microstructures in samples LMo-sac-ED and HMo-sac-ED as shown in Figs. 4.9a and b, respectively. The average grain sizes determined for the layers LMo-sac-ED and HMo-sac-ED annealed to 720 and 813 K, respectively, were ~850 and ~360 nm.

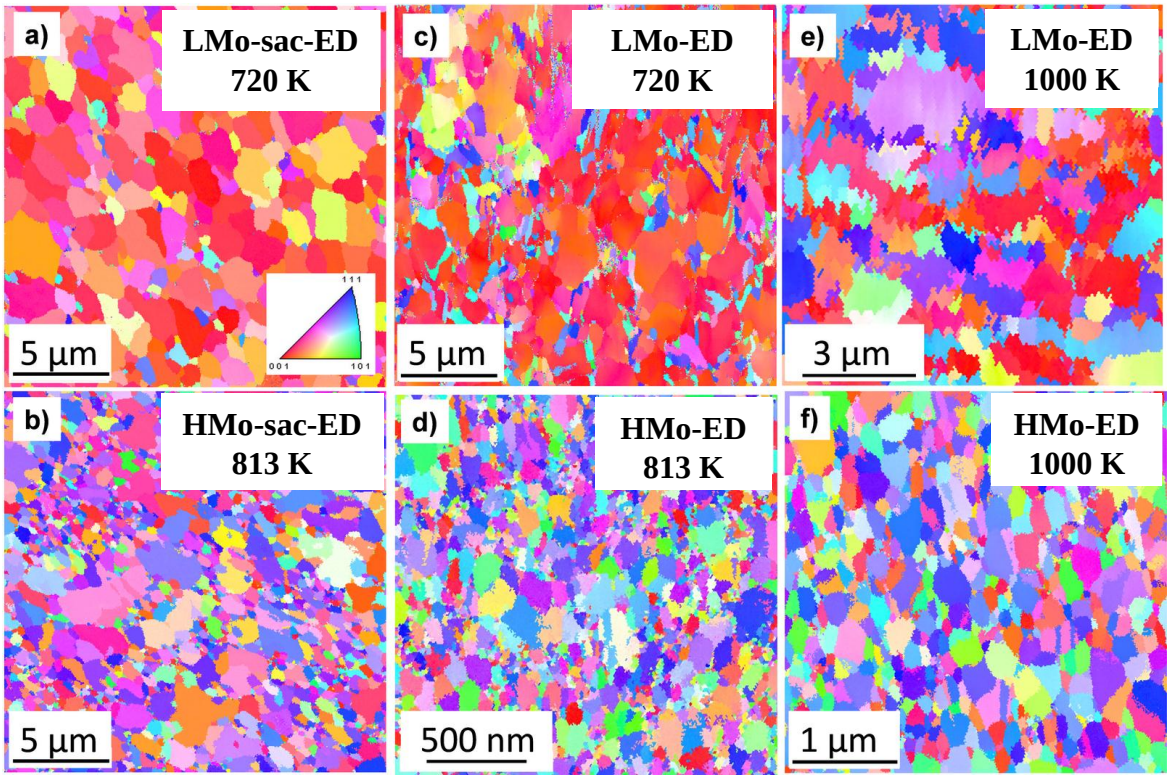

Fig. 4.9: EBSD orientation maps for samples (a) LMo-sac heated up to 720 K, (b) HMo-sac-ED heated up to 813 K, (c) LMo heated up to 720 K, (d) HMo heated up to 813 K, (e) LMo heated up to 1000 K and (f) HMo heated up to 1000 K.

These values are also shown in Fig. 4.7c at the arrows which indicate that the diffraction domain size could not be determined by XLPA. For comparison, Figs. 4.9c and d show EBSD images for the sulfur-free samples heated up to the same temperatures as the sulfur-containing counterparts. The average grain sizes for the layers LMo-ED and HMo-ED annealed to 720 and 813 K, respectively, were ~400 and ~50 nm. These values are much smaller than the grain sizes obtained for the specimens LMo-sac-ED and HMo-sac-ED annealed to the same temperatures. Therefore, we can conclude again that sulfur reduced the thermal stability of the nanocrystalline microstructures in Ni-Mo layers. XLPA was also unable to determine the diffraction domain size for sample LMo-ED annealed to 1000 K. Therefore, EBSD was used to characterize the grain structure in this material (see Fig. 4.9e). The grain size from the EBSD image was determined as ~480 nm. This value is slightly higher than the grain size obtained after annealing at 720 K (~400 nm). For sample HMo-ED heated up to 1000 K, the grain size obtained from EBSD (see Fig. 4.9f) was much smaller (~90 nm) than for layer LMo-ED. In addition, in the former sample, considerable dislocation density and twin fault probability were detected, therefore recrystallization did not occur, only the defect density decreased, and the grains were coarsened from ~26 to ~90 nm. Thus, layer HMo-ED exhibited the best thermal stability among the studied samples.

4.2.2 The difference between the effects of Mo alloying and saccharin addition on the thermal stability of Ni-Mo films

It is evident from this study that although the addition of saccharin resulted in a similar trend in the change of the defect structure as Mo alloying, their influences on the thermal stability of the nanostructures were very different. Namely, while Mo alloying increased the stability, the addition of saccharin to the bath (and hence, doping the sample with sulfur) made the microstructure less stable, as shown in Fig. 4.7. For the visualization of this effect, Kernel Average Misorientation (KAM) maps were made for the EBSD images shown in Fig. 4.9. In the preparation of these maps, a local misorientation angle value was assigned to each pixel which was determined as the average misorientation between the studied central pixel and all pixels at the perimeter of the kernel around the investigated pixel. The same kernel radius of ~50 nm was used for all EBSD images in order to make their KAM maps comparable. The KAM maps were prepared for the misorientation angle range between 0 and 5°, and they indicate the local distortions in the microstructure. The comparison of the KAM maps in Figs. 4.10a and c reveal a higher distortion in the saccharin-free LMo-ED sample annealed at 720 K than that in the layer LMo-sac-ED heated up to the same temperature corresponding to the end of the DSC peak of the latter film. The higher lattice strain in the saccharin-free samples is more pronounced for the specimens with the higher Mo content annealed to 813 K (compare Figs. 4.10b and d). This temperature corresponds to the end of the exothermic DSC peak for the layer HMo-sac-ED. Increasing the temperature to 1000 K, the distortion decreased in both LMo-ED and HMo-ED samples; however, the lattice strain is still higher for the layer with the higher Mo content in accordance with the dislocation density measured by XLPA (see Figs. 4.10e and f). As we discussed above, although the higher Mo concentration increased the defect density and reduced the grain size thereby increasing the driving force for recovery and recrystallization,

the segregation of Mo at the grain boundaries impeded recrystallization and the latter effect was stronger as indicated by the better thermal stability of the sample HMo-ED compared to the specimen LMo-ED. At the same time, saccharin addition yielded only an increase of the defect density without the stabilization of the grain boundaries. Therefore, the saccharin-containing films exhibited a worse thermal stability as compared with their saccharin-free counterparts.

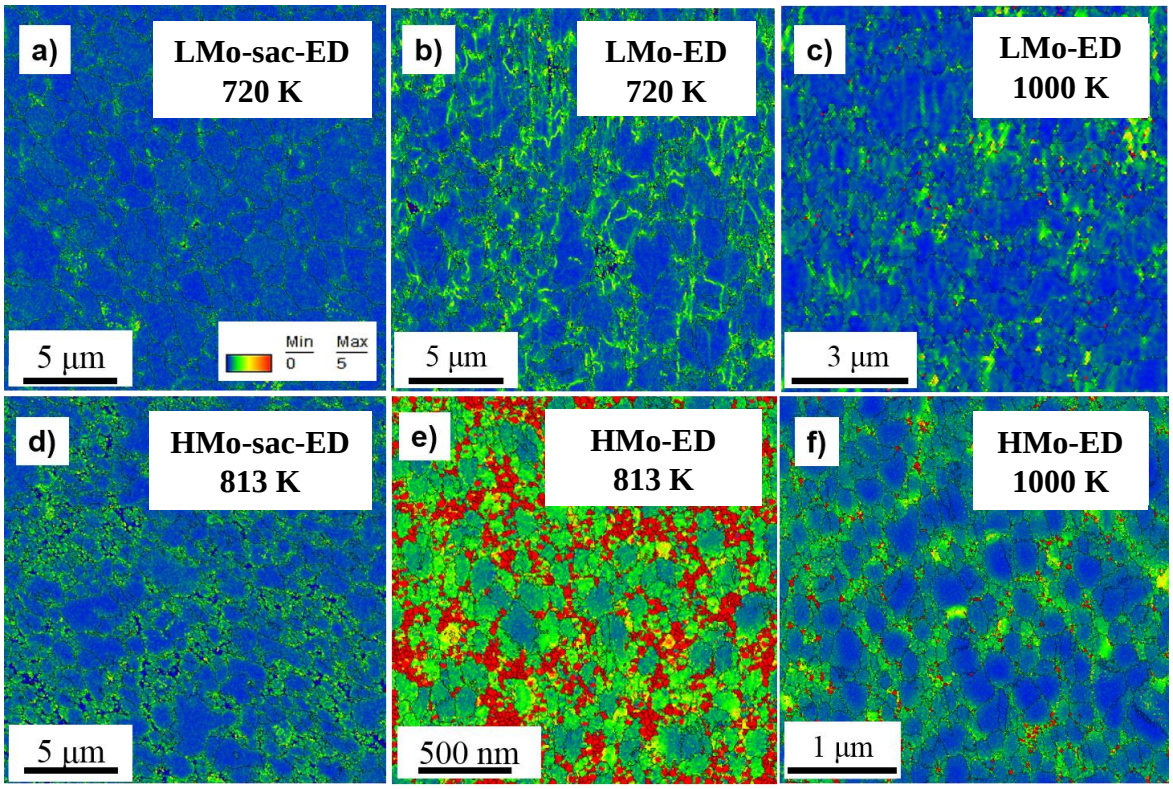

Fig. 4.10: KAM maps obtained for the EBSD images shown in Fig.4.9.

4.2.3 Calculation of the change of stored energy during annealing

The released heat measured by the direct method of DSC is intended to compare with the value calculated from the change of the microstructures during annealing. The stored energy per unit mass before and after the DSC peak is determined as the sum of the energies of the lattice defects investigated in this study (GBs, dislocations and twin faults). The energy stored in

dislocations (E_{disl}) can be obtained from the dislocation density using the following equation [149]:

$$E_{disl} = AGb^2 \frac{\rho}{\rho_m} ln\left(\frac{1}{b\sqrt{\rho}}\right), \quad (4.1)$$

where G is the shear modulus (82 GPa), b is the magnitude of Burgers vector (0.25 nm), ρ is the dislocation density, ρ_m is the mass density ~8.91 g cm^{-3} and A denotes a factor which depends on the material and the edge/screw character of the dislocations.

The value of A is equal to $(4\pi)^{-1}$ and $(4\pi(1-\upsilon))^{-1}$ for pure screw and edge dislocations, respectively, where υ is Poisson's ratio (taken as 0.3). The value of parameter q determined by XLPA describes the edge/screw character of dislocations. The theoretically calculated values of q for pure edge and screw dislocations in Ni are 1.38 and 2.21, respectively. In practice, the values of A were calculated from the experimentally determined q values using a simple rule of mixtures:

$$A = \frac{q - 1.62}{0.73}\frac{1}{4\pi} + \frac{2.35 - q}{0.73}\frac{1}{4\pi(1-\nu)}. \quad (4.2)$$

From the above calculation, the energy stored in dislocations for LMo-sac-ED and HMo-sac-ED samples before the DSC peak are 1.1 ± 0.2 J/g and 2.5 ± 0.5 J/g, respectively. It is noted that for the layer LMo-ED the stored energy at the beginning of the DSC peak was obtained as the weighted sum of the contributions from the fine- and coarse-grained volumes where the weights are the volume fractions estimated from the XRD peak intensities (0.89 and 0.11 for LMo-sac-ED and HMo-sac-ED samples, respectively). The dislocation density at the end of the DSC peak was lower than the detection limit of XLPA (10^{13} m^{-2}) for both samples which is two-three orders of magnitude lower than the value determined before the DSC peak. Therefore, this contribution to the stored energy is negligible. Thus, the difference in the energy stored in

dislocations before and after the DSC peak (ΔE_{disl}) is the same as the values at the beginning of DSC peak (see Table 2). It is clear that the dislocation contribution to the stored energy increases with increasing Mo concentration. The stored energy for twin faults (E_{twin}) can be calculated as [104]:

$$E_{twin} = \gamma_{twin} d^2 \frac{d}{d_{twin}} \frac{1}{d^3 \rho_m} = \frac{\gamma_{twin\beta}}{d_{111} \rho_m}, \quad (4.3)$$

where γ_{twin} is the twin fault energy per unit area in Ni (0.04 J/m^2 [191]), β is the twin fault probability determined by XLPA, d_{111} is the spacing between the neighboring {111} planes (0.20 nm) and d_{twin} is the mean twin-fault spacing which can be expressed as d_{111}/β. The value of E_{twin} were 0.20 ± 0.02 J/g and 0.8 ± 0.1 J/g for the films LMo-sac-ED and HMo-sac-ED, respectively, before the DSC peak and practically zero after the peak. The change of the twin fault energy (ΔE_{twin}) is shown for both LMo-sac-ED and HMo-sac-ED layers in Table 2.

The GB contribution to the stored energy is given as (E_{GB}) [192]:

$$E_{GB} = \frac{3\gamma_{GB}}{d\rho_m}, \quad (4.4)$$

where γ_{GB} is the GB energy per unit area in Ni and d is the average grain size. Former studies [153,193–195] have shown that the value of γ_{GB} for Ni and dilute Ni-Mo alloys varies between 0.4 and 1.4 J/m^2, depending on the misorientation between the neighboring grains, the GB orientation and the excess volume in the GB. As γ_{GB} is not known for our samples, its average values for LMo-sac-ED and HMo-sac-ED layers were determined by making the sum of the stored energy contributions of dislocations, twin faults and GBs equal with the released heats

obtained by DSC (see Table 4.2). This calculation yields 0.5 ± 0.2 and 0.7 ± 0.3 J/m^2 for the samples LMo-sac-ED and HMo-sac-ED, respectively.

Table 4.2: Calculated and measured stored energies for the electrodeposited Ni-Mo layers. ΔE_{disl}, ΔE_{twin} and ΔE_{GB} are the changes of the energies stored in dislocations, twin faults and grain boundaries, respectively. H is the heat released in the exothermic DSC peak and γ_{GB} is the specific grain boundary energy estimated from this analysis.

LMo-sac-ED	ΔE_{disl} [J/g]	1.1 ± 0.2
	ΔE_{twin} [J/g]	0.20 ± 0.02
	$\Delta E_{disl} + \Delta E_{twin}$ [J/g]	1.3 ± 0.2
	H [J/g]	5.6 ± 1.1
	ΔE_{GB} [J/g]	4.3 ± 1.3
	γ_{GB} [J/m^2]	**0.5 ± 0.2**
HMo-sac-ED	ΔE_{disl} [J/g]	2.5 ± 0.5
	ΔE_{twin} [J/g]	0.8 ± 0.1
	$\Delta E_{disl} + \Delta E_{twin}$ [J/g]	3.3 ± 0.6
	H [J/g]	14.3 ± 2.9
	ΔE_{GB} [J/g]	11.0 ± 3.5
	γ_{GB} [J/m^2]	**0.7 ± 0.3**

Table 4.2 shows that the calculated contributions of GBs, dislocations and twin faults to the heat released during the DSC peak are 77%, 20% and 3%, respectively, for sample LMo-sac-ED. The increase of the Mo content to about 5.3 at.% (layer HMo-sac-ED) yielded similar fractions: 77%, 17% and 6% for the contributions of GBs, dislocations and twin faults, respectively. Thus, it can be concluded that the majority of stored energy is attributed to GBs due to the very small grain sizes, irrespectively of the Mo concentration. The contribution of twin faults is marginal. The increase of Mo content from ~0.4 to ~5.3 at.% in the studied Ni films led to a 2-3 folds increase in the released heat due to the smaller grain size and the higher density of lattice defects.

The estimated specific GB energies for the present LMo-sac-ED and HMo-sac-ED films were 0.5 ± 0.2 and 0.7 ± 0.3 J/m^2, respectively. Similar values of γ_{GB} have been obtained recently for

other Ni-Mo electrodeposits [153]. In that work, the specific GB energy varied between 0.56 and 0.67 J/m^2 when the Mo concentration increased from zero to 5.6 at.% which is in a good agreement with our results. The significance of the slight increment of γ_{GB} with increasing Mo content cannot be determined due to the error of the GB energy values. At the same time, these values are certainly in the lower part of γ_{GB} range determined for Ni in previous studies [193–195]. It was shown that the GB energy in Ni varies between 0.4 and 1.4 J/m^2, and the value of γ_{GB} is significantly influenced by the GB orientation. For instance, the energy of {111}, {100} and {110} twist boundaries vary between 0.4-0.5, 0.6-1.0 and 0.9-1.3 J/m^2, respectively. In addition, the value of γ_{GB} increases with increasing the excess volume in GB. The relatively low values of GB energies for the Ni-Mo layers suggest low excess volume in the GBs.

4.3. Hardness evolution during annealing of electrodeposited Ni-Mo films

The evolution of hardness determined by Vickers indentation as a function of annealing temperature is shown in Fig.4.11. The temperatures used in the study of the hardness variation are the same as those applied in the investigation of the stability of the microstructures of the layers (see Fig. 4.6). As discussed in previous sections, the LMo-ED sample at RT has much higher grain size ~240 ± 15 nm and lower defect (dislocations and twin faults) density compared to specimen HMo-ED as well as the saccharin containing samples. This can explain the lowest hardness value of layer LMo-ED before annealing in comparison with the other investigated Ni-Mo layers. It should be noted, however, that for specimens HMo-ED, LMo-sac-ED and HMo-sac-ED the hardness values are very close despite the very different dislocation densities and twin fault probabilities. These three samples have grain sizes between 20 and 30 nm (see Table 4.1). Former studies have shown that for fcc metals and alloys in this grain size regime, the main deformation mechanism changes from dislocation glide to grain boundary sliding [196]. As a result, the increase of the defect density in the grain interiors does not yield hardness

enhancement due to the increased role of grain boundary sliding. In addition, grain refinement from 30 to 20 nm does not lead to hardening owing to the change of the deformation mechanism.

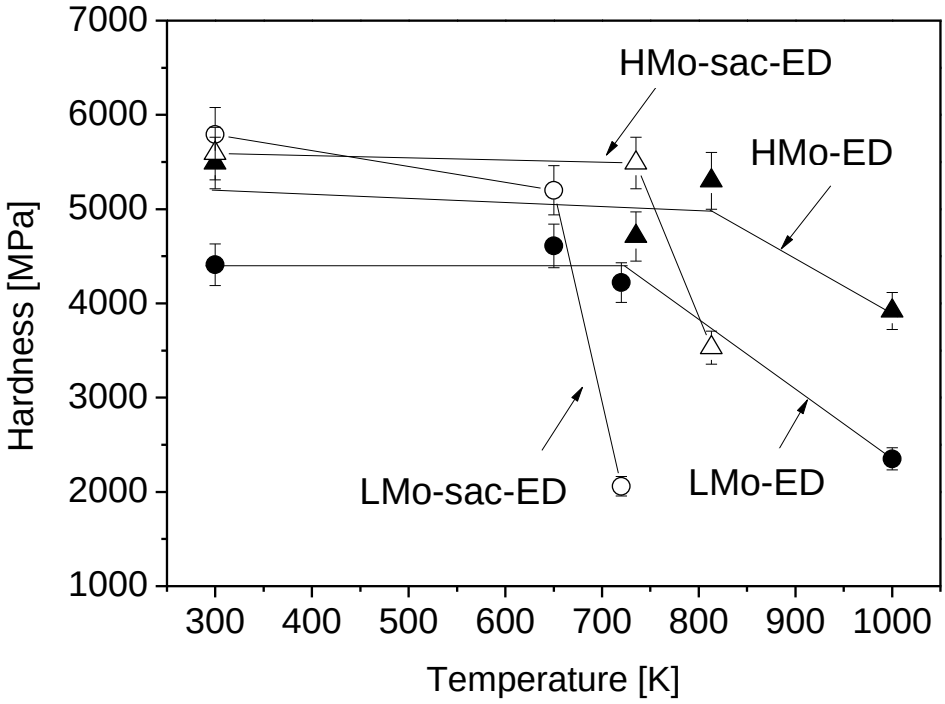

Fig. 4.11: Hardness evolution as a function of annealing temperature for samples LMo-ED, HMo-ED, LMo-sac-ED and HMo-sac-ED.

The change of the hardness during annealing of the different Ni-Mo films reflects the difference observed in the stability of the microstructures. Annealing to the characteristic temperatures corresponding to the DSC peaks (see Fig. 4.6) followed the general trend of hardness reduction on the increasing annealing temperature. It is apparent that the hardness decreases more sharply between the temperatures corresponding to the beginning and the end of DSC peaks than before the occurrence of DSC peak. It was found that the addition of saccharin reduced the temperature of the large hardness reduction. At the same time, the increase of Mo content increased the thermal stability of the layers. Among all the layers, the minimum variation in hardness value

on annealing occurs in HMo-ED layer. This can be explained by the highest thermal stability of microstructure and defect structure exhibited by high Mo specimen without the addition of saccharin. As discussed in previous sections, the addition of Mo retards the recovery and recrystallization of the nanocrystalline microstructure, owing to the pinning effect of Mo on the lattice defects.

It is worth noting that no annealing-induced hardening was observed in the studied electrodeposited Ni-Mo layers, unlike HPT-processed specimens with similar compositions. However, the possibility of existence of such annealing-induced hardening in the studied samples cannot be ruled out. Even if such hardening effect occurs in the case of the studied Ni-Mo layers, it may be limited to the temperature range below the characteristic temperatures corresponding to the measured samples and hence could not be detected. Indeed, a former study [171] showed that for electrodeposited layers with the compositions corresponding to our LMo-ED and HMo-ED samples anneal-hardening occurred at about 500 and 600 K which are considerably smaller than the lowest annealing temperatures used in the present study (see Fig. 4.11).

Chapter 5: Comparison between SPD processed and ED-Ni Mo alloys

In this chapter, the influence of the processing route on the microstructure, defect structure and thermal stability is shown. The microstructure and the thermal stability of the electrodeposited Ni-Mo layers are compared with similar results obtained on Ni-Mo bulk counterparts with very similar compositions but processed by HPT (see the chapter 3), i.e., materials processed by bottom-up and top-down techniques are contrasted. The stored energy in nanocrystalline Ni-Mo thin films processed by electrodeposition was studied experimentally by DSC and compared with the values calculated from the parameters of the microstructure. The GB energy and the concentration of vacancies, which was estimated indirectly from the difference between the measured and the calculated released heats, are also determined in this chapter.

5.1. Comparison of the Microstructures

The present study demonstrated that Mo alloying has a significant effect on the microstructure and its thermal stability in nanocrystalline Ni layers processed by electrodeposition. The increase of Mo content from ~0.4 to ~5.3 at.% resulted in an increase of the dislocation density from ~23 × 10^{14} to ~114 × 10^{14} m^{-2} while the grain size decreased from ~240 nm to ~26 nm. Similar trends were observed when the Mo content increased from ~0.3 to ~5 at.% in UFG bulk Ni processed by SPD using the method of HPT [172]. For this top-down technique, the dislocation density increased from ~27 ×10^{14} to ~59 ×10^{14} m^{-2} while the grain size decreased from ~182 nm to ~125 nm owing to the higher Mo concentration. It is evident that for the bottom-up method of electrodeposition the effect of Mo on the as-processed microstructure was more pronounced since a similar increase of Mo concentration yielded 5-fold and 2-fold increase in the dislocation density for electroplating and HPT, respectively. In addition, the grain size was reduced by one order of magnitude for electrodeposition while for HPT the grain

size decreased only with a factor of ~1.5. Moreover, significant twin fault probability ~3.9% was measured for the electrodeposited layer containing ~5.3 at.% Mo but the similar Mo concentration in the HPT-processed UFG Ni-Mo alloy did not yield considerable twinning. It should also be noted that for the large Mo content, a higher defect density and a smaller grain size could be achieved by electrodeposition than by HPT method.

The difference between the defect structures obtained by the applied bottom-up and top-down techniques can be explained by the different formation mechanisms of lattice defects. Namely, deformation-induced and grown-in defects were formed during HPT and electrodeposition, respectively. In the case of HPT, plastic deformation resulted in a multiplication of dislocations, and the maximum dislocation density is determined primarily by the annihilation rate of dislocations. The higher the melting point, the lower the SFE and the higher the solute element concentration, the more retarded the dislocation annihilation [18]. Therefore, the pinning effect of Mo solute atoms on dislocations formed during HPT impedes their annihilation, thereby increasing the dislocation density. However, the dislocation density cannot increase above a limiting value, as close dislocations with opposite signs are annihilated due to the attractive force between them. This is especially valid for the statistically stored dislocations which are not necessary for the accommodation of misorientations between the differently orientated crystallites. In the case of electrodeposition, the dislocations are not deformation-induced defects, but they are grown-in defects formed for the reduction of the mismatch stresses at the non-coherent grain boundaries [150–152]. Thus, these defects can be considered as geometrically necessary dislocations, and their density is rather determined by the deposition parameters controlling the grain size than by the material properties (e.g., the melting point or SFE). Accordingly, the smaller grain size is usually accompanied by a higher dislocation density as suggested in a recent study on nanocrystalline electrodeposited Ni films [15]. Twin faults (or twin boundaries) also contribute to the accommodation of misorientations in the as-

deposited layer, but they usually form coherent boundaries between crystallites [197,198]. Therefore, the formation of twin faults during electrodeposition is a reasonable process while SPD-processing did not yield considerable twinning in Ni-Mo alloys due to their high SFE (twin fault energy is proportional with SFE in fcc crystals).

5.2. Comparison of the Thermal Stability

Large differences between the defect structures and the grain sizes in the samples processed by electrodeposition and HPT were observed for the higher Mo content. The larger defect density and the smaller grain size for the electrodeposited layer evidently led to a higher driving force for recovery and recrystallization during annealing, thus a worse stability for the electrodeposited film is expected as compared to the HPT sample.

Fig. 5.1a compares the evolution of the dislocation density versus the annealing temperature for the electrodeposited layer and the bulk HPT-processed sample with ~5 at.% Mo. For the latter specimen, the data were taken from Ref. [199]. Similar to the electrodeposited layers, for the HPT-processed Ni-Mo alloy the heat-treatments were also carried out in a DSC by heating the samples up to characteristic temperatures of the thermogram at the same heating rate of 40 K/min and then quenched to RT. Up to about 800 K, only recovery occurred in both samples as revealed by the spot-free Debye-Scherrer rings. In this temperature range, the decrease of the dislocation density for the electroplated layer is higher which can be explained by the larger driving force for recovery owing to the higher initial dislocation density. If the dislocation density is normalized by the initial value, similar temperature dependence is obtained for both samples as revealed in Fig. 5.1b. A large difference between the two specimens was observed between ~800 and ~1000 K, as while the HPT-processed sample was recrystallized, in the electrodeposited layer only the recovery continued. At 1000 K, the dislocation densities in the

electroplated and HPT-processed specimens decreased to ~7 $\times 10^{14}$ m^{-2} and below 10^{13} m^{-2}, respectively.

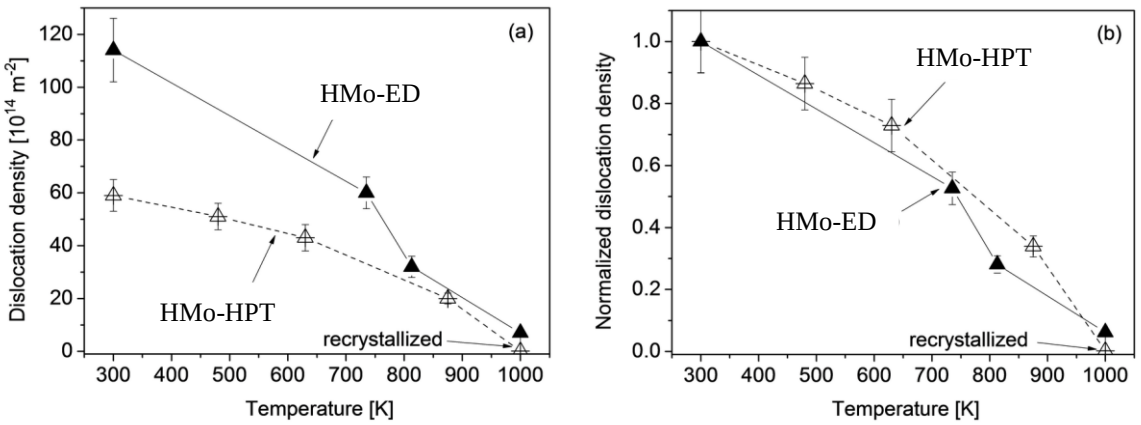

Fig. 5.1: (a) The dislocation density evolution versus the annealing temperature for the electrodeposited (HMo-ED) and the HPT-processed (HMo-HPT) Ni alloys with the higher (~5 at.%) Mo concentration. Image (b) shows the evolution of the dislocation density normalized with the initial (before annealing) value.

The different resistance to recrystallization of the two samples may be caused by the different nature of the dislocation structures. In the electrodeposited film, the majority of dislocations are assumed to be geometrically necessary dislocations located at the grain boundaries. Due to the small grain size (about 30 nm), most probably dislocations are not stored in the grain interiors. The relatively good agreement between the diffraction domain size and the grain size also suggest that dislocation walls and subgrain boundaries were not formed inside the grains. At the same time, for the HPT-processed sample, the diffraction domain size is significantly smaller than the grain size [199], suggesting that a considerable fraction of dislocations was stored in the grain interiors. As Mo solute atoms have a 10% larger size than the Ni matrix atoms, they are located preferentially at dislocations. Since the majority of dislocations can be found at the grain boundaries in the electrodeposited film, the segregation of Mo solute atoms at the grain boundaries was more pronounced in this sample. Indeed, a recently published study proved the enrichment of grain boundaries with Mo in electroplated Ni-Mo films [171]. Similar segregation was observed previously for other Ni alloys such as Ni-W [200–202]. It was found

that the concentration of W at the boundaries of the columnar grains is 50% higher than in the grain interiors of Ni-W layers when direct current is used for deposition [200]. This effect was less pronounced when pulsed current was applied. Computer simulations have shown that the segregation tendency decreased with increasing the total W concentration due to the filling of the energetically preferable grain boundary sites with solute W atoms [201]. In our samples, the high concentration of Mo at the grain boundaries impeded the motion of grain boundaries during annealing, thereby retarding grain growth and recrystallization.

5.3. Comparison of the Stored Energies

The stored energy obtained for the Ni-Mo layers produced by electrodeposition is worth to compare with the values determined on UFG counterparts processed for 20 turns of HPT [199]. For specimen LMo-HPT, the exothermic DSC peak started at ~400 K and finished at ~830 K. For the high Mo concentration, the DSC signal began at a similar temperature, however, the end temperature was shifted to 1000 K. The areas under the whole DSC signal were 4.7 ± 0.9 J/g and 7.9 ± 1.6 J/g for samples LMo-HPT and HMo-HPT, respectively.

The released heats determined experimentally for the HPT-processed specimens were lower than the values obtained for the present electrodeposited samples, especially for the materials with the higher Mo content (see Table 4.2). This difference between the electrodeposited and HPT processed samples can be attributed to the higher grain size (130-180 nm) and the lower dislocation density (27-59 $\times$ 10^{14} m^{-2}) in the latter specimens. The contribution of dislocations to the released heat for both samples LMo-HPT and HMo-HPT was calculated from the changes of the dislocation density during annealing using eq. (4.1) and the values are listed in Table 5.1. The probability of twin faults was lower than the detection limit of XLPA, therefore, their contribution to the stored energy was lower than 0.01 J/g (see Table 5.1). The heat released due to grain growth was calculated from eq. (4.4). However, as the specific GB energy for the HPT-

processed samples is unknown, a lower and an upper limit were calculated for ΔE_{GB} in accordance with the lowest (0.4 J/g) and highest (1.4 J/g) literature values of γ_{GB} (see section 3.4). The corresponding ΔE_{GB} values are listed in Table 5.1. It can be seen that the GB fraction in the released heat was significantly smaller (less than 55%) for the HPT-processed UFG Ni-Mo alloys than the value obtained for the nanocrystalline electrodeposited films (~77%).

The sum of the contributions of dislocations, twin faults and GBs to the released heat is 1.2-2.6

Table 5.1: Calculated and measured stored energies for the Ni-Mo samples processed by HPT. ΔE_{disl}, ΔE_{twin} and ΔE_{GB} are the changes of the energies stored in dislocations, twin faults and grain boundaries, respectively. H is the heat released in the exothermic DSC peak. ΔE_{vac} is the calculated change of energy stored in vacancies and Δc_v is the estimated change of vacancy concentration during annealing.

LMo-HPT	ΔE_{disl} [J/g]	0.6 ± 0.1
	ΔE_{twin} [J/g]	< 0.01
	ΔE_{GB} [J/g]	0.6-2.0 (± 10%)
	Sum [J/g]	1.2-2.6 (± 15%)
	H [J/g]	4.7 ± 0.9
	ΔE_{vac} [J/g]	2.1-3.5 (± 50%)
	Δc_v [10^{-4}]	**(0.7-1.2) × 10^{-3} (± 50%)**
HMo-HPT	ΔE_{disl} [J/g]	1.2 ± 0.3
	ΔE_{twin} [J/g]	< 0.01
	ΔE_{GB} [J/g]	0.6-2.1 (± 10%)
	Sum [J/g]	1.8-3.3 (± 15%)
	H [J/g]	7.9 ± 1.6
	ΔE_{vac} [J/g]	4.6-6.1 (± 50%)
	Δc_v [10^{-4}]	**(1.6-2.1) × 10^{-3} (± 50%)**

J/g for LMo-HPT sample which is much lower than the heat released obtained by DSC (4.7 ± 0.9 J/g). Similarly, for the specimen HMo-HPT the calculated change of the stored energy (1.8-3.3 J/g) is found to be much lower than the measured released heat (7.9 ± 1.6 J/g). The difference can be attributed to the annihilation of vacancies and/or vacancy clusters. Indeed, former publications [149,203] indicated that a very high concentration of vacancies developed during SPD-processing. If the difference between the calculated and experimentally determined

released heat values is attributed to vacancies, this difference can be used for the determination of the vacancy concentration in the HPT-processed Ni-Mo alloys as shown in the next paragraph.

The energy stored in vacancies (E_{vac}) may be expressed by the measured vacancy concentration (c_v) as [149]:

$$E_{vac} = e_{vac} C_v \frac{N_A}{M}, \tag{5.1}$$

where e_{vac} is the formation energy of a vacancy in Ni (1.8 eV = 2.9×10^{-19} J [109]), NA is Avogadro's number (6×10^{23} mol^{-1}) and M is the molar mass of Ni (58.7 g/mol). Thus, the change of vacancy concentration (Δc_v) during annealing can be calculated from the energy stored in the annihilated vacancies (ΔE_{vac}). This energy was estimated as the difference between the heat released during DSC and the sum of energies of other defects (dislocations and grain boundaries). In our case, due to the uncertainty of the specific GB energy, a range was obtained for Δc_v (see Table 5.1). For low and high Mo contents, the vacancy concentrations annihilated during the DSC peak were obtained as (0.7-1.2) $\times 10^{-3}$ and (1.6-2.1) $\times 10^{-3}$, respectively. These very high values are in accordance with the vacancy concentrations determined formerly in SPD-processed metallic materials [149]. These excess vacancies were formed due to the climb of edge dislocations and the movement of jogs during SPD. As the dislocation density is much higher for sample HMo-HPT than that for specimen LMo-HPT, a higher vacancy concentration is expected for the larger Mo content which is in accordance with the present results. Vacancies and vacancy clusters may also exist in the electroplated layers, and they can be annihilated during DSC annealing. Their maximum possible vacancy concentration can be estimated from the released heat if we minimize the GB energy with the selection of the lowest limit of γ_{GB} (0.4 J/m^2). Then, the rest of the released heat is associated with vacancies which yields Δc_v=0.2 $\times 10^{-3}$ and 1.7 $\times 10^{-3}$ for LMo-sac-ED and HMo-sac-ED films, respectively. These values are

smaller than the vacancy concentrations determined with the same γ_{GB} for the HPT-processed samples (see Table 5.1), especially in the case of specimen LMo-HPT (1.2×10^{-3}). This result suggests that the excess vacancy concentration in the electroplated Ni-Mo alloys is lower than that in the SPD processed counterparts even if its value was not determined precisely.

New Scientific Results

1. Both Ni alloys with low (0.3%) and high (5%) Mo contents remain in solid solution state even after cryorolling and HPT. Although the grain size was not refined into the UFG regime during cryorolling, there were very high dislocation densities (~15-35 × 10^{14} m^{-2}) in both alloys. HPT at RT led to further enhancement in the dislocation density up to ~30-60 × 10^{14} m^{-2} and a concomitant gradual grain refinement below 200 nm. Irrespective of the Mo content, the saturation of the dislocation density occurred earlier (after 5 turns) than for the grain size (only after 20 turns) during combined cryorolling and HPT. The minimum grain size and the maximum dislocation density values are, respectively, smaller and higher in the alloy with high Mo content than in the material with low Mo concentration due to the pinning effect of Mo atoms on the lattice defects. This effect also hinders the clustering of dislocations within the grains, as indicated by the higher value of the dislocation arrangement parameter.

2. The hardness for both alloys saturated and became homogeneous along the disk radii after 5 turns of HPT. The maximum hardness values achieved for 0.3% and 5% Mo concentrations were ~3200 and ~4300 MPa, respectively. The higher saturation hardness with 5% Mo is in accordance with the microstructural observations. It is demonstrated that the hardening caused by the combined process of cryorolling and HPT may be related to the increase of the dislocation density using the Taylor equation. The α parameter in this equation has a lower value for the higher Mo content due to the less clustered dislocation structure.

3. For the HPT-processed samples, the recovery of the UFG microstructures started at ~400 K irrespective of the Mo content, but recrystallization occurred at a much higher temperature for the Ni alloy with higher Mo content. During recovery, the low-angle grain boundary fraction increased due to the arrangement of dislocations into low energy configurations, such as low-angle grain boundaries. In the recrystallization process, the fraction of low-angle grain boundaries decreased. The temperature range of the recovery is much larger for the alloy with higher Mo content (~515 K) than that for the sample with lower Mo content (~280 K). After annealing up to ~1000 K, the grain size remained much smaller for the sample with higher Mo concentration. Moreover, the larger Mo content yielded a separation of recovery and recrystallization processes in the DSC thermogram. In comparison to the sample with lower Mo content, there is a much higher onset temperature of recrystallization for the alloy with higher Mo concentration due to the segregation of solute Mo atoms at the grain boundaries which may reduce the grain boundary energy and additionally hinders the motion of the grain boundaries. The higher Mo concentration has a more pronounced hindering effect on recrystallization than on recovery. It is concluded that the higher Mo content significantly increases the stability of the SPD-processed UFG microstructure in Ni.

4. Annealing to ~600 K resulted in a considerable hardening for the sample with lower Mo content while the ductility remained unchanged. This annealing-induced hardening was explained by the annihilation of mobile dislocations and the clustering of the remaining dislocations into subgrain boundaries. An increase of the Mo concentration in UFG Ni led to a much lower annealing-induced hardening which was explained by the hindering effect of Mo atoms on the annihilation and clustering of dislocations. Therefore, the influence of Mo content on the annealing-induced hardening in UFG Ni-Mo alloys is

opposite to the trend observed formerly for their nanocrystalline counterparts processed by bottom-up methods due to the different strengthening mechanisms. Annealing to high temperatures resulted in a simultaneous reduction in the strength and an improvement in the ductility in UFG Ni-Mo alloys. The softening and the increase of ductility were lower for the alloy with higher Mo concentration, indicating a better thermal stability of this sample compared to the sample with lower Mo content.

5. In the electrodeposited Ni-Mo layers, the increase of Mo content resulted in a smaller grain size as well as a higher dislocation density and twin fault probability in the Ni layers. This effect is more pronounced for the electrodeposited films than for the UFG Ni-Mo alloys with similar compositions but processed by SPD. This difference can be attributed to the different formation mechanisms of lattice defects: during SPD-processing and electrodeposition deformation-induced and grown-in defects were formed, respectively. The addition of saccharin to the electrolyte bath also yielded an increase of the lattice defect density in Ni-Mo layers for both low and high Mo contents. This effect can be explained by the co-deposition of sulfur together with Ni. The increase of the defect density due to saccharin addition is more pronounced for Ni film with low Mo concentration.

6. The increase of Mo concentration in Ni films resulted in a considerable improvement of the thermal stability of the nanocrystalline microstructure. The improved stability due to Mo alloying can be attributed to the pinning effect of Mo on the lattice defects such as dislocations and grain boundaries, thereby retarding recovery and recrystallization of the nanocrystalline microstructure. The electrodeposited film with higher Mo concentration exhibited a better stability than the SPD-processed counterpart with the same Mo content. Although both Mo alloying and saccharin addition resulted in a strong

increase of the lattice defect density in electrodeposited Ni layers, their effects on the thermal stability were significantly different. Namely, saccharin yielded a significant reduction of the thermal stability of the nanocrystalline Ni microstructure because this additive increased the defect density during deposition, thereby enhancing the thermodynamic driving force for recovery and recrystallization. At the same time, the impurity elements (e.g., sulfur) deposited from saccharin cannot hinder effectively the recovery and recrystallization of the nanocrystalline microstructure in Ni films, causing a reduced thermal stability.

7. The stored energy investigation for the electroplated Ni films with both low and high Mo contents revealed that the majority of the released heat (~77%) can be attributed to the contribution of grain boundaries while the rest was caused by the annihilation of dislocations and twin faults. From the equality between the measured and calculated released heats, the grain boundary energy was estimated as ~0.5 and ~0.7 J/m^2 for low and high Mo concentrations, respectively. These values are in the lower part of the possible grain boundary energy range (0.4 - 1.4 J/m^2), suggesting a low excess volume in the grain boundaries of the present electroplated films. The grain boundary fraction in the released heat was significantly smaller (less than 55%) for UFG Ni-Mo samples with similar compositions but processed by HPT. For these specimens, the sum of the heat contributions of grain boundaries, dislocations and twin faults was much smaller than the released heat obtained by DSC. The difference was attributed to vacancies and vacancy clusters. The estimated vacancy concentration was about 10^{-3}. The higher Mo content yielded a two times larger vacancy concentration. The electroplated layers contain less vacancies than the HPT-processed samples, especially for low Mo content. The increase of Mo concentration in the electrodeposited films from ~0.4 at.% to ~5.3

at.% resulted in an enhancement of the stored energy with a factor of about two. This change is caused by the larger defect density and the smaller grain size. The influence of Mo content on the stored energy is less pronounced in the samples processed by HPT.

8. The investigation of the hardness of the electrodeposited Ni-Mo films showed that before annealing the saccharin-free layer with low Mo content has the lowest hardness value in comparison with the other investigated Ni-Mo layers. This can be explained by the much higher grain size and lower dislocation density for this film compared to the other three electrodeposited samples. For other investigated layers, the hardness values were very close, despite the very different dislocation densities and twin fault probabilities. The grain size values for these three samples were very small (between 20 and 30 nm), which can cause change of the main deformation mechanism from dislocation glide to grain boundary sliding. Among all the layers, the minimum variation in the hardness during annealing was observed in the saccharin-free layer with high Mo content in accordance with the best thermal stability of the microstructure of this film. Furthermore, the addition of saccharin reduced the temperature of the large hardness reduction. At the same time, the increase of Mo content increased the thermal stability of the layers. Unlike HPT processed samples, no annealing-induced hardening was observed in the studied electrodeposited Ni-Mo layers.

Publication List

Publications related to this Thesis:

P1. **Kapoor G**, Huang Y, Sarma VS, Langdon TG, Gubicza J, Effect of Mo addition on the microstructure and hardness of ultrafine-grained Ni alloys processed by a combination of cryorolling and high-pressure torsion, Materials Science and Engineering A 688: 92-100 (2017).

P2. **Kapoor G,** Huang Y, Sarma VS, Langdon TG, Gubicza J, Evolution of the microstructure during annealing of ultrafine-grained Ni with different Mo contents, Materials Characterization 130: 56-63 (2017).

P3. **Kapoor G,** Huang Y, Sarma VS, Langdon TG, Gubicza J, Influence of Mo alloying on the thermal stability and hardness of ultrafine-grained Ni processed by high-pressure torsion, Journal of Materials Research and Technology 6:(4) 361-368 (2017).

P4. Gubicza J, Pereira PHR, **Kapoor G**, Huang Y, Sarma VS, Langdon TG, Annealing-induced Hardening in Ultrafine-grained Ni-Mo Alloys, Advanced Engineering Materials 20:(9) 1800184 (1-4) (2018).

P5. **Kapoor G**, Péter L, Fekete E, Gubicza J, Defect structure in electrodeposited nanocrystalline Ni layers with different Mo concentrations, AIP Conference Proceedings 1953, 030047 (2018).

P6. **Kapoor G**, Péter L, Fekete E, Lábár JL, Gubicza J, The influence of Mo addition on the microstructure and its thermal stability for electrodeposited Ni films, Materials Characterization 145: 563-572 (2018).

P7. **Kapoor G**, Péter L, Fekete E, Lábár JL, Gubicza J, Stored energy in nanocrystalline Ni-Mo films processed by electrodeposition, Journal of Alloys and Compounds 796: 307-313 (2019).

Other publication:

P8. Athreya CN, **Kapoor G**, Gubicza J and Sarma VS, Influence of mode of plastic straining on the microstructure of Ni and Ti deformed through rolling and torsion, Materials Characterization 132: 205-214 (2017).

Acknowledgment

In September 2015, I received Stipendium Hungaricum scholarship, to pursue doctoral studies in Hungary. Though it has been more than four years now since I left India, but not even once I regret the decision to come to Hungary and join the department of materials physics at the ELTE.

I conducted my doctoral research under the supervision of eminent professor, **Jenő Gubicza**, who is highly respected and well renowned in this field. I could not have imagined more support, guidance and encouragement than he provided throughout my time as his student. I feel privileged to have a supervisor who cared so much about my work, and who responded to my questions and queries so promptly, even when he was preoccupied with other responsibilities. I express my sincere thanks to him for providing excellent research opportunities and valuable insights.

I am also grateful to our head of department, Prof. **István Groma**, who always offered his kind support and corporation in difficult administrative situations. I would like to express my gratitude to all other staff members of the Department of Materials Physics of ELTE who helped me in completing my PhD studies. In particular, I want to thank the whole team of SEM laboratory including **Gábor Varga, Zoltán Dankházi, Ábel Szabó** and **Ádám Vida** for their support in SEM investigations, **János Lábár** and **György Radnóczi** for TEM investigations, **Alajos Ö. Kovács** for assistance in sample preparation and DSC measurements, **Nguyen Quang Chinh** for hardness testing, **Peter Szommer** and **Zoltán Dankházi** as well for their technical support, especially in fixing my computer.

I would like to thank my co-authors **Terence G Langdon, Yi Huang, Pedro HR Pereira, László Péter, Éva Fekete, Vadlamani S Sarma** for their continuous cooperation. My senior labmates, **Anita Heczel** (my first Hungarian friend), **Moustafa Mamdouh Taha El-Tahawy**

and **Péter Jenei**, for their consistent support and advice. I really appreciate Anita for giving me professional and personal support.

From the depth of my heart, I am thankful to my sister **Heena Kapoor** and my brother **Gaurav Kapoor**, for always being there for me. Above all, I would like to dedicate this PhD thesis to my loving parents, for their continuous love and motivation. Thank you for always believing in me.

References

[1] D.E. Brown, M.N. Mahmood, M.C.M. Man, A.K. Turner, Preparation and characterization of low overvoltage transition metal alloy electrocatalysts for hydrogen evolution in alkaline solutions, Electrochim. Acta. 29 (1984) 1551–1556. doi:10.1016/0013-4686(84)85008-2.

[2] R. Schulz, J.Y. Huot, M.L. Trudeau, L. Dignard-Bailey, Z.H. Yan, S. Jin, et al., Nanocrystalline Ni-Mo alloys and their application in electrocatalysis, J. Mater. Res. 9 (1994) 2998–3008. doi:10.1557/JMR.1994.2998.

[3] J.R. McKone, B.F. Sadtler, C.A. Werlang, N.S. Lewis, H.B. Gray, Ni–Mo Nanopowders for Efficient Electrochemical Hydrogen Evolution, ACS Catal. 3 (2013) 166–169. doi:10.1021/cs300691m.

[4] P.P. Bhattacharjee, R.K. Ray, A. Upadhyaya, Nickel base substrate tapes for coated superconductor applications, J. Mater. Sci. 42 (2007) 1984–2001. doi:10.1007/s10853-006-1416-6.

[5] T. Ohgai, Y. Tanaka, R. Washio, Nanocrystalline structure and soft magnetic properties of nickel-molybdenum alloy thin films electrodeposited from acidic and alkaline aqueous solutions, J. Solid State Electrochem. 17 (2013) 743–750. doi:10.1007/s10008-012-1924-z.

[6] P.C. Huang, K.H. Hou, H.H. Sheu, M.D. Ger, G.L. Wang, Wear properties of Ni–Mo coatings produced by pulse electroforming, Surf. Coatings Technol. 258 (2014) 639–645. doi:10.1016/J.SURFCOAT.2014.08.024.

[7] E.B. Lehman, A. Bigos, P. Indyka, M. Kot, Electrodeposition and characterisation of nanocrystalline Ni–Mo coatings, Surf. Coatings Technol. 211 (2012) 67–71. doi:10.1016/J.SURFCOAT.2011.10.011.

[8] K. Frisk, A Thermodynamic Evaluation of the Mo-Ni System, Calphad. 14 (1990) 311–320. doi:10.1016/0364-5916(90)90031-T.

[9] P. Franke, D. Neuschütz, Mo-Ni, in: P. Franke, D. Neuschütz (Eds.), Bin. Syst. Part 4 Bin.

Syst. from Mn-Mo to Y-Zr, Springer Berlin Heidelberg, Berlin, Heidelberg, 2006: pp. 1–3. doi:10.1007/10757285_13.

[10] Y. Cui, Z. Jin, X. Lu, Experimental study and thermodynamic assessment of the Ni-Mo-Ta ternary system, Metall. Mater. Trans. A. 30 (1999) 2735–2744. doi:10.1007/s11661-999-0110-0.

[11] S.I. Shah, G.H. Jaffari, E. Yassitepe, B. Ali, Evaporation: Processes, Bulk Microstructures, and Mechanical Properties, in: P.M. Martin (Ed.), Handb. Depos. Technol. Film. Coatings, William Andrew Publishing, 2010: pp. 135–252. doi:10.1016/B978-0-8155-2031-3.00004-1.

[12] H. Gleiter, Nanocrystalline materials, Prog. Mater. Sci. 33 (1989) 223–315. doi:10.1016/0079-6425(89)90001-7.

[13] J.O. Carlsson, P. M.Martin, Chemical Vapor Deposition, William Andrew Publishing, 2010. doi:10.1016/B978-0-8155-2031-3.00007-7.

[14] C. Suryanarayana, B. Prabhu, Synthesis of Nanostructured Materials by Inert-Gas Condensation Methods, Nanostructured Mater. (2007) 47–90. doi:10.1016/B978-081551534-0.50004-X.

[15] T. Kolonits, P. Jenei, L. Péter, I. Bakonyi, Z. Czigány, J. Gubicza, Effect of bath additives on the microstructure, lattice defect density and hardness of electrodeposited nanocrystalline Ni films, Surf. Coatings Technol. 349 (2018) 611–621. doi:10.1016/j.surfcoat.2018.06.052.

[16] B. Zhang, Physical fundamentals of nanomaterials, William Andrew Publishing, Boston, 2018. doi:10.1016/C2012-0-02139-4.

[17] J. Lv, Effect of grain size on mechanical property and corrosion resistance of the Ni-based alloy 690, J. Mater. Sci. Technol. 34 (2018) 1685–1691. doi:10.1016/J.JMST.2017.12.017.

[18] J. Gubicza, Defect structure in nanomaterials, Woodhead Publishing Limited, Cambridge, UK, 2012. doi:10.1533/9780857096142.

[19] A. Azushima, R. Kopp, A. Korhonen, D.Y. Yang, F. Micari, G.D. Lahoti, et al., Severe plastic deformation (SPD) processes for metals, CIRP Ann. 57 (2008) 716–735. doi:10.1016/J.CIRP.2008.09.005.

[20] Y. Estrin, A. Vinogradov, Extreme grain refinement by severe plastic deformation: A wealth of challenging science, Acta Mater. 61 (2013) 782–817. doi:10.1016/j.actamat.2012.10.038.

[21] D. Gunderov, A. Lukyanov, E. Prokofiev, A. Churakova, V. Pushin, S. Prokoshkin, et al., Microstructure and Mechanical Properties of the SPD-Processed TiNi Alloys, Mater. Sci. Forum. 738–739 (2013) 486–490. doi:10.4028/www.scientific.net/MSF.738-739.486.

[22] P. Cavaliere, Mechanical Properties of Nanocrystalline Materials, Handb. Mech. Nanostructuring. 1 (2015) 3–16. doi:10.1002/9783527674947.ch1.

[23] V. Segal, Review: Modes and Processes of Severe Plastic Deformation (SPD)., Mater. (Basel, Switzerland). 11 (2018). doi:10.3390/ma11071175.

[24] M. Krystian, J. Horky, D. Colas, S. Neodo, F. Diologent, Microstructure, mechanical properties, and thermal stability of lean, copper-free silver alloy subjected to equal channel angular pressing (ECAP) and subsequent post-processing, Mater. Sci. Eng. A. 757 (2019) 52–61. doi:10.1016/J.MSEA.2019.04.052.

[25] G.B. Rathmayr, A. Hohenwarter, R. Pippan, Influence of grain shape and orientation on the mechanical properties of high pressure torsion deformed nickel, Mater. Sci. Eng. A. 560 (2013) 224–231. doi:10.1016/J.MSEA.2012.09.061.

[26] R.Z. Valiev, A.P. Zhilyaev, T.G. Langdon, Bulk Nanostructured Materials, John Wiley & Sons, Inc, Hoboken, NJ, 2013. doi:10.1002/9781118742679.

[27] A.P. Zhilyaev, G.V. Nurislamova, B.K. Kim, M.D. Baró, J.A. Szpunar, T.G. Langdon, Experimental parameters influencing grain refinement and microstructural evolution during high-pressure torsion, Acta Mater. 51 (2003) 753–765. doi:10.1016/S1359-6454(02)00466-4.

[28] A.P. Zhilyaev, T.G. Langdon, Using high-pressure torsion for metal processing: Fundamentals and applications, Prog. Mater. Sci. 53 (2008) 893–979. doi:10.1016/J.PMATSCI.2008.03.002.

[29] A. Hohenwarter, A. Bachmaier, B. Gludovatz, S. Scheriau, R. Pippan, Technical parameters affecting grain refinement by high pressure torsion, Int. J. Mater. Res. 100 (2009) 1653–1661. doi:10.3139/146.110224.

[30] Y.B. Wang, J.C. Ho, Y. Cao, X.Z. Liao, H.Q. Li, Y.H. Zhao, et al., Dislocation density evolution during high pressure torsion of a nanocrystalline Ni–Fe alloy, Appl. Phys. Lett. 94 (2009) 091911. doi:10.1063/1.3095852.

[31] A. Alhamidi, K. Edalati, Z. Horita, Production of nanograined intermetallics using high-pressure torsion, Mater. Res. 16 (2013) 672–678. doi:10.1590/s1516-14392013005000057.

[32] K. Edalati, E. Akiba, Z. Horita, High-pressure torsion for new hydrogen storage materials., Sci. Technol. Adv. Mater. 19 (2018) 185–193. doi:10.1080/14686996.2018.1435131.

[33] H.Y. Um, E.Y. Yoon, D.J. Lee, C.S. Lee, L.J. Park, S. Lee, et al., Hollow cone high-pressure torsion: Microstructure and tensile strength by unique severe plastic deformation, Scr. Mater. 71 (2014) 41–44. doi:10.1016/j.scriptamat.2013.09.032.

[34] G. Sakai, K. Nakamura, Z. Horita, T.G. Langdon, Application of High Pressure Torsion to Bulk Samples, Mater. Sci. Forum. 503–504 (2006) 391–398. doi:10.4028/www.scientific.net/MSF.503-504.391.

[35] K. Edalati, Z. Horita, Scaling-Up of High Pressure Torsion Using Ring Shape, Mater. Trans. 50 (2009) 92–95. doi:10.2320/matertrans.MD200822.

[36] K. Edalati, Z. Horita, Continuous high-pressure torsion, J. Mater. Sci. 45 (2010) 4578–4582. doi:10.1007/s10853-010-4381-z.

[37] R.V. Sundeev, A.M. Glezer, A.P. Menushenkov, A.V. Shalimova, O.V. Chernysheva, N.V. Umnova, Effect of high pressure torsion at different temperatures on the local atomic structure of amorphous Fe-Ni-B alloys, Mater. Des. 135 (2017) 77–83.

doi:10.1016/J.MATDES.2017.08.062.

[38] Y. Huang, R.B. Figueiredo, T. Baudin, F. Brisset, T.G. Langdon, Evolution of Strength and Homogeneity in a Magnesium AZ31 Alloy Processed by High-Pressure Torsion at Different Temperatures, Adv. Eng. Mater. 14 (2012) 1018–1026. doi:10.1002/adem.201200016.

[39] P. Verleysen, F. Van Den Abeele, J. Degrieck, Numerical simulation of HPT processing, IOP Conf. Ser. Mater. Sci. Eng. 63 (2014). doi:10.1088/1757-899X/63/1/012043.

[40] R.B. Figueiredo, P.R. Cetlin, T.G. Langdon, Using finite element modeling to examine the flow processes in quasi-constrained high-pressure torsion, Mater. Sci. Eng. A. 528 (2011) 8198–8204. doi:10.1016/J.MSEA.2011.07.040.

[41] R.B. Figueiredo, P.H.R. Pereira, M.T.P. Aguilar, P.R. Cetlin, T.G. Langdon, Using finite element modeling to examine the temperature distribution in quasi-constrained high-pressure torsion, Acta Mater. 60 (2012) 3190–3198. doi:10.1016/J.ACTAMAT.2012.02.027.

[42] M. Zehetbauer, Y.T. Zhu, Bulk nanostructured materials, Wiley-VCH, Weinheim, 2009.

[43] K. Václavová, J. Stráský, P. Harcuba, V. Polyakova, I. Semenova, M. Janeček, Investigation of Microhardness and Microstructure in Ultra-Fine Grained Metastable Beta-Ti Alloys Prepared by High Pressure Torsion, in: Proc. 13th World Conf. Titan., John Wiley & Sons, Inc., Hoboken, NJ, USA, 2016: pp. 657–662. doi:10.1002/9781119296126.ch109.

[44] J.J. Jonas, C. Ghosh, L.S. Toth, The equivalent strain in high pressure torsion, Mater. Sci. Eng. A. 607 (2014) 530–535. doi:10.1016/j.msea.2014.04.046.

[45] M. Kawasaki, B. Ahn, H. Lee, A.P. Zhilyaev, T.G. Langdon, Using high-pressure torsion to process an aluminum-magnesium nanocomposite through diffusion bonding, J. Mater. Res. 31 (2016) 88–99. doi:10.1557/jmr.2015.257.

[46] G. Faraji, H.S. Kim, H.T. Kashi, Severe Plastic Deformation : Methods, Processing and

Properties, Elsevier Science Publishing, 2018.

[47] A.P. Zhilyaev, S. Lee, G.V. Nurislamova, R.Z. Valiev, T.G. Langdon, Microhardness and microstructural evolution in pure nickel during high-pressure torsion, Scr. Mater. 44 (2001) 2753–2758. doi:10.1016/S1359-6462(01)00955-1.

[48] K. Edalati, T. Fujioka, Z. Horita, Microstructure and mechanical properties of pure Cu processed by high-pressure torsion, Mater. Sci. Eng. A. 497 (2008) 168–173. doi:10.1016/j.msea.2008.06.039.

[49] Y. Ito, K. Edalati, Z. Horita, High-pressure torsion of aluminum with ultrahigh purity (99.9999%) and occurrence of inverse Hall-Petch relationship, Mater. Sci. Eng. A. 679 (2017) 428–434. doi:10.1016/j.msea.2016.10.066.

[50] Y.D. Gamburg, G. Zangari, Introduction to Electrodeposition: Basic Terms and Fundamental Concepts, in: Theory Pract. Met. Electrodepos., Springer New York, New York, NY, 2011: pp. 1–25. doi:10.1007/978-1-4419-9669-5_1.

[51] J.Y. Kim, J. Yu, J.H. Lee, T.Y. Lee, The effects of electroplating parameters on the composition and morphology of Sn-Ag solder, J. Electron. Mater. 33 (2004) 1459–1464. doi:10.1007/s11664-004-0087-9.

[52] F. Ebrahimi, G.R. Bourne, M.S. Kelly, T.E. Matthews, Mechanical properties of nanocrystalline nickel produced by electrodeposition, Nanostructured Mater. 11 (1999) 343–350. doi:10.1016/S0965-9773(99)00050-1.

[53] K. Murase, M. Ogawa, T. Hirato, Y. Awakura, Design of Acidic Ni-Mo Alloy Plating Baths Using a Set of Apparent Equilibrium Constants, J. Electrochem. Soc. 151 (2004) C798. doi:10.1149/1.1817758.

[54] D. Sobha Jayakrishnan, Electrodeposition: the versatile technique for nanomaterials, in: Corros. Prot. Control Using Nanomater., Elsevier, 2012: pp. 86–125. doi:10.1533/9780857095800.1.86.

[55] I. Rose, C. Whittington, Ni-plating Handbook, Nickel Institute, Brussels, 2014.

doi:10.1017/CBO9781107415324.004.

[56] L.S. Sanches, S.H. Domingues, A. Carubelli, L.H. Mascaro, Electrodeposition of Ni-Mo and Fe-Mo alloys from sulfate-citrate acid solutions, J. Braz. Chem. Soc. 14 (2003) 556–563. doi:10.1590/S0103-50532003000400011.

[57] M. Paunovic, M. Schlesinger, D.D. Snyder, Fundamental Considerations, in: Mod. Electroplat., John Wiley & Sons, Inc., Hoboken, NJ, USA, 2010: pp. 1–32. doi:10.1002/9780470602638.ch1.

[58] X. Zhou, Y. Wang, Z. Liang, H. Jin, Electrochemical Deposition and Nucleation/Growth Mechanism of Ni⁻Co⁻Y_2O_3 Multiple Coatings., Mater. 11 (2018) 1124. doi:10.3390/ma11071124.

[59] P. Vanden Brande, A. Dumont, R. Winand, Nucleation and growth of nickel by electrodeposition under galvanostatic conditions, J. Appl. Electrochem. 24 (1994) 201–205. doi:10.1007/BF00242884.

[60] B.J. Hwang, R. Santhanam, Y.-L. Lin, Nucleation and Growth Mechanism of Electropolymerization of Polypyrrole on Gold/Highly Oriented Pyrolytic Graphite Electrode, J. Electrochem. Soc. 147 (2002) 2252–2257. doi:10.1149/1.1393516.

[61] A. Brenner, Electrodeposition of alloys, Academic Press, Inc., New York, 1963.

[62] H.J. Seim, M.L. Holt, The Electrodeposition of Molybdenum Alloys, J. Electrochem. Soc. 96 (1949) 205. doi:10.1149/1.2776783.

[63] D.W. Ernst, R.F. Amlie, M.L. Holt, Electrodeposition of Molydenum Alloys from Aqueous Solutions, J. Electrochem. Soc. 102 (1955) 461–469. doi:10.1149/1.2430124.

[64] N.W. Hovey, A. Krohn, G.M. Hanneken, The Electrodeposition of Nickel-Molybdenum Alloys, J. Electrochem. Soc. 110 (1963) 362. doi:10.1149/1.2425765.

[65] C.C. Nee, W. Kim, R. Weil, Pulsed Electrodeposition of Ni-Mo Alloys, J. Electrochem. Soc. 135 (1988) 1100. doi:10.1149/1.2095883.

[66] E.J. Podlaha, D. Landolt, Induced Codeposition, J. Electrochem. Soc. 143 (1996) 885–892.

doi:10.1149/1.1836553.

[67] E.J. Podlaha, D. Landolt, Induced Codeposition I. An experimental investigation of Ni-Mo alloys, J. Electrochem. Soc. 143 (1996) 885–892. doi:10.1149/1.1836553.

[68] E.J. Podlaha, D. Landolt, Induced Codeposition II. A Mathematical Model Describing the Electrodeposition of Ni-Mo Alloys, J. Electrochem. Soc. 143 (1996) 893–899. doi:10.1149/1.1836554.

[69] E. Chassaing, K. Vu Quang, R. Wiart, Mechanism of nickel-molybdenum alloy electrodeposition in citrate electrolytes, J. Appl. Electrochem. 19 (1989) 839–844. doi:10.1007/BF01007931.

[70] H. Fukushima, T. Akiyama, S. Akagi, K. Higashi, Role of Iron-Group Metals in the Induced Codeposition of Molybdenum From Aqueous Solution., Trans. Japan Inst. Met. 20 (1979) 358–364. doi:10.2320/matertrans1960.20.358.

[71] T. Akiyama, H. Fukushima, Recent Study on the Mechanism of the Electrodeposition of Iron-group Metal Alloys., ISIJ Int. 32 (1992) 787–798. doi:10.2355/isijinternational.32.787.

[72] K. Mech, P. Zabinski, M. Mucha, R. Kowalik, Electrodeposition of Catalytically Active Ni-Mo Alloys, Arch. Metall. Mater. 58 (2013) 227–229. doi:10.2478/v10172-012-0178-1.

[73] S. Sun, E.J. Podlaha, Pulse Electrodeposition of NiMoW Alloys, ECS Trans. 53 (2013) 27–35. doi:10.1149/05311.0027ecst.

[74] D. Landolt, Electrochemical and materials science aspects of alloy deposition, Electrochim. Acta. 39 (1994) 1075–1090. doi:10.1016/0013-4686(94)E0022-R.

[75] E. Bełtowska-Lehman, Kinetic correlations in codeposition of coatings of molybdenum-iron group metal alloys, J. Appl. Electrochem. 20 (1990) 132–138. doi:10.1007/BF01012482.

[76] E.J. Podlaha, M. Matlosz, D. Landolt, Electrodeposition of High Mo Content Ni-Mo Alloys under Forced Convection, J. Electrochem. Soc. 140 (1993) L149.

doi:10.1149/1.2220956.

[77] A. Bigos, E. Beltowska-Lehman, M. Kot, Studies on electrochemical deposition and physicochemical properties of nanocrystalline Ni-Mo alloys, Surf. Coatings Technol. 317 (2017) 103–109. doi:10.1016/J.SURFCOAT.2017.03.036.

[78] M.H. Allahyarzadeh, B. Roozbehani, A. Ashrafi, S.R. Shadizadeh, A. Seddighian, E. Kheradmand, A Novel Aspect of Two Imidazolium-Based Ionic Liquids in Electrodeposition of Amorphous/Nanocrystalline Ni-Mo, J. Electrochem. Soc. 159 (2012) D473–D478. doi:10.1149/2.065208jes.

[79] M.H. Allahyarzadeh, A. Ashrafi, A. Golgoon, B. Roozbehani, Effect of pulse plating parameters on the structure and properties of electrodeposited NiMo films, Mater. Chem. Phys. 175 (2016) 215–222. doi:10.1016/J.MATCHEMPHYS.2016.03.023.

[80] M.H. Allahyarzadeh, B. Roozbehani, A. Ashrafi, S.R. Shadizadeh, E. Kheradmand, Electrochemically Deposition of High Mo Content Amorphous/Nanocrystalline Ni-Mo Using Ionic Liquids as Additive, in: ECS Trans., The Electrochemical Society, 2012: pp. 11–28. doi:10.1149/1.4718388.

[81] E. Chassaing, N. Portail, A.F. Levy, G. Wang, Characterisation of electrodeposited nanocrystalline Ni-Mo alloys, J. Appl. Electrochem. 34 (2004) 1085–1091. doi:10.1007/s10800-004-2460-z.

[82] A. Bigos, E. Beltowska-Lehman, E. García-Lecina, M. Bieda, M.J. Szczerba, J. Morgiel, Ultrasound-assisted electrodeposition of Ni and Ni-Mo coatings from a citrate-ammonia electrolyte solution, J. Alloys Compd. 726 (2017) 410–416. doi:10.1016/J.JALLCOM.2017.07.300.

[83] Y.H. Zhao, Y.Z. Guo, Q. Wei, A.M. Dangelewicz, C. Xu, Y.T. Zhu, et al., Influence of specimen dimensions on the tensile behavior of ultrafine-grained Cu, Scr. Mater. 59 (2008) 627–630. doi:10.1016/j.scriptamat.2008.05.031.

[84] M.B. Myers, F. Dachille, R. Roy, Pressure Multiplication Effect in Opposed-Anvil

Configurations, Rev. Sci. Instrum. 34 (1963) 401–402. doi:10.1063/1.1718377.

[85] G. Sakai, K. Nakamura, Z. Horita, T.G. Langdon, Developing high-pressure torsion for use with bulk samples, Mater. Sci. Eng. A. 406 (2005) 268–273. doi:10.1016/j.msea.2005.06.049.

[86] Y. Harai, K. Edalati, Z. Horita, T.G. Langdon, Using ring samples to evaluate the processing characteristics in high-pressure torsion, Acta Mater. 57 (2009) 1147–1153. doi:10.1016/j.actamat.2008.10.046.

[87] H.J. Frost, M.F. Ashby, Deformation-mechanism maps : the plasticity and creep of metals and ceramics, Pergamon Press, Oxford [u.a.], 1982. https://www.tib.eu/en/search/id/TIBKAT%3A01753397X/Deformation-mechanism-maps-the-plasticity-and-creep/ (accessed June 28, 2019).

[88] K. Edalati, R. Miresmaeili, Z. Horita, H. Kanayama, R. Pippan, Significance of temperature increase in processing by high-pressure torsion, Mater. Sci. Eng. A. 528 (2011) 7301–7305. doi:10.1016/j.msea.2011.06.031.

[89] J. Gubicza, M. El-Tahawy, Y. Huang, H. Choi, H. Choe, J.L. Lábár, et al., Microstructure, phase composition and hardness evolution in 316L stainless steel processed by high-pressure torsion, Mater. Sci. Eng. A. 657 (2016) 215–223. doi:10.1016/j.msea.2016.01.057.

[90] M.Y. Maeda, J.J.H. Quintero, M.T. Izumi, M.F. Hupalo, O.M. Cintho, Study of Cryogenic Rolling of FCC Metals with Different Stacking Fault Energies, Mater. Res. 20 (2017) 716–721. doi:10.1590/1980-5373-mr-2017-0054.

[91] W. Wu, L. Guo, B. Guo, Y. Liu, M. Song, Altered microstructural evolution and mechanical properties of CoCrFeNiMo0.15 high-entropy alloy by cryogenic rolling, Mater. Sci. Eng. A. 759 (2019) 574–582. doi:10.1016/j.msea.2019.05.078.

[92] J. Gubicza, Correlation between processing conditions, lattice defect structure and mechanical performance of ultrafine-grained materials, Acta Phys. Pol. A. 128 (2015) 479–485. doi:10.12693/APhysPolA.128.479.

[93] J. Gubicza, N.Q. Chinh, Z. Horita, T.G. Langdon, Effect of Mg addition on microstructure and mechanical properties of aluminum, Mater. Sci. Eng. A. (2004) 55–59. doi:10.1016/j.msea.2004.03.076.

[94] V. V. Popov, A. V. Stolbovsky, E.N. Popova, Structure of nickel–copper alloys subjected to high-pressure torsion to saturation stage, Phys. Met. Metallogr. 118 (2017) 1073–1080. doi:10.1134/s0031918x17110114.

[95] J. Gubicza, S. V. Dobatkin, E. Khosravi, A.A. Kuznetsov, J.L. Lábár, Microstructural stability of Cu processed by different routes of severe plastic deformation, Mater. Sci. Eng. A. 528 (2011) 1828–1832. doi:10.1016/j.msea.2010.11.026.

[96] A. Alhamidi, K. Edalati, Z. Horita, S. Hirosawa, K. Matsuda, D. Terada, Softening by severe plastic deformation and hardening by annealing of aluminum-zinc alloy: Significance of elemental and spinodal decompositions, Mater. Sci. Eng. A. 610 (2014) 17–27. doi:10.1016/j.msea.2014.05.026.

[97] O. Andreau, J. Gubicza, N. Xian Zhang, Y. Huang, P. Jenei, T.G. Langdon, Effect of short-term annealing on the microstructures and flow properties of an Al-1% Mg alloy processed by high-pressure torsion, Mater. Sci. Eng. A. 615 (2014) 231–239. doi:10.1016/j.msea.2014.07.018.

[98] A. Bachmaier, A. Hohenwarter, R. Pippan, New procedure to generate stable nanocrystallites by severe plastic deformation, Scr. Mater. 61 (2009) 1016–1019. doi:10.1016/j.scriptamat.2009.08.016.

[99] D. Setman, M.B. Kerber, E. Schafler, M.J. Zehetbauer, Activation enthalpies of deformation-induced lattice defects in severe plastic deformation nanometals measured by differential scanning calorimetry, in: Metall. Mater. Trans. A Phys. Metall. Mater. Sci., 2010: pp. 810–815. doi:10.1007/s11661-009-0058-0.

[100] N. Lugo, N. Llorca, J.J. Suñol, J.M. Cabrera, Thermal stability of ultrafine grains size of pure copper obtained by equal-channel angular pressing, J. Mater. Sci. 45 (2010) 2264–

2273. doi:10.1007/s10853-009-4139-7.

[101] W.Q. Cao, C.F. Gu, E. V. Pereloma, C.H.J. Davies, Stored energy, vacancies and thermal stability of ultra-fine grained copper, Mater. Sci. Eng. A. 492 (2008) 74–79. doi:10.1016/j.msea.2008.02.048.

[102] J. Čížek, I. Procházka, M. Cieslar, R. Kužel, J. Kuriplach, F. Chmelík, et al., Thermal stability of ultrafine grained copper, Phys. Rev. B - Condens. Matter Mater. Phys. 65 (2002) 1–16. doi:10.1103/PhysRevB.65.094106.

[103] Y.K. Huang, A.A. Menovsky, F.R. de Boer, Calorimetric analysis of the grain growth in nanocrystalline copper samples, Nanostructured Mater. 2 (1993) 587–595. doi:10.1016/0965-9773(93)90032-7.

[104] Z. Hegedűs, J. Gubicza, M. Kawasaki, N.Q. Chinh, K. Süvegh, Z. Fogarassy, et al., High temperature thermal stability of ultrafine-grained silver processed by equal-channel angular pressing, J. Mater. Sci. 48 (2013) 1675–1684. doi:10.1007/s10853-012-6926-9.

[105] J. Lian, R.Z. Valiev, B. Baudelet, On the enhanced grain growth in ultrafine grained metals, Acta Metall. Mater. 43 (1995) 4165–4170. doi:10.1016/0956-7151(95)00087-C.

[106] S.C. Tjong, H. Chen, Nanocrystalline materials and coatings, Mater. Sci. Eng. R Reports. 45 (2004) 1–88. doi:10.1016/j.mser.2004.07.001.

[107] C.M. Kuo, C.S. Lin, Static recovery activation energy of pure copper at room temperature, Scr. Mater. 57 (2007) 667–670. doi:10.1016/j.scriptamat.2007.06.054.

[108] S. Divinski, J. Ribbe, G. Schmitz, C. Herzig, Grain boundary diffusion and segregation of Ni in Cu, Acta Mater. 55 (2007) 3337–3346. doi:10.1016/j.actamat.2007.01.032.

[109] D. Setman, E. Schafler, E. Korznikova, M.J. Zehetbauer, The presence and nature of vacancy type defects in nanometals detained by severe plastic deformation, Mater. Sci. Eng. A. 493 (2008) 116–122. doi:10.1016/j.msea.2007.06.093.

[110] F. Zhou, X.Z. Liao, Y.T. Zhu, S. Dallek, E.J. Lavernia, Microstructural evolution during recovery and recrystallization of a nanocrystalline Al-Mg alloy prepared by cryogenic ball

milling, Acta Mater. 51 (2003) 2777–2791. doi:10.1016/S1359-6454(03)00083-1.

[111] B. Adamczyk-Cieślak, J. Mizera, K.J. Kurzydłowski, Thermal stability of model Al–Li alloys after severe plastic deformation—Effect of the solute Li atoms, Mater. Sci. Eng. A. 527 (2010) 4716–4722. doi:10.1016/J.MSEA.2010.04.032.

[112] A.P. Zhilyaev, B.-K. Kim, J.A. Szpunar, M.D. Baró, T.G. Langdon, The microstructural characteristics of ultrafine-grained nickel, Mater. Sci. Eng. A. 391 (2005) 377–389. doi:10.1016/j.msea.2004.09.030.

[113] A.P. Zhilyaev, J. Gubicza, G. Nurislamova, Á. Révész, S. Suriñach, M.D. Baró, et al., Microstructural characterization of ultrafine-grained nickel, Phys. Status Solidi Appl. Res. 198 (2003) 263–271. doi:10.1002/pssa.200306608.

[114] S. Sabbaghianrad, T.G. Langdon, A critical evaluation of the processing of an aluminum 7075 alloy using a combination of ECAP and HPT, Mater. Sci. Eng. A. 596 (2014) 52–58. doi:10.1016/j.msea.2013.12.034.

[115] T.R. Lee, C.P. Chang, P.W. Kao, The tensile behavior and deformation microstructure of cryo-rolled and annealed pure nickel, Mater. Sci. Eng. A. 408 (2005) 131–135. doi:10.1016/j.msea.2005.07.045.

[116] I. Bakonyi, E. Tóth-Kádár, T. Tarnóczi, L.K. Varga, Á. Cziráki, I. Geröcs, et al., Structure and properties of fine-grained electrodeposited nickel, Nanostructured Mater. 3 (1993) 155–161. doi:10.1016/0965-9773(93)90073-K.

[117] I. Bakonyi, E. Tóth-Kádár, L. Pogány, Á. Cziráki, I. Gerőcs, K. Varga-Josepovits, et al., Preparation and characterization of d.c.-plated nanocrystalline nickel electrodeposits, Surf. Coatings Technol. 78 (1996) 124–136. doi:10.1016/0257-8972(94)02399-9.

[118] J.X. Kang, W.Z. Zhao, G.F. Zhang, Influence of electrodeposition parameters on the deposition rate and microhardness of nanocrystalline Ni coatings, Surf. Coatings Technol. 203 (2009) 1815–1818. doi:10.1016/j.surfcoat.2009.01.003.

[119] W. René, Electrodeposition of metals and alloys—new results and perspectives,

Electrochim. Acta. 39 (1994) 1091–1105. doi:10.1016/0013-4686(94)e0023-s.

[120] A.M. Rashidi, A. Amadeh, The effect of current density on the grain size of electrodeposited nanocrystalline nickel coatings, Surf. Coatings Technol. 202 (2008) 3772–3776. doi:10.1016/j.surfcoat.2008.01.018.

[121] F. Ebrahimi, Z. Ahmed, The effect of current density on properties of electrodeposited nanocrystalline nickel, J. Appl. Electrochem. 33 (2003) 733–739. doi:10.1023/A:1025049802635.

[122] A. Sharma, Y.J. Jang, J.P. Jung, Effect of current density on morphology of electroplated tin, Surf. Eng. 31 (2015) 458–464. doi:10.1179/1743294414y.0000000427.

[123] W. Lu, C. Ou, P. Huang, P. Yan, B. Yan, Effect of pH on the structural properties of electrodeposited nanocrystalline FeCo films, Int. J. Electrochem. Sci. 8 (2013) 8218–8226.

[124] K.S. Kumar, H. Van Swygenhoven, S. Suresh, Mechanical behavior of nanocrystalline metals and alloys, Acta Mater. 51 (2003) 5743–5774. doi:10.1016/j.actamat.2003.08.032.

[125] M. Hagarová, D. Jakubéczyová, J. Cervová, Microstructure and properties of electroplated Ni-Co alloy coatings, Int. J. Electrochem. Sci. 10 (2015) 9968–9974.

[126] M. Zamani, A. Amadeh, S.M. Lari Baghal, Effect of Co content on electrodeposition mechanism and mechanical properties of electrodeposited Ni-Co alloy, Trans. Nonferrous Met. Soc. China (English Ed. 26 (2016) 484–491. doi:10.1016/S1003-6326(16)64136-5.

[127] A.M. Rashidi, A. Amadeh, The effect of saccharin addition and bath temperature on the grain size of nanocrystalline nickel coatings, Surf. Coatings Technol. 204 (2009) 353–358. doi:10.1016/j.surfcoat.2009.07.036.

[128] N. Zaghian, B.S. Boroujeny, The Effect of Saccharin on Microstructure and Corrosion Behavior of Nanocrystalline Nickel Thin Films in Alkaline Solution, J. Adv. Mater. Process. 5 (2017) 25–37.

[129] M. Saitou, Internal stress in nickel thin films affected by additives in electrodeposition, Int. J. Electrochem. Sci. 11 (2016) 1651–1660.

[130] Y. Li, J. Yao, X. Huang, Effect of Saccharin on the Process and Properties of Nickel Electrodeposition from Sulfate Electrolyte, Int. J. Metall. Mater. Eng. 2 (2016). doi:10.15344/2455-2372/2016/123.

[131] S. Tebbakh, Y. Messaoudi, A. Azizi, N. Fenineche, G. Schmerber, A. Dinia, The influence of saccharin on the electrodeposition and properties of Co–Ni alloy thin films, Trans. IMF. 93 (2015) 196–204. doi:10.1179/0020296715z.000000000247.

[132] T. Kolonits, P. Jenei, B.G. Tóth, Z. Czigány, J. Gubicza, L. Péter, et al., Characterization of Defect Structure in Electrodeposited Nanocrystalline Ni Films, J. Electrochem. Soc. 163 (2016) D107–D114. doi:10.1149/2.0911603jes.

[133] A.M. Rashidi, A. Amadeh, Effect of electroplating parameters on microstructure of nanocrystalline nickel coatings, J. Mater. Sci. Technol. 26 (2010) 82–86. doi:10.1016/S1005-0302(10)60013-8.

[134] F. Czerwinski, J.A. Szpunar, Controlling the thermal stability of texture in single-phase electrodeposits, Nanostructured Mater. 11 (1999) 669–676. doi:10.1016/S0965-9773(99)00355-4.

[135] Z.F. Zhou, Y. Pan, Y.C. Zhou, L. Yang, Growth dynamics and thermal stability of Ni nanocrystalline nanowires, Appl. Surf. Sci. 257 (2011) 9991–9995. doi:10.1016/j.apsusc.2011.06.125.

[136] X.C. Liu, H.W. Zhang, K. Lu, Strain-induced ultrahard and ultrastable nanolaminated structure in nickel, Science. 342 (2013) 337–340. doi:10.1126/science.1242578.

[137] G.D. Hibbard, U. Erb, K.T. Aust, U. Klement, G. Palumbo, Thermal Stability of Nanostructured Electrodeposits, J. Metastable Nanocrystalline Mater. 13 (2002) 387–396. doi:10.4028/www.scientific.net/JMNM.13.387.

[138] E.A. Holm, S.M. Foiles, How grain growth stops: A mechanism for grain-growth stagnation in pure materials, Science. 328 (2010) 1138–1141. doi:10.1126/science.1187833.

[139] R. Klemm, E. Thiele, C. Holste, J. Eckert, N. Schell, Thermal stability of grain structure and defects in submicrocrystalline and nanocrystalline nickel, Scr. Mater. 46 (2002) 685–690. doi:10.1016/S1359-6462(02)00054-4.

[140] A.A. Talin, E.A. Marquis, S.H. Goods, J.J. Kelly, M.K. Miller, Thermal stability of Ni-Mn electrodeposits, Acta Mater. 54 (2006) 1935–1947. doi:10.1016/j.actamat.2005.12.027.

[141] A. Bachmaier, C. Motz, On the remarkable thermal stability of nanocrystalline cobalt via alloying, Mater. Sci. Eng. A. 624 (2015) 41–51. doi:10.1016/j.msea.2014.11.062.

[142] K. Liu, Z. Huang, X. Zhang, D. Lu, A. Atrens, H. Zhou, et al., Influence of Ag micro-alloying on the thermal stability and ageing characteristics of a Cu–14Fe in-situ composite, Mater. Sci. Eng. A. 673 (2016) 1–7. doi:10.1016/j.msea.2016.07.017.

[143] T. Liang, Z. Chen, X. Yang, J. Zhang, P. Zhang, The thermodynamic stability induced by solute co-segregation in nanocrystalline ternary alloys, Int. J. Mater. Res. 108 (2017) 435–440. doi:10.3139/146.111496.

[144] G.D. Hibbard, J.L. McCrea, G. Palumbo, K.T. Aust, U. Erb, An initial analysis of mechanisms leading to late stage abnormal grain growth in nanocrystalline Ni, Scr. Mater. 47 (2002) 83–87. doi:10.1016/S1359-6462(02)00098-2.

[145] X.F. Zhang, T. Fujita, D. Pan, J.S. Yu, T. Sakurai, M.W. Chen, Influences of grain size and grain boundary segregation on mechanical behavior of nanocrystalline Ni, Mater. Sci. Eng. A. 527 (2010) 2297–2304. doi:10.1016/j.msea.2009.12.005.

[146] M.J.N.V. Prasad, A.H. Chokshi, On the exothermic peak during annealing of electrodeposited nanocrystalline nickel, Scr. Mater. 64 (2011) 544–547. doi:10.1016/j.scriptamat.2010.11.038.

[147] J.E. Darnbrough, P.E.J. Flewitt, Growth of abnormal planar faceted grains in nanocrystalline nickel containing impurity sulphur, Acta Mater. 79 (2014) 421–433. doi:10.1016/j.actamat.2014.05.059.

[148] J.C. Hsu, K.L. Lin, The effect of saccharin addition on the mechanical properties and

fracture behavior of electroless Ni-Cu-P deposit on Al, Thin Solid Films. 471 (2005) 186–193. doi:10.1016/j.tsf.2004.08.025.

[149] E. Schafler, G. Steiner, E. Korznikova, M. Kerber, M.J. Zehetbauer, Lattice defect investigation of ECAP-Cu by means of X-ray line profile analysis, calorimetry and electrical resistometry, Mater. Sci. Eng. A. 410–411 (2005) 169–173. doi:10.1016/j.msea.2005.08.070.

[150] E. Rahimi, A. Davoodi, A. R. Kiani Rashid, Characterization of screw dislocation-driven growth in nickel micro-nanostructure electrodeposition process by AFM, Mater. Lett. 210 (2018) 341–344. doi:10.1016/j.matlet.2017.09.057.

[151] Y.D. Gamburg, G. Zangari, Theory and Practice of Metal Electrodeposition, Springer, New York, 2011. doi:10.1007/978-1-4419-9669-5.

[152] G. Wang, Z. Jiang, J. Lian, Q. Jiang, The grain refinement mechanism of electrodeposited copper, J. Mater. Res. 24 (2009) 3226–3236. doi:10.1557/jmr.2009.0372.

[153] J. Hu, Y.-N. Shi, K. Lu, Thermal analysis of electrodeposited nano-grained Ni-Mo alloys, Scr. Mater. 154 (2018) 182–185. doi:10.1016/j.scriptamat.2018.05.036.

[154] A.M. El-Sherik, U. Erb, G. Palumbo, K.T. Aust, Deviations from hall-petch behaviour in as-prepared nanocrystalline nickel, Scr. Metall. Mater. 27 (1992) 1185–1188. doi:10.1016/0956-716X(92)90596-7.

[155] I. Matsui, T. Uesugi, Y. Takigawa, K. Higashi, Effect of interstitial carbon on the mechanical properties of electrodeposited bulk nanocrystalline Ni, Acta Mater. 61 (2013) 3360–3369. doi:10.1016/j.actamat.2013.02.025.

[156] F. Dalla Torre, H. Van Swygenhoven, M. Victoria, Nanocrystalline electrodeposited Ni: Microstructure and tensile properties, Acta Mater. 50 (2002) 3957–3970. doi:10.1016/S1359-6454(02)00198-2.

[157] K.S. Kumar, S. Suresh, M.F. Chisholm, J.A. Horton, P. Wang, Deformation of electrodeposited nanocrystalline nickel, Acta Mater. 51 (2003) 387–405.

doi:10.1016/S1359-6454(02)00421-4.

[158] X. Shen, J. Lian, Z. Jiang, Q. Jiang, High strength and high ductility of electrodeposited nanocrystalline Ni with a broad grain size distribution, Mater. Sci. Eng. A. 487 (2008) 410–416. doi:10.1016/j.msea.2007.10.018.

[159] G. Changdong, L. Jianshe, J. Zhonghao, J. Qing, Enhanced tensile ductility in an electrodeposited nanocrystalline Ni, in: NanoSingapore 2006 IEEE Conf. Emerg. Technol. - Nanoelectron. - Proc., 2006: pp. 293–297. doi:10.1109/NANOEL.2006.1609732.

[160] K.L. Morgan, Z. Ahmed, F. Ebrahimi, The Effect of Deposition Parameters on Tensile Properties of Pulse-Plated Nanocrystalline Nickel, MRS Proc. 634 (2000). doi:10.1557/proc-634-b3.11.1.

[161] C.E. Carlton, P.J. Ferreira, What is behind the inverse Hall-Petch effect in nanocrystalline materials?, Acta Mater. 55 (2007) 3749–3756. doi:10.1016/j.actamat.2007.02.021.

[162] Y.M. Wang, E. Ma, Three strategies to achieve uniform tensile deformation in a nanostructured metal, Acta Mater. 52 (2004) 1699–1709. doi:10.1016/j.actamat.2003.12.022.

[163] Y. Wang, M. Chen, F. Zhou, E. Ma, High tensile ductility in a nanostructured metal, Nature. 419 (2002) 912–915. doi:10.1038/nature01133.

[164] Y. Zhao, T. Topping, J.F. Bingert, J.J. Thornton, A.M. Dangelewicz, Y. Li, et al., High tensile ductility and strength in bulk nanostructured nickel, Adv. Mater. 20 (2008) 3028–3033. doi:10.1002/adma.200800214.

[165] K. Sitarama Raju, V. Subramanya Sarma, A. Kauffmann, Z. Hegedus, J. Gubicza, M. Peterlechner, et al., High strength and ductile ultrafine-grained Cu-Ag alloy through bimodal grain size, dislocation density and solute distribution, Acta Mater. 61 (2013) 228–238. doi:10.1016/j.actamat.2012.09.053.

[166] A. Hasnaoui, H. Van Swygenhoven, P.M. Derlet, On non-equilibrium grain boundaries and their effect on thermal and mechanical behaviour: a molecular dynamics computer

simulation, Acta Mater. 50 (2002) 3927–3939. doi:10.1016/S1359-6454(02)00195-7.

[167] Y.M. Wang, S. Cheng, Q.M. Wei, E. Ma, T.G. Nieh, A. Hamza, Effects of annealing and impurities on tensile properties of electrodeposited nanocrystalline Ni, Scr. Mater. 51 (2004) 1023–1028. doi:10.1016/j.scriptamat.2004.08.015.

[168] X. Huang, N. Hansen, N. Tsuji, Hardening by Annealing and Softening by Deformation in Nanostructured Metals, Science. 312 (2006) 249–251. doi:10.1126/science.1124268.

[169] L. Chang, P.W. Kao, C.-H. Chen, Strengthening mechanisms in electrodeposited Ni–P alloys with nanocrystalline grains, Scr. Mater. 56 (2007) 713–716. doi:10.1016/J.SCRIPTAMAT.2006.12.036.

[170] J. Tao, G. Chen, W. Jian, J. Wang, Y. Zhu, X. Zhu, et al., Anneal hardening of a nanostructured Cu–Al alloy processed by high-pressure torsion and rolling, Mater. Sci. Eng. A. 628 (2015) 207–215. doi:10.1016/J.MSEA.2015.01.055.

[171] J. Hu, Y.N. Shi, X. Sauvage, G. Sha, K. Lu, Grain boundary stability governs hardening and softening in extremely fine nanograined metals., Science. 355 (2017) 1292–1296. doi:10.1126/science.aal5166.

[172] G. Kapoor, Y. Huang, V.S. Sarma, T.G. Langdon, J. Gubicza, Effect of Mo addition on the microstructure and hardness of ultrafine-grained Ni alloys processed by a combination of cryorolling and high-pressure torsion, Mater. Sci. Eng. A. 688 (2017) 92–100. doi:10.1016/j.msea.2017.01.104.

[173] J. Gubicza, X-Ray Line Profile Analysis in Materials Science, IGI Global, 2014. doi:10.4018/978-1-4666-5852-3.

[174] E.F. Bertaut, Debye-Scherrer Lines and Distribution of the Dimensions of the Bragg Domains in Polycrystalline Powders, Acta Crystallogr. 3 (1950) 14–18. doi:10.1107/S0365110X50000045.

[175] A. Guinier, X-ray diffraction in crystals, imperfect crystals, and amorphous bodies., W.H. Freeman, San Francisco, 1963.

[176] B.E. Warren, B.L. Averbach, The Separation of Cold-Work Distortion and Particle Size Broadening in X-Ray Patterns, J. Appl. Phys. 23 (1952) 497–497. doi:10.1063/1.1702234.

[177] T. Ungár, G. Tichy, The Effect of Dislocation Contrast on X-Ray Line Profiles in Untextured Polycrystals, Phys. Status Solidi. 171 (1999) 425–434. doi:10.1002/(SICI)1521-396X(199902)171:2<425::AID-PSSA425>3.0.CO;2-W.

[178] A. Borbély, J. Dragomir-Cernatescu, G. Ribárik, T. Ungár, Computer program *ANIZC* for the calculation of diffraction contrast factors of dislocations in elastically anisotropic cubic, hexagonal and trigonal crystals, J. Appl. Crystallogr. 36 (2003) 160–162. doi:10.1107/S0021889802021581.

[179] G. Ribárik, T. Ungár, J. Gubicza, *MWP-fit* : a program for multiple whole-profile fitting of diffraction peak profiles by *ab initio* theoretical functions, J. Appl. Crystallogr. 34 (2001) 669–676. doi:10.1107/S0021889801011451.

[180] Y. Mishima, S. Ochiai, T. Suzuki, Lattice parameters of Ni(γ), Ni3Al(γ') and Ni3Ga(γ') solid solutions with additions of transition and B-subgroup elements, Acta Metall. 33 (1985) 1161–1169. doi:10.1016/0001-6160(85)90211-1.

[181] M. Karolus, E. Łagiwka, The Structural Studies on Nanocrystalline Ni-Mo Alloys after Annealing, in: Appl. Crystallogr., World Scientific, 2004: pp. 337–341. doi:10.1142/9789812702913_0066.

[182] S.H. Zhou, Y. Wang, L.-Q. Chen, Z.-K. Liu, R.E. Napolitano, Solution-based thermodynamic modeling of the Ni–Al–Mo system using first-principles calculations, Calphad. 46 (2014) 124–133. doi:10.1016/J.CALPHAD.2014.03.002.

[183] R. Kirchheim, Grain coarsening inhibited by solute segregation, Acta Mater. 50 (2002) 413–419. doi:10.1016/S1359-6454(01)00338-X.

[184] F. Liu, R. Kirchheim, Nano-scale grain growth inhibited by reducing grain boundary energy through solute segregation, J. Cryst. Growth. 264 (2004) 385–391. doi:10.1016/J.JCRYSGRO.2003.12.021.

[185] H.A. Murdoch, C.A. Schuh, Stability of binary nanocrystalline alloys against grain growth and phase separation, Acta Mater. 61 (2013) 2121–2132. doi:10.1016/J.ACTAMAT.2012.12.033.

[186] P. Jenei, J. Gubicza, E.Y. Yoon, H.S. Kim, J.L. Lábár, High temperature thermal stability of pure copper and copper–carbon nanotube composites consolidated by High Pressure Torsion, Compos. Part A Appl. Sci. Manuf. 51 (2013) 71–79. doi:10.1016/J.COMPOSITESA.2013.04.007.

[187] G. Ribárik, J. Gubicza, T. Ungár, Correlation between strength and microstructure of ball-milled Al–Mg alloys determined by X-ray diffraction, Mater. Sci. Eng. A. 387–389 (2004) 343–347. doi:10.1016/j.msea.2004.01.089.

[188] J. Gubicza, N.Q. Chinh, J.L. Lábár, S. Dobatkin, Z. Hegedűs, T.G. Langdon, Correlation between microstructure and mechanical properties of severely deformed metals, J. Alloys Compd. 483 (2009) 271–274. doi:10.1016/J.JALLCOM.2008.07.200.

[189] F.H. Olivares, J. Gil Sevillano, A quantitative assessment of forest-hardening in f.c.c. metals, Acta Metall. 35 (1987) 631–641. doi:10.1016/0001-6160(87)90186-6.

[190] G. Kapoor, L. Péter, É. Fekete, J.L. Lábár, J. Gubicza, The influence of Mo addition on the microstructure and its thermal stability for electrodeposited Ni films, Mater. Charact. 145 (2018) 563–572. doi:10.1016/j.matchar.2018.09.026.

[191] W. Li, S. Lu, Q.M. Hu, S.K. Kwon, B. Johansson, L. Vitos, Generalized stacking fault energies of alloys, J. Phys. Condens. Matter. 26 (2014) 265005. doi:10.1088/0953-8984/26/26/265005.

[192] F.J. Humphreys, M. Hatherly, Recrystallization and related annealing phenomena, 2nd ed., Pergamon Press, Oxford, 2004.

[193] D.L. Olmsted, S.M. Foiles, E.A. Holm, Survey of computed grain boundary properties in face-centered cubic metals: I. Grain boundary energy, Acta Mater. 57 (2009) 3694–3703. doi:10.1016/j.actamat.2009.04.007.

[194] G.S. Rohrer, E.A. Holm, A.D. Rollett, S.M. Foiles, J. Li, D.L. Olmsted, Comparing calculated and measured grain boundary energies in nickel, Acta Mater. 58 (2010) 5063–5069. doi:10.1016/j.actamat.2010.05.042.

[195] V. V. Bulatov, B.W. Reed, M. Kumar, Grain boundary energy function for fcc metals, Acta Mater. 65 (2014) 161–175. doi:10.1016/j.actamat.2013.10.057.

[196] X. Li, Y. Wei, W. Yang, H. Gao, Competing grain-boundary- and dislocation-mediated mechanisms in plastic strain recovery in nanocrystalline aluminum, Proc. Natl. Acad. Sci. 106 (2009) 16108–16113. doi:10.1073/PNAS.0901765106.

[197] H. Alimadadi, A.B. Fanta, M.A.J. Somers, K. Pantleon, Crystallographic orientations and twinning of electrodeposited nickel—a study with complementary characterization methods, Surf. Coatings Technol. 254 (2014) 207–216. doi:10.1016/j.surfcoat.2014.06.013.

[198] H. Alimadadi, A.B. Fanta, T. Kasama, M.A.J. Somers, K. Pantleon, Texture and microstructure evolution in nickel electrodeposited from an additive-free Watts electrolyte, Surf. Coatings Technol. 299 (2016) 1–6. doi:10.1016/J.SURFCOAT.2016.04.068.

[199] G. Kapoor, Y. Huang, V. Subramanya Sarma, T.G. Langdon, J. Gubicza, Evolution of the microstructure during annealing of ultrafine-grained Ni with different Mo contents, Mater. Charact. 130 (2017) 56–63. doi:10.1016/j.matchar.2017.05.034.

[200] S. Ruan, C.A. Schuh, Mesoscale structure and segregation in electrodeposited nanocrystalline alloys, Scr. Mater. 59 (2008) 1218–1221. doi:10.1016/j.scriptamat.2008.08.010.

[201] A.J. Detor, C.A. Schuh, Grain boundary segregation, chemical ordering and stability of nanocrystalline alloys: Atomistic computer simulations in the Ni–W system, Acta Mater. 55 (2007) 4221–4232. doi:10.1016/J.ACTAMAT.2007.03.024.

[202] M.H. Allahyarzadeh, M. Aliofkhazraei, A.R. Rezvanian, V. Torabinejad, A.R. Sabour Rouhaghdam, Ni-W electrodeposited coatings: Characterization, properties and applications, Surf. Coatings Technol. 307 (2016) 978–1010.

doi:10.1016/J.SURFCOAT.2016.09.052.

[203] J. Čížek, M. Janeček, O. Srba, R. Kužel, Z. Barnovská, I. Procházka, et al., Evolution of defects in copper deformed by high-pressure torsion, Acta Mater. 59 (2011) 2322–2329. doi:10.1016/j.actamat.2010.12.028.

Declarations for Dissertation

I. The data of the doctoral dissertation:

Name of the author: Garima Kapoor
MTMT-identifier: 10063724
Title and subtitle of the doctoral dissertation: Microstructure and Mechanical Behavior of Ultrafine-grained Ni-Mo Alloys Processed by Top-Down and Bottom-Up Methods
DOI-identifier: 10.15476/ELTE.2019.211
Name of the doctoral school: Doctoral School of Physics
Name of the doctoral programme: Materials Science and Solid-State Physics Program
Name and scientific degree of the supervisor: Prof. Jenő Gubicza, DSc
Workplace of the supervisor: Eötvös Loránd University, Department of Materials Physics

II. Declarations

1. As the author of the doctoral dissertation,
a) I agree to public disclosure of my doctoral dissertation after obtaining a doctoral degree in the storage of ELTE Digital Institutional Repository. I authorize the administrator of the Department of Doctoral, Habilitational and International Affairs of the Dean's Office of the faculty of Science to upload the dissertation and the abstract to ELTE Digital Institutional Repository, and I authorize the administrator to fill all the declarations that are required in this procedure.
b) I request to defer public disclosure to the University Library and the ELTE Digital Institutional Repository until the date of announcement of the patent or protection. For details, see the attached application form;
c) I request in case the doctoral dissertation contains qualified data pertaining to national security, to disclose the doctoral dissertation publicly to the University Library and the ELTE Digital Institutional Repository ensuing the lapse of the period of the qualification process.;
d) I request to defer public disclosure to the University Library and the ELTE Digital Institutional Repository, in case there is a publishing contract concluded during the doctoral procedure or up until the award of the degree. However, the bibliographical data of the work shall be accessible to the public. If the publication of the doctoral dissertation will not be carried out within a year from the award of the degree subject to the publishing contract, I agree to the public disclosure of the doctoral dissertation and abstract to the University Library and the ELTE Digital Institutional Repository.
2. As the author of the doctoral dissertation, I declare that
a) the doctoral dissertation and abstract uploaded to the ELTE Digital Institutional Repository are entirely the result of my own intellectual work and as far as I know, I did not infringe anyone's intellectual property rights.;
b) the printed version of the doctoral dissertation and the abstract are identical with the doctoral dissertation files (texts and diagrams) submitted on electronic device.
3. As the author of the doctoral dissertation, I agree to the inspection of the dissertation and the abstract by uploading them to a plagiarism checker software.

Budapest, 27th Aug 2019

……

Signature of dissertation author